

**The Wetting of Two Dimensional Nanomaterials and their Industrial Applications**

by

Eklavya Singh

A Thesis Submitted to the Graduate  
Faculty of Rensselaer Polytechnic Institute  
in Partial Fulfillment of the  
Requirements for the degree of  
DOCTOR OF PHILOSOPHY  
Major Subject: Mechanical Engineering

Approved by the  
Examining Committee:

---

Dr. Nikhil Koratkar, Thesis Adviser

---

Dr. Johnson Samuel, Member

---

Dr. Yunfeng Shi, Member

---

Dr. Jie Lian, Member

Rensselaer Polytechnic Institute  
Troy, New York

December, 2014  
(For Graduation December 2014)

© Copyright 2014  
by  
Eklavya Singh  
All Rights Reserved

# CONTENTS

LIST OF FIGURES .....	v
ACKNOWLEDGMENT .....	xii
ABSTRACT .....	xiii
1. Introduction.....	1
1.1 Objectives of this Study .....	1
1.2 References .....	4
2. The Wetting of Supported Graphene.....	6
2.1 Graphene on Flat Surfaces .....	6
2.2 Non-Conformal Coating of Graphene on Rough Surfaces .....	9
2.2.1 Introduction .....	9
2.2.2 Graphene Draped Nanostructures .....	10
2.2.3 Water Contact Angle Measurements .....	12
2.2.4 Droplet Impact Experiments .....	16
2.2.5 Molecular Dynamics Simulations .....	20
2.2.6 Materials and Methods.....	22
2.3 Conformal Coating of Graphene on Rough Surfaces .....	25
2.3.1 Introduction .....	25
2.3.2 Conformal Graphene Coatings via “In-Situ” Deposition.....	26
2.3.3 Experimental Results and Discussion .....	28
2.4 Summary .....	36
2.5 References .....	37
3. Freestanding Superhydrophobic Graphene Foams .....	39
3.1 Introduction .....	39
3.2 Graphene Foam Macrostructure.....	40
3.3 Theoretical Contact Angle Prediction .....	41
3.4 Water Contact Angle Measurements .....	43

3.5	Droplet Impact Experiments .....	45
3.6	Materials and Methods .....	50
3.7	Summary .....	51
3.8	References .....	52
4.	Transition Metal Dichalcogenides .....	54
4.1	Introduction .....	54
4.2	Synthesis and Characterization .....	56
4.3	Water Contact Angle Measurements .....	58
4.4	Aging of Samples .....	60
4.5	Chalcogen Substitution for Hydrophobic/Hydrophilic Patterning.....	62
4.6	Summary .....	65
4.7	References .....	66
5.	Application Development using Wetting Science .....	67
5.1	Graphene Additives for Metal Cutting Fluids.....	67
5.1.1	Introduction .....	67
5.1.2	Dispersing Graphene in Aqueous and Non-Aqueous Mediums .....	68
5.1.3	Summary .....	81
5.1.4	References .....	83
5.2	Nanomaterial Electrode Synthesis for Energy Storage Devices .....	84
5.2.1	Introduction .....	84
5.2.2	Lithium Ion Batteries .....	85
5.2.3	Freestanding Graphene Electrodes.....	87
5.2.4	Roll-to-Roll Production and Assembly of 2D Nanomaterials .....	90
5.2.5	Summary .....	95
5.2.6	References .....	97
6.	Conclusion .....	99

## LIST OF FIGURES

- Figure 1 – Wetting transparency of graphene. (a) Water contact angle measurements for Si and Au substrates with and without monolayer graphene deposition. The intermediate graphene layer does not have a significant impact on the baseline wettability of the underlying substrate. (b) Water contact angle measurements on Cu substrates with varying number of graphene layers. There is  $< 0.7\%$  change in contact angle of the Cu substrate due to the presence of monolayer graphene. Beyond 4 graphene layers there is a sharp decrease in the wettability with the water contact angle finally saturating at the bulk graphite value for greater than 6 graphene layers. (c) Water contact angle measurements on glass with varying number of graphene layers. The wetting transparency effect of monolayer graphene that was seen for copper, gold and silicon is not observed on the glass substrate..... 7
- Figure 2 – Characterization of Cu nanorods surface with and without the graphene drape. (a) Scanning electron micrograph (SEM) of the aligned array of Cu nanorods deposited on a flat Si wafer by oblique angle sputter deposition. (b) Corresponding image of the same Cu nanorods surface after it has been draped with a single-layer graphene sheet. (c) Top view SEM image of the Cu nanorods surface. The darkened region represents the portion of the array that is draped while the lighter region is the undraped portion. (d) Typical Raman spectra of the graphene drape showing the Raman G ( $\sim 1584\text{ cm}^{-1}$ ) and 2D ( $\sim 2685\text{ cm}^{-1}$ ) band peaks that are characteristic of monolayer graphene. Note the strongly suppressed defect related D peak ( $\sim 1350\text{ cm}^{-1}$ ) that indicates high quality graphene..... 11
- Figure 3 – Contact angle hysteresis measurements. (a) Images of advancing and receding water drops on the Cu nanorods surface with and without the graphene drape. (b) Advancing and receding water contact angles of the drop plotted vs. the number of graphene layers in the drape. (c) Measured contact angle hysteresis plotted vs. the number of graphene layers in the drape..... 13
- Figure 4 – Droplet impact experiments. (a) Snapshots of a water droplet impacting the baseline Cu nanorods surface at a velocity of  $\sim 60\text{ cm/sec}$ . The droplet spreads into a pancake shape as its kinetic energy is converted into elastic strain energy in the drop, however during the receding phase, the water contact line gets strongly pinned to the

substrate, which results in large contact angle hysteresis. (b) Corresponding real-time snapshots of a similar sized water droplet striking the surface of the graphene draped Cu nanorods surface at a velocity of  $\sim 60$  cm/sec. In this case the droplet contact line does not get pinned to the surface and extends/contacts periodically as the droplet repeatedly advances and then recedes on the graphene draped surface. .... 17

Figure 5 – Non-dimensional drop contact length and dynamic contact angle during droplet impact. (a) Non-dimensional contact length (defined as the real-time contact length at the drop/substrate interface normalized by the final equilibrium contact length) plotted vs. time after impact. (b) Dynamic water contact angle (obtained by averaging the instantaneous, real-time contact angles on the left and right contact lines of the droplet) plotted vs. the time after impact. .... 19

Figure 6 – Molecular dynamics (MD) simulations. (a) A snapshot of a moving water droplet (the substrate is moving to the right) on a rough nano-textured Cu surface without a graphene drape (upper graph) and with a monolayer graphene drape (lower graph) during our molecular dynamics simulations. The porosity of the surface (projected area of the solid-liquid contacts divided by the total projected area of the droplet) is  $\sim 0.5$  which is similar to the experiments. (b) The friction force distribution for water droplet on bare patterned copper (upper graph) and graphene-coated patterned copper (lower graph). .... 21

Figure 7 – Monolayer graphene coating on hydrophobic electroplated copper substrate. (a) Flat Copper substrate. (b) Copper oxide grown on surface to create hierarchical roughness features. (c) Rough copper surface obtained after thermal annealing. (d) In-situ Chemical Vapor Deposition (CVD) used to grow monolayer graphene that provides a conformal coating for the hierarchical roughness features. (e) Water harvesting using the graphene protected, corrosion resistant hydrophobic copper surface. The graphene is wetting transparent and thus does not disturb the intrinsic hydrophobicity of the roughened underlying copper substrate ..... 26

Figure 8 – The wetting transparency and water repellency achieved by conformal coating of graphene on a roughened copper surface Scanning Electron Microscopy (SEM) images for (a) Baseline copper surface (Cu). (b) Electroplated copper oxide surface (h-Cu). (c) Electroplated and thermally annealed copper surface (h-rCu). (d)

Electroplated and thermally annealed copper surface after graphene growth using CVD (h-Gr/rCu). (e) Raman Spectra of graphene transferred to SiO<sub>2</sub>. (f) Water contact angle measurements on substrates (a)-(d).<sup>18</sup> ..... 29

Figure 9 – Improved resistance to oxidation for graphene coated hierarchical copper surface. X-Ray Photoelectron Spectroscopy analysis for Cu2P<sub>3/2</sub> and Cu2p<sub>1/2</sub> spectrum of (a) Flat copper. (b) Graphene coated flat copper. (c) Electroplated and thermally annealed Cu without graphene. (d) Electroplated and thermally annealed Cu with graphene. Upper spectra and inset photographs are taken before the annealing at 200°C for 4 hours in air, while the data and images below are taken afterwards.<sup>18</sup> ..... 32

Figure 10 – Graphene monolayer helps improve chemical stability and ensures sustained hydrophobicity in corrosive environments. Photographs of a water droplet were taken on (a) h-rCu and (b) h-Gr/rCu after immersion in a ~0.1 M NaCl aqueous solution over a period of 1-5 hours. (c) Static water contact angle variation from 0 to 5 hours of electrolyte immersion.<sup>18</sup> ..... 33

Figure 11 – Dehumidification for water harvesting (a) Droplet condensation experimental set-up. (b) Total condensate mass and dewetting ratio for the Cu, Gr/Cu, h-rCu and h-Gr/rCu surfaces. (c), (d) Filmwise condensation on bare copper (Cu) and copper with graphene coating (Gr/Cu). (e), (f) Drop wise condensation mode observed on electroplated/thermally annealed copper without (h-rCu) and with (h-Gr/rCu) graphene coating.<sup>18</sup> ..... 35

Figure 12 – (a) Photograph of a macroscopic 3D graphene foam network. The foam is flexible and can be easily handled and manipulated. (b) Raman spectra taken from several locations on the graphene foam clearly showing the Raman G band and 2D band peaks. Based on the ratio of the integrated intensity of the G and 2D bands, we conclude that the walls of the foam are comprised of mono- to few-layered graphene sheets. Note the absence of a defect related D band in the Raman spectrum which indicates the high quality of graphene sheets prepared using our chemical vapor deposition process. (c) Scanning electron microscopy (SEM) image of the micro-porous graphene foam showing average pore size of ~200 μm. (d) Teflon coated graphene foam showing similar pore structure and dimensions to the original graphene foam. The Teflon coating

thickness is estimated to be ~200 nm by Teflon coating on to a flat surface which was subsequently cleaved for cross-sectional SEM..... 42

Figure 13 – (a) Advancing liquid front for the Teflon coated graphene sample indicating an advancing water contact angle of ~163.01 degrees. (b) Receding liquid front on the same sample indicating a receding water contact angle of ~143.78 degrees. (c) Corresponding advancing contact angle on the baseline graphene foam (without Teflon coating) measured to be ~134.86 degrees. (d) Corresponding receding contact angle on the baseline graphene foam measured to be ~110.72 degrees. .... 43

Figure 14 – (a) Snapshots of a water droplet impacting the surface of the Teflon coated graphene foam. The impact velocity just prior to the droplet striking the surface was ~76 cm/sec. The sequence of snapshots shows the deformation time history of the droplet upon impact. The droplet spreads, then retracts and successfully rebounds off the surface. The coefficient of restitution (i.e. ratio of droplet impacting velocity to ejecting velocity) is ~0.37 for the Teflon coated foam. (b) Corresponding snapshots of a water droplet impacting on the surface of the baseline graphene foam (without Teflon coating). The impact velocity in this case was ~75 cm/s. For this case the droplet does not rebound off the surface. The droplet gets pinned to the substrate and pulsates on the surface as its kinetic energy is converted into internal modes of vibration and is eventually dissipated through viscosity..... 46

Figure 15 – (a) Time history of the droplet’s dynamic contact angle for the droplet impacting on the baseline graphene foam and the Teflon coated graphene foam samples. The impact velocity for both the samples is ~75 cm/s. (b) Normalized contact line length vs. time for droplets impinging on the baseline graphene foam and the Teflon coated foam with a velocity of ~75 cm/s. .... 47

Figure 16 – (a) Schematic of the thermal reduction/sulfurization method used to deposit WS<sub>2</sub> sheets. (b) (Top) schematic of monolayer WS<sub>2</sub> film on Si/SiO<sub>2</sub> substrate, (bottom) Optical microscopy image of large area, continuous WS<sub>2</sub> film on SiO<sub>2</sub>/Si substrate, and this image is taken near the edge of the film showing the covered and exposed regions on the SiO<sub>2</sub> substrate. (c) (Top) Atomic force microscopy and (Bottom) scanning electron microscopy images of the edge region of the WS<sub>2</sub> film. (d) Atomic force microscopy line scan showing the height of the WS<sub>2</sub> monolayer film as ~ 1 nm. .... 56

Figure 17 – (a) Raman spectroscopy characterization (at 532 nm excitation) of monolayer, bi-layer and tri-layer WS<sub>2</sub> films on Si/SiO<sub>2</sub> wafer. (b) Difference in the frequency of various Raman active modes vs. the number of layers (mono, bi and tri) in the WS<sub>2</sub> film. .... 58

Figure 18 – (a) Static water contact angle measurements for WS<sub>2</sub> films with varying number of layers on Si/SiO<sub>2</sub> substrate. (b) Aging dynamics of a monolayer WS<sub>2</sub> film showing the formation of a hydrocarbon layer that increases the water contact angle over time. .... 61

Figure 19 – (a) Schematic of chalcogen substitution with oxygen using argon plasma treatment. (b) XPS analysis of Ar plasma treated WS<sub>2</sub> showing removal of sulfur atoms with progressive plasma deposition time; the sulfur appear to be removed from the top surface of the film that is exposed to the plasma. (c) (Top) Condensation of water drops on untreated WS<sub>2</sub>, (Bottom) Condensation on plasma-patterned WS<sub>2</sub> surface. (d) Top and bottom show corresponding condensation results for a monolayer MoS<sub>2</sub> film. .... 64

Figure 20 – Graphite to Graphene production (a) Process flow schematic for the creation of graphene platelets with different aspect ratios and thicknesses in water-based synthetic cutting oils. (b) Modified Hummer’s method over oxidizes the graphite as compared to Staudenmaier method, which exhibits lesser expanded when interlayer spacing is analyzed using X-Ray Diffraction.<sup>10</sup> ..... 71

Figure 21 – SEM image analysis of graphene platelets. (a) Reduced graphene oxide exfoliated at 500 °C. (b) Reduced graphene oxide exfoliated at 1050°C. (c) Ultrasonicated graphene oxide sheets. Agglomeration of TR-GO flakes ex-situ mandates use of alternate techniques to analyze in-situ dimensionality of these flakes.<sup>10</sup> ..... 72

Figure 22 – Dynamic Light Scattering (DLS) data for various functionalized graphene platelets (a) Ultrasonicated graphene oxide produced via Modified Hummer's method shows the smallest hydrodynamic diameter with a mean of ~120 nm owing to electrostatic repulsion of sheets. (b) TR-GO 500°C shows larger flakes in dispersion as a result of lesser oxygen functional groups and more hydrophobic nature. (c) TR-GO 1050°C agglomerates further as higher temperature thermal exfoliation reduces oxygen moieties to a great extent and the sheets become highly hydrophobic.<sup>10</sup> ..... 74

Figure 23 – Carboxyl Graphene Platelets (GPL) analyzed using (a) Scanning Electron Microscope (SEM) imaging. (b) X-Ray Photoelectron Spectroscopy indicates prominent peaks at ~286 eV for hydroxyl and ~289 eV for carboxyl functional groups attached to the basal plane of graphene.<sup>10</sup> ..... 77

Figure 24 – Varying concentrations of carboxyl graphene dispersed in canola oil positively impact critical parameters for metal cutting fluids. (a) Coefficient of Friction. (b) Kinematic Viscosity. (c) Thermal Conductivity.<sup>8</sup> ..... 79

Figure 25 – Schematic representation of a commercially available LiCoO<sub>2</sub> - Graphite Li-Ion Cell. .... 86

Figure 26 – Photo-thermal reduction of graphene oxide sheets induces a rapid deoxygenation reaction resulting in the formation of freestanding graphene electrodes (a) Laser based raster scanning. (b) Xenon flash induced deoxygenation. (c) Freestanding electrode is found to be robust and flexible. (d) Top view showing cracks and pores created as a result of photo-thermally induced deoxygenation. .... 88

Figure 27 – A summary of performance characteristics for graphene based electrodes (a) Graphene anodic half-cells exhibit high capacities upto ~915 mAh/g over 1000 cycles. (b) Cathodic half cells are compared with commercially available cathodes and achieve ~815 mAh/g. (c) Graphene electrodes demonstrate extremely high rate capability with appreciable capacities observed at rates up to 150 C. (d) A Ragone Chart comparing this battery technology with state-of-the art energy storage devices including batteries and electrochemical capacitors<sup>22,23</sup> ..... 89

Figure 28 – (a) Schematic representing graphite oxidation to graphite oxide and its result on interlayer spacing. (b) X-Ray diffraction of Graphite Oxide produced using Modified Hummer’s method shows a prominent peak at ~11 deg (as opposed to ~27° for pristine graphite) indicating a larger interlayer spacing of ~1.1 nm (as opposed to 0.34 nm for pristine graphite). .... 92

Figure 29 – (a) Profiles for change in current and resistance as a function of time during the electro deposition of graphene oxide. (b) Roll-to-Roll electrodeposition setup built for graphene oxide electrodeposition. (c) Image of a large area freestanding graphene oxide sheet. (d) Cross-sectional SEM image of synthesized graphene oxide paper. (e) Schematic representation of All-Carbon lithium ion cell using graphene anodes and

graphene-lithium composite cathodes. (f) Image of 20 mAh pouch cell built using graphene based electrodes powering an LED. Electroplating offers a drastic reduction in production time, leading to faster processing for industrial scale electrodes, with high achievable mass loadings. Flexibility with lateral dimensions enables device scale prototypes.<sup>23</sup> ..... 94

## ACKNOWLEDGMENT

Graduate school has been a marvelous journey, and I have learnt a great deal from my peers, professors, and various other people that I encountered along the way. I would like to begin by thanking my thesis advisor and mentor, Prof. Nikhil Koratkar. His support and encouragement were critical in enabling me to pursue knowledge in the field of my choice. He has a very open approach to how graduate students in his lab work, and he inspires us to think critically and examine problems on our own. I would also like to thank my committee members, Prof. Johnson Samuel, Prof. Jie Lian and Prof. Yunfeng Shi for their valuable feedback and guidance through this effort.

My friends and family have also been incredibly supportive through these formative years. My grandfather, Dr. Jagannath Singh, nurtured my curiosity in the world around us from an early age and made me the inquisitive individual that I am today. My parents, Dr. Anil Kumar Singh and Dr. Archana Singh, and my sister Shuchi, have all been there for me as a constant source of support and advice, and this would not have been possible without them.

I would also like to extend a special thanks to my friends from school, undergraduate and graduate years. Thank you Shashank, Tushar, and Shobhit among others for making school life fun and exciting; and Nishant, Sagnik and Lokesh for the strangest conversations during my undergraduate years that led me to consider a life in technology. Graduate school would also have not been as easy if it wasn't for all the friends that I made here. Thanks a lot to Hannes, Michelle, Andy, Stacy, Aditya, Shruti, Amba and Bhaskar for the great times we have had together. My seniors and colleagues at RPI really made this a great experience as well – Abhay, Rahul, Ajay, Jian, Phil, Trevor, Kayvan, Ardavan, Fazel – it was really amazing to work with and learn from you. Lastly, a special mention and thank you to Sumitra, who has been a pillar of encouragement and support since my very first year here at Rensselaer. This period in Troy would just not have been the same without her and I really feel glad to have her by my side through this period of my life.

## ABSTRACT

This work deals primarily with the wettability of 2-dimensional nanomaterials including graphene and transition metal dichalcogenides, such as WS<sub>2</sub> and MoS<sub>2</sub>. The understanding developed through various experiments is subsequently applied to enable novel technologies using these materials.

Graphene is first investigated for its notable wetting transparency effect. Water droplets have been found to actually “see-through” extremely thin monolayers of carbon atoms draped over a planar surface, with the wetting behavior being influenced by the underlying substrate. This interaction is dependent on the surface chemistry of the support layer, in addition to its morphology. Subsequently, the effect of graphene coatings on roughened architectures is studied. Rough and porous substrates often entrap air-pockets that make them water repellent or hydrophobic. Sheer graphene monolayers that are draped over rough nanostructures are found to be useful in terms of lowering surface friction, thus leading to enhanced droplet mobility. However, non-conformal coatings are found to limit the water contact angle by blocking pores and roughness features that provide water repellency in the first place. This is not the case with a conformal graphene coating though, which improves chemical stability while maintaining its wetting transparent nature at a local level. Thus, highly hydrophobic surfaces may be created and passivated with the use of atomically thin graphene sheets, enabling a host of applications such as water condensation, electrowetting and nanofluidics.

The work then goes on to discuss how 3-dimensional graphene macrostructures may be synthesized and used as superhydrophobic foams that exhibit water contact angles greater than  $\sim 150^\circ$ . These foams were found to maintain the superhydrophobic state even under harsh conditions such as droplet impact, and water droplets were found to rebound off the surface. This is attributed to the robust and elastic nature of graphene foams assembled in a 3-dimensional architecture.

Having characterized the behavior of graphene, monolayer transition metal dichalcogenides are investigated next. These 2D layered materials are very intriguing, given their direct band-gap and interesting optical and electronic attributes. Studying their wetting behavior led to the understanding that simple continuum models that predict wetting opacity for these monolayers are not entirely accurate. The transparency effect is

observed with WS<sub>2</sub> and MoS<sub>2</sub> monolayers exhibiting partial wetting transparency. Observed water contact angle values for monolayers were ~82°, with bulk samples following the theoretically predicted values more closely at around ~90°. Furthermore, it is found that the substitution of chalcogen atoms (S) with their more hydrophilic counterparts such as oxygen, could allow for the development of micro-patterned arrays with specific hydrophilic/hydrophobic regions.

The last chapter focuses on using wetting science to predict the behavior of these nanosheets and apply these concepts towards the development of real world applications. First, graphene sheets are functionalized to enhance dispersibility in semi-synthetic and plant derived cutting oils, and improve their performance in micro-machining environments. Using graphene sheets as an additive mitigates high cutting forces and temperatures.

Finally, the role of graphene electrodes in next-generation energy storage devices is discussed. Although, there is intense research activity with respect to the performance of graphene-based electrodes, the scalability of nanomaterials is a major roadblock to commercial applications. A novel electrodeposition technique is developed, that utilizes the behavior and surface charge of functionalized graphenes in aqueous environments to enable rapid, scalable production of graphene macrostructures. Electrode materials were synthesized using this process and initially tested as anodes in lithium-ion batteries. Furthermore, graphene-lithium composite electrodes are also synthesized using these materials, enabling the realization of a unique All-Carbon chemistry for lithium-ion cells. These electrodes have extremely high power densities of ~30 kW/kg, allowing rapid charge and discharge, while providing high energy densities of ~650 Wh/kg. Maintaining these attributes, achieved through the nanoscale dimensionality of graphene, is a challenge when scaling the thickness and areal mass loading to industrially desirable levels of ~ 5 mg /cm<sup>2</sup>. Electrodeposition of graphene-based materials is demonstrated as an industrially viable process that allows for quick build-up in thickness, facilitating higher mass loadings, while the retaining the critical performance parameters.

# 1. Introduction

This work attempts to understand the intrinsic wetting behavior of 2-dimensional nanomaterials such as graphene and transition metal dichalcogenides, and eventually apply those concepts towards the development of practical applications. Since the discovery of graphene in 2004 by Andre Geim and Konstantin Novoselov, various forms of monolayer and multilayer graphene have been described in literature<sup>1-4</sup>. The nanoscale dimensions bring a wide array of distinct advantages such as high specific surface area, chemical stability, mechanical strength, high thermal and electrical conductivity, optical transparency and a tunable bandgap<sup>5-8</sup>. 2-dimensional nanomaterials have since expanded in scope to include transition metal dichalcogenides that have unique electronic and optical attributes that stem from a direct band-gap, which is absent in graphene<sup>9-10</sup>.

## 1.1 Objectives of this Study

Understanding wetting phenomena and the molecular interactions of liquids with these 2-dimensional nanomaterials is critical information for engineers developing various technologies. The wettability of a nanomaterial significantly impacts its applicability in any field. The synthesis of composites, creating lubricant additives, casting films or coatings and even deposition processes such as printing or spraying require the creation of stable dispersions to enable production at meaningful scales<sup>11-14</sup>. Nanomaterials must be manipulated and assembled into macro-scale structures without compromising on their nanoscale advantages. The agglomeration of nanosheets within a dispersion leads to the manifestation of bulk characteristics, which degrades the final performance in any potential application. Developing processing techniques that are compatible with the basic wetting nature of these 2D layers is therefore crucial if we wish to leverage the tremendous potential nanoscale materials offer.

In addition to developing wettable nanosheets for easier handling and synthesis, molecular interactions with liquids are also very important from a direct application perspective. Superhydrophobic surfaces that exhibit the “lotus leaf” effect by strongly repelling water droplets are very attractive for the development and realization of self-cleaning surfaces, water harvesting technologies, protective coatings, and also nanofluid-

ics and electrowetting applications<sup>15-18</sup>. Electrodes for energy storage applications need to be tailored for good electrolyte wettability since that improves electron transfer kinetics and reduces interfacial charge transfer resistance<sup>19-20</sup>.

This work attempts to advance the fundamental understanding related to the interaction of liquids at atomic scales with 2 dimensional nanomaterials. The applicability of these concepts to the development of various applications is also explored. First, the effect of substrate morphology on supported graphene's wettability is thoroughly understood. In addition to flat planar surfaces, the behavior is also characterized with respect to roughened underlying substrates. Non-conformal graphene coatings were found to exhibit wetting opacity; whereas an in-situ conformal coating of graphene allows the monolayer to maintain wetting transparency, even for strongly hydrophobic surfaces. This proves useful in devices for condensation and water harvesting applications. Following the discussion on supported graphene, unsupported 3 dimensional macrostructures of porous graphene are synthesized and tested as elastic, super-hydrophobic foams.

Beyond graphene, Chapter 4 goes on to discuss another class of 2D layered nanomaterials that include transition metal dichalcogenides (TMD's) such as WS<sub>2</sub> and MoS<sub>2</sub>. Monolayers were shown to exhibit a certain degree of wetting transparency, in contrast with the predictions of simple continuum models. The effects of aging and hydrocarbon contamination were also investigated. It is shown that clean (i.e. non-aged) monolayers of TMD's are much more hydrophilic than previously thought. It is also shown, that by replacing sulfur atoms with oxygen atoms in the TMD lattice, patterned hydrophilic/hydrophobic regions may be created, facilitating the formation of micro-drop arrays during condensation and water evaporation experiments.

Chapter 5 focuses on the development of two diverse applications using knowledge about their wetting behavior. First, few-layered graphene is used as an additive to enable sustainable, plant-derived metal cutting oils. Stable dispersions are created using functionalized graphene sheets that avoid agglomeration in canola oil. In the second subchapter, electrode materials for energy storage devices are synthesized. Freestanding, 3-dimensional, porous graphene networks are produced using an electrodeposition approach. Upon photothermal reduction, the graphene networks produced are found to

exhibit enhanced electrolyte wettability and faster lithium ion diffusion. Nanomaterial processing techniques are developed by taking advantage of the 2-dimensional atomic crystals wetting behavior in aqueous environments. This led to the invention of a novel manufacturing technique that supports nanomaterial assembly into macrostructures, paving the path towards commercialization.

## 1.2 References

1. Geim, A. K., & Novoselov, K. S. The rise of graphene. *Nat. Mater.* **6**, 183-191 (2007).
2. Neto, A. C., Guinea, F., Peres, N. M. R., Novoselov, K. S., & Geim, A. K. The electronic properties of graphene. *Rev. Mod. Phys.* **81**, 109 (2009).
3. Meyer, J. C. *et al.* The structure of suspended graphene sheets. *Nature* **446**, 60-63 (2007).
4. McAllister, M. J. *et al.* Single sheet functionalized graphene by oxidation and thermal expansion of graphite. *Chem. of Mater.* **19**, 4396-4404 (2007).
5. Balandin, A. A. *et al.* Superior thermal conductivity of single-layer graphene. *Nano Lett.* **8**, 902-907 (2008).
6. Frank, I. W., Tanenbaum, D. M., Van der Zande, A. M., & McEuen, P. L. Mechanical properties of suspended graphene sheets. *J. Vac. Sci, Technol. B* **25**, 2558-2561 (2007).
7. Zhang, Y. *et al.* Direct observation of a widely tunable bandgap in bilayer graphene. *Nature* **459**, 820-823 (2009).
8. Jung, I., Dikin, D. A., Piner, R. D., & Ruoff, R. S. Tunable electrical conductivity of individual graphene oxide sheets reduced at “low” temperatures. *Nano Lett.* **8**, 4283-4287 (2008).
9. Wang, Q. H., Kalantar-Zadeh, K., Kis, A., Coleman, J. N., & Strano, M. S. Electronics and optoelectronics of two-dimensional transition metal dichalcogenides. *Nat. Nanotechnol.* **7**, 699-712 (2012).
10. Chhowalla, M. *et al.* The chemistry of two-dimensional layered transition metal dichalcogenide nanosheets. *Nat. Chem.* **5**, 263-275 (2013).
11. Stankovich, S. *et al.* Graphene-based composite materials. *Nature* **442**, 282-286 (2006).
12. Samuel, J., Rafiee, J., Dhiman, P., Yu, Z. Z., & Koratkar, N. Graphene colloidal suspensions as high performance semi-synthetic metal-working fluids. *J. Phys. Chem. C.* **115**, 3410-3415 (2011).
13. Li, D., Müller, M. B., Gilje, S., Kaner, R. B., & Wallace, G. G. Processable aqueous dispersions of graphene nanosheets. *Nat. Nanotechnol.* **3**, 101-105 (2008).
14. Gilje, S., Han, S., Wang, M., Wang, K. L., & Kaner, R. B. A chemical route to graphene for device applications. *Nano Lett.* **7**, 3394-3398 (2007).
15. Bhushan, B., & Jung, Y. C. Natural and biomimetic artificial surfaces for superhydrophobicity, self-cleaning, low adhesion, and drag reduction. *Prog. Mater. Sci.* **56**, 1-108 (2011).
16. Rauscher, M., & Dietrich, S. Wetting phenomena in nanofluidics. *Annu. Rev. Mater. Res.* **38**, 143-172 (2008).
17. Pollack, M. G., Fair, R. B., & Shenderov, A. D. Electrowetting-based actuation of liquid droplets for microfluidic applications. *Appl. Phys. Lett.* **77**, 1725-1726 (2000).

18. Mugele, F., & Baret, J. C. Electrowetting: from basics to applications. *J. Phys-Condens. Mat.* **17**, R705 (2005).
19. Wang, C., Li, D., Too, C. O., & Wallace, G. G. Electrochemical properties of graphene paper electrodes used in lithium batteries. *Chem. Mater.* **21**, 2604-2606 (2009).
20. Stoller, M. D., Park, S., Zhu, Y., An, J., & Ruoff, R. S. Graphene-based ultracapacitors. *Nano Lett.* **8**, 3498-3502 (2008).

## 2. The Wetting of Supported Graphene

### 2.1 Graphene on Flat Surfaces

In 2012, our group published a report on the “wetting transparency” of graphene<sup>1</sup>. Since it is extremely difficult to measure the wetting contact angle for a single layer of graphene in isolation, this work focused on how graphene behaves when placed on flat surfaces with different wetting characteristics. It was demonstrated that a single layer of graphene is transparent to water droplets and does not disrupt the intrinsic wetting behavior of the underlying substrate in certain situations. Such transparency for any material had never been reported before and was a unique observation in the field of wetting. When the water-substrate interaction is dominated by Van Der Waals forces such as in the case of silicon, gold and copper, a graphene monolayer allows for cross talk between the water and substrate. Van Der Waals forces usually vanish quickly over long distances; however the extreme thinness of a graphene monolayer (~0.34 nm) allows water molecules to interact with the underlying surface. In the case of short-range chemical bonding, such as water-glass interfaces, graphene disrupts the wetting behavior significantly since it prevents this chemical interaction.

Water contact angles (WCA) were used to quantify the wettability of these surfaces. The contact angle of a droplet is defined as the angle between the solid-liquid interface line and a tangential line moving along the liquid-vapor interface, beginning at the edge of the droplet. When the wetting of a surface is favorable water droplets will spread out on the surface and contact angle will be low. Surfaces with WCA below 90° are considered hydrophilic while those with WCA above 90° are termed hydrophobic. A higher contact angle is observed when wetting is unfavorable, causing the fluid to minimize its contact with the solid surface.

---

Portions of this chapter previously appeared as: Singh, E. *et al.* Graphene Drape Minimizes the Pinning and Hysteresis of Water Drops on Nanotextured Rough Surfaces. *ACS Nano* **7**, 3512-3521 (2013).

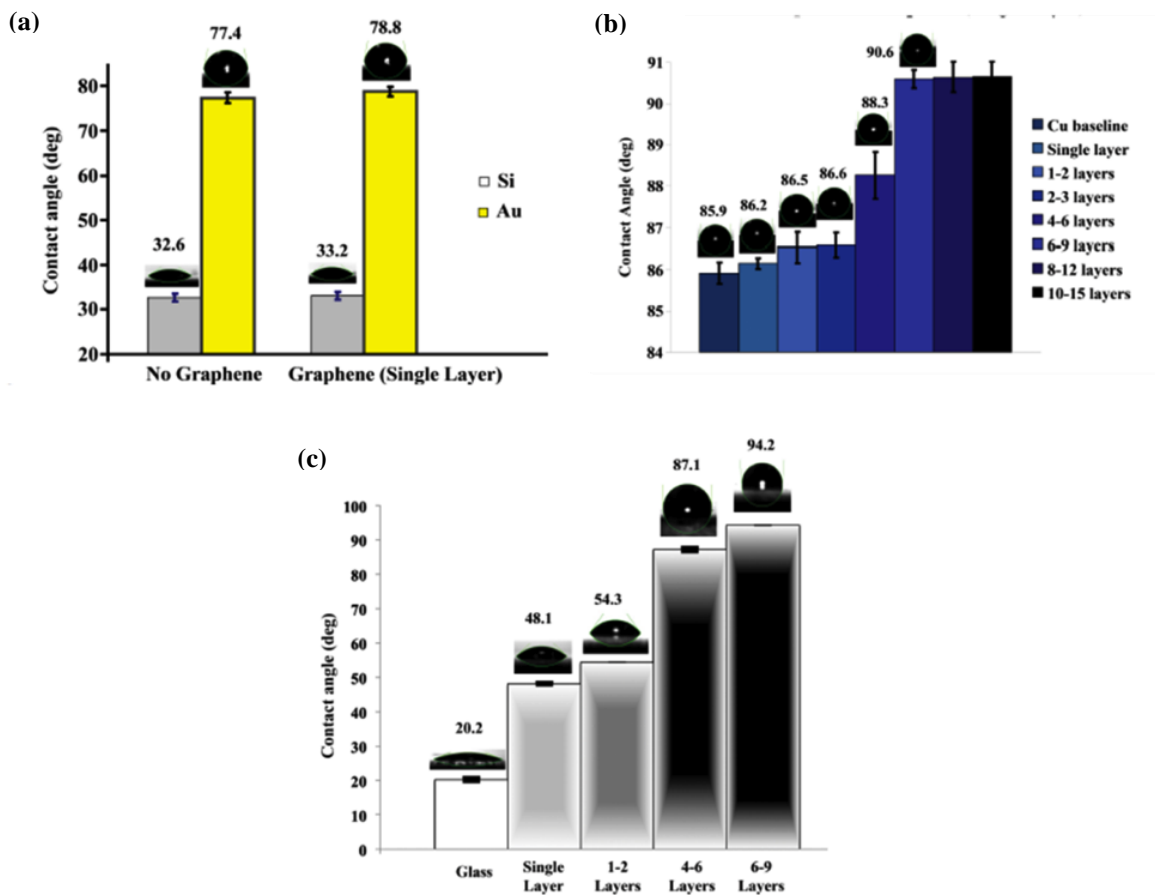


**Figure 1 – Wetting transparency of graphene. (a) Water contact angle measurements for Si and Au substrates with and without monolayer graphene deposition. The intermediate graphene layer does not have a significant impact on the baseline wettability of the underlying substrate. (b) Water contact angle measurements on Cu substrates with varying number of graphene layers. There is < 0.7% change in contact angle of the Cu substrate due to the presence of monolayer graphene. Beyond 4 graphene layers there is a sharp decrease in the wettability with the water contact angle finally saturating at the bulk graphite value for greater than 6 graphene layers. (c) Water contact angle measurements on glass with varying number of graphene layers. The wetting transparency effect of monolayer graphene that was seen for copper, gold and silicon is not observed on the glass substrate.**

Reprinted by permission from Macmillan Publishers Ltd: Nature Materials “Rafiee, J. *et al.* Wetting transparency of graphene *Nat. Mater.* 11, 217-222 (2012)”, Copyright © 2012.

The transparency effect was experimentally demonstrated by coating a graphene monolayer on silicon (Si) and ~300 nm thick gold (Au) film on Si. As shown in Figure 1(a), the baseline contact angles are ~32.6° and 77.4°. A graphene monolayer results in just 1-2% increase in the contact angle implying that interaction of water molecules with the substrate is still taking place. The effect of coating thickness is clearly seen in Figure 1(b) by covering copper with single and multilayer graphene. Bare copper has a contact

angle of  $\sim 85.9^\circ$  and it rises by  $\sim 0.7\%$  to  $86.2^\circ$  when coated with single layer graphene. With 2-3 layers the value rises gradually to  $\sim 86.6^\circ$ . With 4 layers and more there is a dramatic increase to  $\sim 88.3^\circ$  and by 6 layers the contact angle approaches  $\sim 90.6^\circ$ , the bulk value for graphite. These results indicate that a monolayer of graphene is transparent to the substrate's effect on water molecules.

Interestingly, the transparency effect does not extend to situations where the wetting is dominated by short-range chemical interactions such as hydrogen bonding. When glass ( $\text{SiO}_2$ ) was coated with graphene the contact angle changed pretty significantly as is seen in **Figure 1(c)**. Bare glass with no graphene was cleaned by piranha etching and the water contact angle was observed to be  $\sim 20.2$ . A monolayer of graphene results in a sharp increase to  $\sim 48.1$  with multiple layers bringing it up to  $\sim 94$ . Theoretical calculations and molecular dynamics simulations confirmed these experimental observations. Soon after this study, Strano and Blankschtein looked at this behavior in greater detail and reported other situations where the wetting transparency breaks down<sup>2</sup>. Notably, this occurred on superhydrophilic surfaces, where interaction was dominated by chemical bonding, as well as on superhydrophobic surfaces. In the superhydrophobic case they demonstrate that the graphene itself limits the maximum possible contact angle when covering a superhydrophobic surface, since water molecules are attracted more to carbon atoms than the underlying substrate. It is akin to decoupling graphene from its substrate and capturing the 2D sheets intrinsic wetting behavior by forcing the water molecules to interact only with carbon atoms. This prompted the question of how wetting behavior would be impacted if graphene sheets were draped on a nanotextured rough surface.

## 2.2 Non-Conformal Coating of Graphene on Rough Surfaces

### 2.2.1 Introduction

Previous studies of the interaction of water with graphene-coated surfaces have been limited to flat (smooth) surfaces. Here we created a rough surface by nano-patterning and then draped the surface with a single-layer graphene sheet<sup>3</sup>. We found that the ultra-sheer graphene drape prevents the penetration of water into the textured surface thereby drastically reducing the contact angle hysteresis (which is a measure of frictional energy dissipation) and preventing the liquid contact line from getting pinned to the substrate. This has important technological implications since the main obstacle to the motion of liquid drops on rough surfaces is contact angle hysteresis and contact line pinning.

Graphene drapes could therefore enable enhanced droplet mobility, which is required in a wide range of applications in micro and nano-fluidics. Compared to polymer coatings that could fill the cavities between the nano/micro pores or significantly alter the roughness profile of the substrate, graphene provides the thinnest (i.e. most sheer) and most conformal drape that is imaginable. In spite of its extreme thinness, the graphene drape is mechanically robust, chemically stable and offers high flexibility and resilience which can enable it to reliably drape arbitrarily complex surface topologies. Graphene drapes may therefore provide a hitherto unavailable ability to tailor the dynamic wettability of surfaces for a variety of applications.

The motion of water drops on solid surfaces is required in many applications including lab-on-chip devices, bio-medical applications, high throughput assays, surfaces for drop-wise condensation, water harvesting, low-friction coatings, self-cleaning and anti-fouling surfaces<sup>4-6</sup>. The key to successfully moving water drops on surfaces is to reduce the adhesion of water with the surface. This can be achieved by tailoring the chemistry of the surface or its roughness<sup>7-8</sup>. Many studies have utilized micro or nanoscale surface roughness features to entrap air pockets underneath the water droplet<sup>9-10</sup>. Under static conditions such surface roughness features are effective in supporting the water drop in a suspended (Cassie) state<sup>11</sup>, which results in weak surface adhesion. However under dynamic conditions (e.g. droplet motion or impact), water drops can possess sufficient kinetic energy to penetrate into these roughness features and force out the entrapped air; this is called the Wenzel State<sup>12</sup>. Such Cassie-to-Wenzel state transition pins the drop to

the surface and generates large differences between the advancing and receding water contact angles (contact angle hysteresis), which is a measure of the friction at the droplet-substrate interface. Here we show using both experiments and modeling that droplet pinning and contact angle hysteresis on rough surfaces can be dramatically reduced by draping an ultra-thin and flexible monolayer graphene sheet over the surface. This has important implications for the design of ultra-thin and minimally invasive coating materials that enhance droplet mobility on textured (rough) surfaces.

### 2.2.2 Graphene Draped Nanostructures

The nano-textured (rough) surface in our study is comprised of an aligned array of Copper (Cu) nanorods (Figure 2 – Characterization of Cu nanorods surface with and without the graphene drape. (a) Scanning electron micrograph (SEM) of the aligned array of Cu nanorods deposited on a flat Si wafer by oblique angle sputter deposition. (b) Corresponding image of the same Cu nanorods surface after it has been draped with a single-layer graphene sheet. (c) Top view SEM image of the Cu nanorods surface. The darkened region represents the portion of the array that is draped while the lighter region is the undraped portion. (d) Typical Raman spectra of the graphene drape showing the Raman G ( $\sim 1584 \text{ cm}^{-1}$ ) and 2D ( $\sim 2685 \text{ cm}^{-1}$ ) band peaks that are characteristic of monolayer graphene. Note the strongly suppressed defect related D peak ( $\sim 1350 \text{ cm}^{-1}$ ) that indicates high quality graphene.) that are deposited on a flat silicon wafer using oblique angle sputter deposition (Materials and Methods)<sup>13-14</sup>. The average height of the Cu nanorods is  $\sim 200 \text{ nm}$ , with a maximum diameter of  $\sim 50 \text{ nm}$  (at the fanned out section at the top) and a minimum diameter of  $\sim 20 \text{ nm}$  (at the base). The average wall-to-wall spacing between the Cu nanorods is  $\sim 30 \text{ nm}$  (Figure 2c). The water contact angle for the Cu nanorods surface can be predicted by using the well-established Cassie and Baxter equation<sup>31</sup>.  $\cos\theta_c = f(\cos\theta_o + 1) - 1$ , where  $\theta_o$  is the contact angle on a flat Cu surface,  $\theta_c$  is the apparent contact angle and  $f$  is the porosity, expressed as the projected area of the solid-liquid contacts divided by the total projected area of the droplet.

Based on image analysis from SEM observations (Figure 2c), the porosity,  $f = 0.54$ . The water contact angle measured on a flat Cu film ( $\theta_o$ ) deposited under the same conditions as the Cu nanorods was  $\sim 86^\circ$ . Note that a pristine (perfectly clean) Cu surface

should show zero water contact angle<sup>15</sup> but in practice formation of passivation layers<sup>16</sup> (typically CuO and Cu<sub>2</sub>O) result in larger contact angles. By substituting  $\theta_0 = 86^\circ$  for Cu, we get a predicted water contact angle,  $\theta_c$  of  $115.24^\circ$  for the Cu nanorods array, which shows good agreement with the experimental static water contact angle value which was  $\sim 114 \pm 2$  degrees. This confirms that when water droplets are gently released on the surface of the Cu nanorods array, they lie in the suspended Cassie state due to the entrapped air pockets formed within the porous Cu nanorod network.

Next, we draped the Cu nanorods surface with a monolayer graphene sheet as indicated in Figure 2b. We synthesized monolayer graphene by chemical vapor deposition (CVD) on Cu foils using methane as the feedstock<sup>16</sup> (Materials and Methods). After growth, a thin poly-methyl-methacrylate (PMMA) film was coated on the graphene/Cu substrate. The Cu substrate was etched in dilute ammonium persulfate (0.25 M), and the graphene/PMMA film was transferred onto the Cu nanorods array.

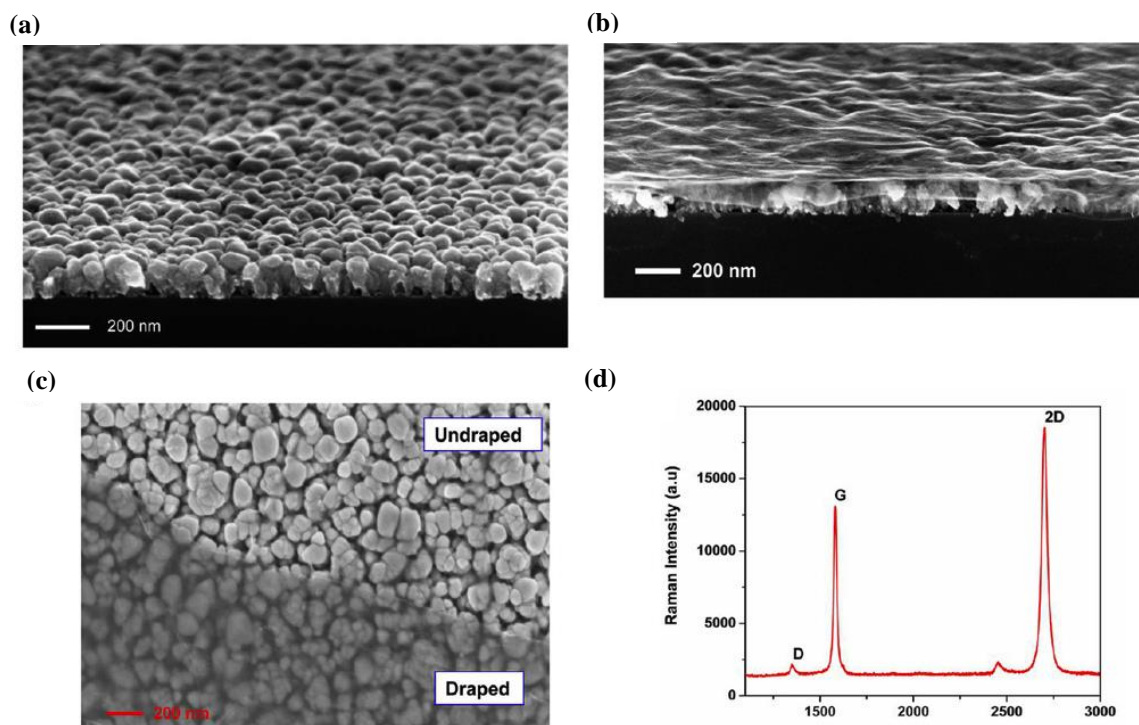


**Figure 2 – Characterization of Cu nanorods surface with and without the graphene drape. (a) Scanning electron micrograph (SEM) of the aligned array of Cu nanorods deposited on a flat Si wafer by oblique angle sputter deposition. (b) Corresponding image of the same Cu nanorods surface after it has been draped with a single-layer graphene sheet. (c) Top view SEM image of the Cu nanorods surface. The darkened region represents the portion of the array that is draped while the lighter region is the undraped portion. (d) Typical Raman spectra of the graphene drape showing the Raman G ( $\sim 1584 \text{ cm}^{-1}$ ) and 2D ( $\sim 2685 \text{ cm}^{-1}$ ) band peaks that are characteristic of monolayer graphene. Note the strongly suppressed defect related D peak ( $\sim 1350 \text{ cm}^{-1}$ ) that indicates high quality graphene.**

The scanning electron microscopy (SEM) image in Figure 2b shows a typical image of the Cu nanorods surface draped with a monolayer graphene sheet. The graphene drape uniformly covers the entire surface and there is no indication of any cracks or tears in the drape. The extreme thinness and flexibility of the drape also enables it to conform to the surface topology of the Cu nanorod tips. A typical top view SEM image of the graphene draped Cu nanorods surface is shown in Figure 2c. The contrast between the portion of the surface that is draped by the monolayer graphene and the part that lies exposed is evident. To confirm that the graphene that we are using is monolayer, we used Raman spectroscopy to measure the characteristic Raman G, and 2D bands (Figure 2d). The ratio of the integrated intensity of the Raman G and 2D peaks ( $\sim 0.4$ ), the position of the 2D peak at  $\sim 2685$   $\text{cm}^{-1}$  and the full width at half maximum ( $\sim 32$   $\text{cm}^{-1}$ ) of the 2D peak are all consistent with the literature for single-layer graphene grown by chemical vapor deposition on Cu foils.

### **2.2.3 Water Contact Angle Measurements**

Advancing and receding water contact angle measurements were performed using a 500-F4 Rame-Hart goniometer for images and the low-bond axisymmetric drop shape analysis technique was used to determine the contact angles (Materials and Methods). In the experiments a  $\sim 1$   $\mu\text{l}$  volume water drop was brought in contact with the surface and subsequently the volume of the drop was increased and then decreased to advance and retract the liquid front. This was repeated several times to check the reproducibility of the results. Figure 3a shows the advancing and receding conditions created by dispensing and retracting water at a rate of  $\sim 0.40$   $\mu\text{l/s}$  for the Cu nanorods surface with and without a monolayer graphene drape. It is evident that the graphene drape has a ‘dramatic’ influence on the receding liquid front. Without the drape the liquid front gets strongly pinned to the solid surface, which lowers the receding water contact angle to nearly zero degrees. By contrast with the drape, the water drop is no longer pinned and is able to retract freely on the surface (Figure 3a).

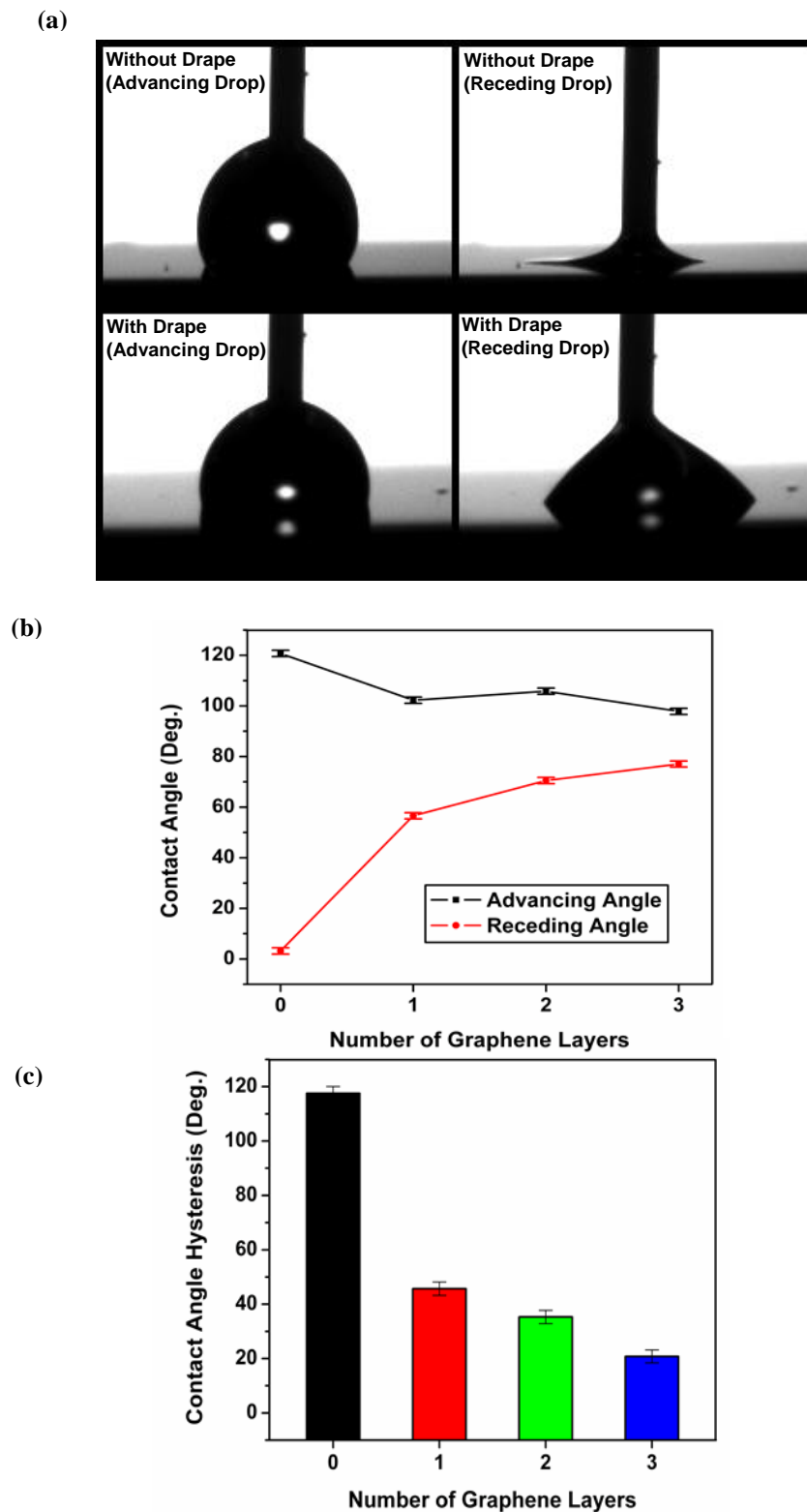


**Figure 3 – Contact angle hysteresis measurements. (a) Images of advancing and receding water drops on the Cu nanorods surface with and without the graphene drape. (b) Advancing and receding water contact angles of the drop plotted vs. the number of graphene layers in the drape. (c) Measured contact angle hysteresis plotted vs. the number of graphene layers in the drape.**

Additional measurements were performed by varying the number of graphene layers on the surface. For this multiple transfers were carried out to deposit bi-layer and then tri-layer graphene drapes on the Cu nanorods surface. The effect of the number of graphene layers in the drape on the advancing/receding contact angles is shown in Figure 3b. The advancing contact angle of the baseline Cu nanorods surface (without the drape) is  $\sim 120^\circ$ , while its receding contact angle is nearly zero degrees. With the monolayer graphene drape, the advancing water contact angle drops to  $\sim 102^\circ$ . This shows that on such strongly hydrophobic surfaces, even a single graphene layer fails to exhibit the wetting transparency effect that has been reported on flat surfaces at lower contact angles [1]. This deviation from wetting transparency has been explained by Strano, Blankschtein and co-workers<sup>2</sup> who showed that the water contact angle on an isolated mono-layer graphene sheet is  $\sim 96^\circ$ . Consequently, the maximum contact angle that can be achieved on any graphene draped surface (including the Cu nanorods surface) will be limited to  $\sim 96^\circ$ . Since the advancing contact angle is typically several degrees greater than the static value, the  $\sim 102^\circ$  advancing contact angle measured on the graphene-draped Cu nanorods surface is therefore consistent with the  $\sim 96^\circ$  static contact angle predicted in Reference 15. However the key observation from Figure 3b is that graphene draping results in a large increase in the receding water contact angle from nearly 0 degrees to  $\sim 60^\circ$ . With increasing number of graphene layers in the drape (i.e. for bi-layer and tri-layer coatings) the advancing contact angle remains fairly constant at  $\sim 100^\circ$ , while the receding contact angle continues to increase to  $\sim 70^\circ$  for bi-layer graphene and  $\sim 80^\circ$  for the tri-layer graphene drape. In figure 3c, we have plotted the contact angle hysteresis (which is the difference between the advancing and receding contact angles) vs. the number of graphene layers in the drape. The contact angle hysteresis falls sharply from  $\sim 120^\circ$  for the baseline Cu nanorods surface to  $\sim 45^\circ$  for the monolayer graphene drape and then continues to decrease with increasing number of graphene layers in the drape. For the tri-layer graphene drape, the contact angle hysteresis reduces to  $\sim 25^\circ$ .

The very high contact angle hysteresis observed for the baseline Cu nanorods surface is caused by a Cassie-to-Wenzel state transition, which occurs when the volume of the liquid drop is being increased (i.e. during the advancing phase). This can be understood by considering the critical pressure ( $P_c$ ) required to transition the water drop from

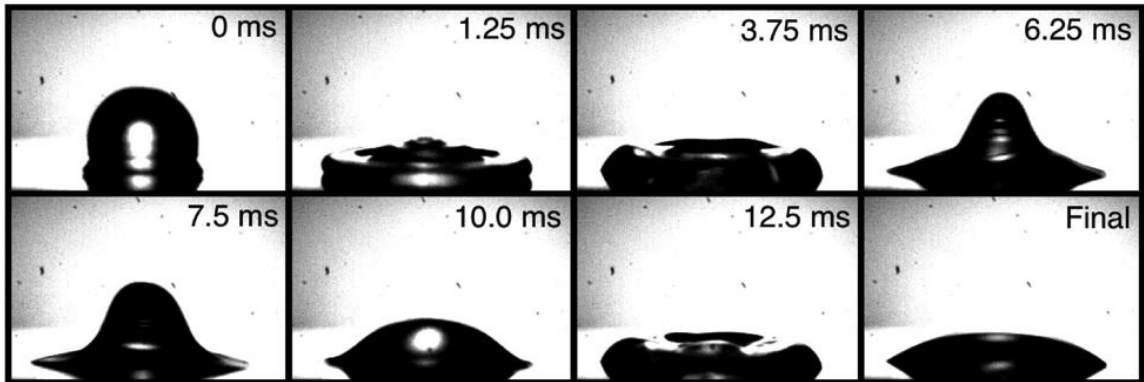
the Cassie to the Wenzel state:  $P_c = \frac{-\gamma \cos(\theta_o) \times L}{A}$  Here  $\gamma$  is the surface tension of water,  $L$  is the perimeter of the nano-pore formed between the Cu nanorods,  $A$  is the cross sectional area of the nano-pore and  $\theta_o$  is the water contact angle of the pore walls ( $\sim 86^\circ$  for Cu). Since  $\theta_o < 90^\circ$  (i.e.  $\cos(\theta_o) > 0$ ), the critical pressure is negative which implies that the Cassie state is inherently unstable, and therefore even a slight disturbance to the liquid drop (during the advancing phase) will cause the water to penetrate into the pores formed between the Cu nanorods. The net result of this is that all the entrapped air pockets formed in the nano-textured surface are expelled and the liquid drop now resides in the sticky Wenzel state. The droplet contact line is therefore strongly pinned to the surface and when the drop is retracted the receding contact angle remains close to zero to ensure that the contact length between the water drop and the substrate remains essentially unchanged.

Draping the Cu nanorods surface with a minimally invasive (ultra-sheer) but impermeable<sup>17</sup> graphene sheet appears to prevent water penetration into the nano-pores in the Cu nanorods surface. Consequently the liquid drop remains suspended on the top of the graphene draped Cu nanorods surface which prevents the contact line from getting pinned to the substrate roughness features (this increases the receding contact angle by  $\sim 60^\circ$  compared to the undraped surface). With increasing number of graphene layers in the drape, the receding water contact angle continues to increase and the contact angle hysteresis decreases further as shown in Figure 3b-c. We find using AFM that there was no large change in the rms roughness values as a function of the number of graphene layers in the drape. In addition to roughness, contact angle hysteresis also depends on defects on the surface, which can pin the water contact line. When we transfer the first layer of graphene, damage (e.g. nm size holes or cracks) could be more easily induced since it comes in direct contact with the sharp Cu nanorod tips. Subsequent layers of graphene will be less defective post-transfer due to the cushioning effect of the underlying sheets.

#### 2.2.4 Droplet Impact Experiments

Droplet impact tests were also performed to evaluate the ability of the graphene drape to prevent Cassie-to-Wenzel state transition under impact conditions. Droplets as large as 1-2 ml were dropped on the samples from a fixed height using a microsyringe to impact the surface at velocities ranging from 50 to 70 cm/sec. A high-speed camera (PhantomV4) operated at 800 frames per second with  $\sim 80 \mu\text{s}$  exposure time was used in this study. Time lapse images for the relevant advancing and receding stages of the droplets are shown in Figure 4 at an impact velocity of  $\sim 60$  cm/sec. For the baseline (i.e. undraped) Cu nanorods surface (Figure 4a), the droplet first deforms and flattens into a pancake shape (this is the advancing phase). However during the retraction phase the droplet gets strongly pinned to the substrate. This is evident in Figure 5a where we plot the real-time contact length of the droplet normalized by the equilibrium contact length of the same drop. The equilibrium contact length is measured after the drop is no longer in motion and has fully settled on the solid surface. Figure 5a indicates that without the drape the droplet expands to a maximum size (normalized contact length = 1.0) which occurs at  $\sim 1.25$  ms (which is the end of the advancing phase), but then at subsequent times the non-dimensional contact length remains fixed at  $\sim 1.0$  and does not reduce which confirms that the droplet is now pinned. By contrast on the Cu nanorods surface with the monolayer graphene drape (Figure 4b) the droplet spreads into a pancake shape but then retracts fully (see time = 12.5 ms in Fig. 4b) and does not get pinned to the substrate. In fact the contact line continues to advance and retract for several cycles as indicated by the sinusoidal fluctuations in the non-dimensional contact length of the drop (Fig. 5a); these oscillations persist for over 25 ms as opposed to  $\sim 1.25$  ms for the baseline (undraped) Cu nanorods surface.

(a)



(b)

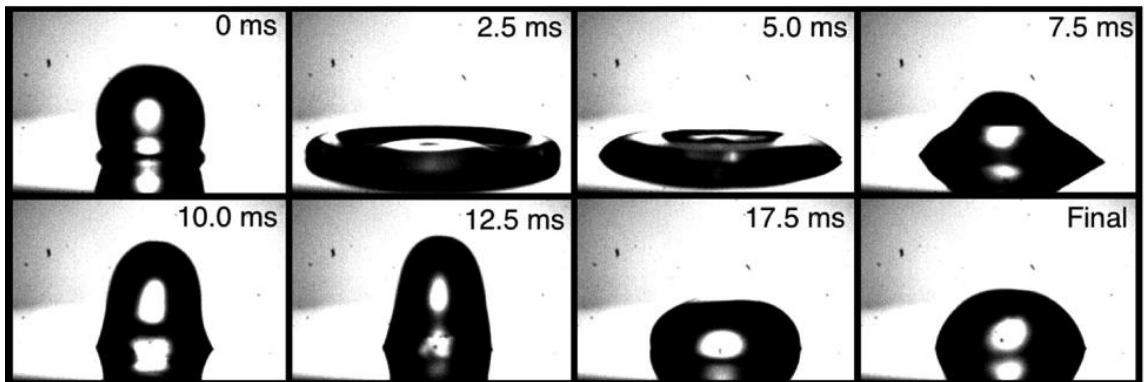


**Figure 4 – Droplet impact experiments. (a) Snapshots of a water droplet impacting the baseline Cu nanorods surface at a velocity of  $\sim 60$  cm/sec. The droplet spreads into a pancake shape as its kinetic energy is converted into elastic strain energy in the drop, however during the receding phase, the water contact line gets strongly pinned to the substrate, which results in large contact angle hysteresis. (b) Corresponding real-time snapshots of a similar sized water droplet striking the surface of the graphene draped Cu nanorods surface at a velocity of  $\sim 60$  cm/sec. In this case the droplet contact line does not get pinned to the surface and extends/contacts periodically as the droplet repeatedly advances and then recedes on the graphene draped surface.**

The droplet impact phenomenon was studied in further detail by plotting the dynamic contact angle against time as shown in Figure 5b. For the baseline Cu nanorods surface the dynamic contact angle decreases rapidly from  $\sim 120^\circ$  during the short-lived advancing phase to 0 degrees during the retraction of the drop. Subsequently the dynamic contact angle fluctuates as the pinned drop pulsates on the surface and settles to a value of  $\sim 40^\circ$ . When the surface is draped with graphene, the initial dynamic contact angle is again  $\sim 120^\circ$ , but this time the water contact angle never drops below  $\sim 60^\circ$  even during the retraction phase and continues to oscillate for a prolonged time period as the droplet vibrates freely (no pinning) on the graphene draped surface. We fitted the results for the dynamic contact angle shown in Figure 5b to an exponentially decaying sinusoidal function expressed as:  $e^{-\zeta\omega t} A \sin(\omega t)$ , where  $\zeta$  is the damping ratio which quantifies the energy dissipation,  $\omega$  is the oscillation frequency,  $t$  is time and  $A$  is the initial amplitude of the contact angle fluctuation. The measured damping ratio ( $\zeta$ ) of the bare Cu nanorods surface was  $\sim 0.164$  which reduces to  $\sim 0.034$  when a monolayer graphene drape is placed over the surface. This indicates that the energy dissipation is  $\sim 382\%$  greater when the water droplet is impacted on the baseline Cu nanorods surface as compared to the corresponding graphene draped surface. Note that the decay in the oscillation amplitude of the dynamic contact angle (as in Figure 5b) reflects the energy dissipated at the interface as well as in the bulk liquid droplet. To focus more narrowly on the liquid-solid interface, we investigated the damping ratio measured with respect to the oscillations in the non-dimensional contact length. From the time traces in Fig. 5a, we conclude that the Cu nanorods surface is over-damped ( $\zeta \geq 1$ , since no oscillations were observed), while the graphene draped surface gave a damping ratio ( $\zeta$ ) of  $\sim 0.072$ . Therefore for the liquid-solid interface, the graphene draped surface exhibits over an order of magnitude less frictional energy dissipation as compared to the baseline Cu nanorods surface.

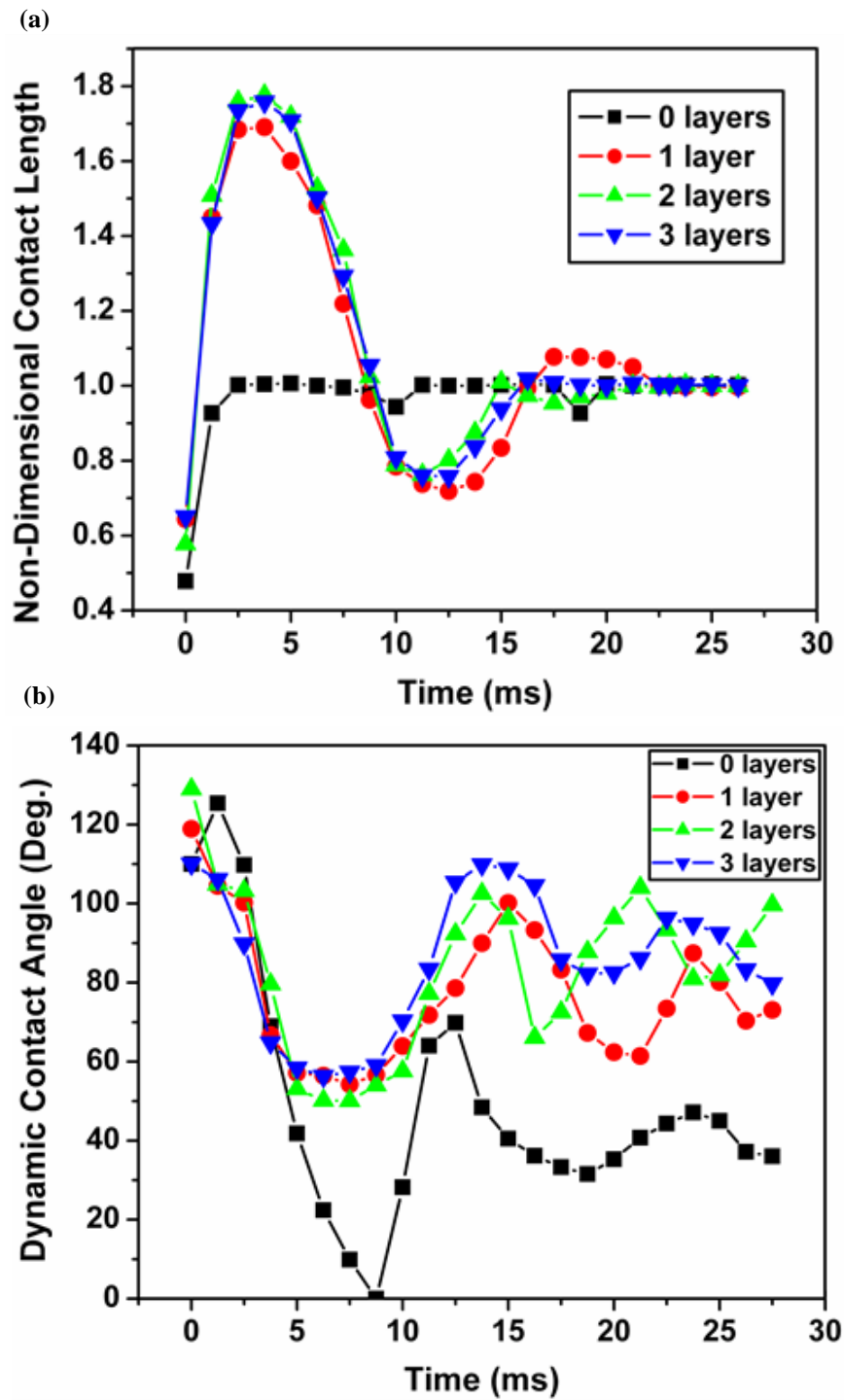
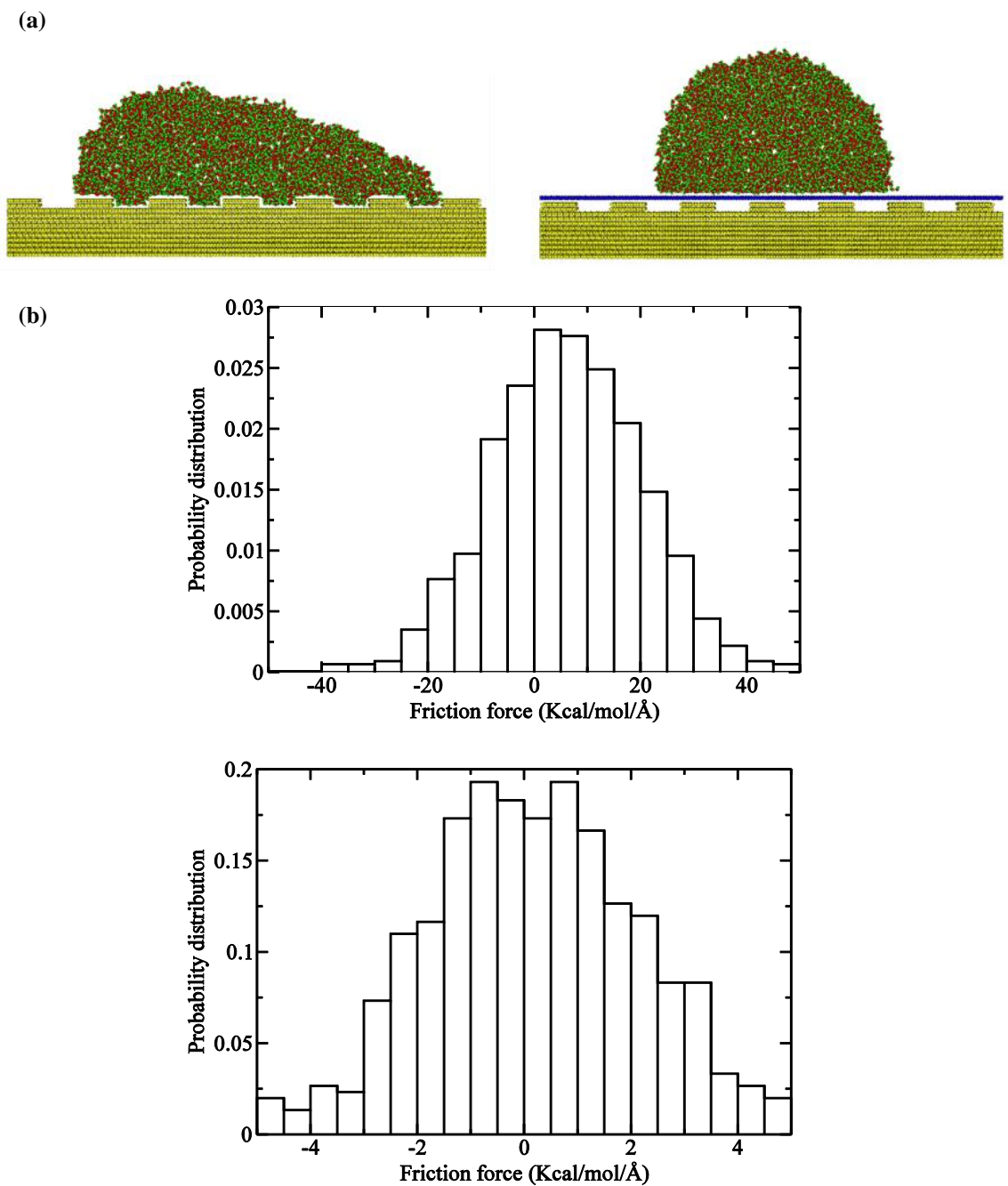


Figure 5 – Non-dimensional drop contact length and dynamic contact angle during droplet impact. (a) Non-dimensional contact length (defined as the real-time contact length at the drop/substrate interface normalized by the final equilibrium contact length) plotted vs. time after impact. (b) Dynamic water contact angle (obtained by averaging the instantaneous, real-time contact angles on the left and right contact lines of the droplet) plotted vs. the time after impact.

### 2.2.5 Molecular Dynamics Simulations

In order to better understand and interpret the experimental observations, we conducted molecular dynamics (MD) simulations to compute both the advancing and receding contact angles for a water droplet on a model nanotextured substrate with and without graphene draping. As a full MD simulation with the actual Cu nanorod dimensions ( $\sim 200$  nm in height and  $\sim 50$  nm in diameter) is beyond the current computational capability, we chose a rough Cu surface (with steps that are 1.5 nm long, 0.6 nm high, repeating with a periodicity of 3.0 nm) as the model nanotextured substrate. We setup the system in the following way. The size of the simulation box is  $307.68 \times 22.20 \times 200$  Å<sup>3</sup>. This simulation box is designed to be thin-slab-like in the y-direction in order to avoid size-dependent contact angle due to line tension. Three-layered thick square-wave-shaped features are constructed on top of the 9-layered Cu (111) slab. The graphene draping is placed at 2.8 Å away on top of the Cu substrate. The substrate (Cu and graphene) is kept rigid throughout the simulation. It has been shown that the water contact angle is almost identical on either rigid or flexible substrates<sup>28</sup>. 4000 water molecules were initially packed orderly on top of the substrate and then relaxed under constant temperature to form the droplet. We used the SPC/E model<sup>29</sup> with slight modification for water-water interactions, which consists of Coulombic interactions between partial charges on O (-0.8476e) and H (+0.4238e) atoms, and an O-O Lennard-Jones (LJ) interaction with  $\epsilon_{\text{O-O}} = 0.6502$  kJ/mol,  $\sigma_{\text{O-O}} = 3.166$  Å and a cutoff of 10 Å. Harmonic bond and angle constraints are used to keep the O-H distance close to 1 Å and the H-O-H angle close to 109.47. LJ potentials are used for both C-O and Cu-O interactions. The LJ parameters are determined as  $\epsilon_{\text{C-O}} = 0.3975$  kJ/mol,  $\sigma_{\text{C-O}} = 3.19$  Å,  $\epsilon_{\text{Cu-O}} = 0.7113$  kJ/mol and  $\sigma_{\text{Cu-O}} = 3.19$  Å to match the experimental contact angles for water/graphite and water/Cu.

The system was equilibrated at 298 K for 2.4 ns to reach equilibrium under NVT ensemble with an integration step of 1 fs. The substrate is dragged towards the positive x direction with a constant velocity of 10 m/s. At the same time, the x-position of center of mass (COM) of the water droplet is held fixed. Moreover, the velocity of COM along the x direction is held at zero.



**Figure 6 – Molecular dynamics (MD) simulations. (a) A snapshot of a moving water droplet (the substrate is moving to the right) on a rough nano-textured Cu surface without a graphene drape (upper graph) and with a monolayer graphene drape (lower graph) during our molecular dynamics simulations. The porosity of the surface (projected area of the solid-liquid contacts divided by the total projected area of the droplet) is  $\sim 0.5$  which is similar to the experiments. (b) The friction force distribution for water droplet on bare patterned copper (upper graph) and graphene-coated patterned copper (lower graph).**

This simulation setup leads to a moving water droplet sliding on a substrate such that both the advancing and receding angles can be measured in the same molecular simulation. After the droplet reaches the steady shape, we acquire data using the next 2.4 ns while the temperature is maintained at 298 K. We generated the equimolar contour of the droplet based on its time-averaged shape. The advancing and receding angles are then obtained by fitting the partial contours 10~20 Å away from the substrate.

As shown in Figure 6a, the shape of the moving water droplet (the substrate is moving to the right) on the roughened Cu surface is significantly altered by the monolayer graphene drape. The simulations indicate that the moving water droplet fully wets the undraped (rough) Cu surface reaching the Wenzel state, which is consistent with experimental observations. However, once it is draped by single-layer graphene, there is no indication of water penetrating into the surface. For the undraped (rough) Cu surface, the advancing angle ( $84^\circ$ ) is very different from the receding angle ( $39^\circ$ ). However, for Cu with graphene-draping, the advancing and receding angles are both close to  $\sim 103^\circ$ . Note that the MD simulations assume a perfectly flat (smooth) and defect-free graphene surface which leads to almost zero hysteresis. In the experiments, the hysteresis is larger because the graphene sheet is wrinkled (due to the transfer) and rough since it conforms to the topology of the sharp Cu nanorod tips. Wetting hysteresis can be correlated to the frictional force between the water droplet and the substrate. As shown in Figure 6b, the friction force (from the simulations) for water on the bare (i.e. roughened) Cu surface is  $\sim 5$  Kcal/mol/Å, while the friction force on the same surface after it has been draped by graphene is almost negligible. This observation agrees very well with our drop impact experiments (see Fig. 5) which indicated that the energy dissipation in the nano-textured rough surface (high friction) is up to an order of magnitude higher as compared to the corresponding graphene-draped surface (low friction).

### 2.2.6 Materials and Methods

**Copper Nanorod Deposition:** Copper nanorods were deposited using DC magnetron sputtering with an oblique angle flux incidence of  $\sim 85^\circ$  with respect to the surface normal. The copper target was obtained from Plasmaterials, Inc. with a purity of 99.999%. In order to deposit vertically aligned copper nanorods, the substrate was

mounted on a stepper motor and rotated at a speed of 30 rpm. Vertically aligned nanorods however show a significant fanning out of the structures which drastically reduces the porosity of the film. To reduce fanning out, the substrate rotation direction was changed periodically from clockwise to counter-clockwise and vice versa. Depositions were carried out at room temperature. A pre-sputtering stage in which the substrate was shielded from the flux by a manually controlled shutter was employed to remove possible contaminants from the copper target prior to the final deposition step. The deposition parameters used were: chamber base pressure of  $\sim 8 \times 10^{-7}$  Torr, power of 200 W, an ultra-pure Ar working pressure of  $\sim 2.5$  mTorr and Ar flow rate of 2.01 sccm.

***Graphene Synthesis:*** Single layer graphene was grown using chemical vapor deposition on  $\sim 25$   $\mu\text{m}$  thick copper foils<sup>21</sup>; the growth procedure used was an optimized version developed for our specific furnace. An alumina boat was loaded with a 2 cm x 2 cm copper foil which was placed in a 3 zone split tube furnace and pumped down to 2 mTorr and then purged with argon twice. Hydrogen was set to a flow rate of 8 sccm which corresponds to a pressure of 120 mTorr. The furnace was then ramped to 1020 °C in 30 minutes and the copper foils were then annealed at this temperature for 30 minutes. The graphene growth was initiated by turning on the methane (flow rate = 120 sccm) and this drove the pressure up to 1.2 Torr. After 20 minutes of graphene growth the furnace heaters were turned off and the lid was opened to cool the tube rapidly without turning off the flow of gases. After the tube cooled to  $\sim 400$  °C the flowing hydrogen and methane was replaced by argon to purge the system till the sample temperature was reduced to the ambient.

***Graphene Transfer onto the Cu Nanorods:*** PMMA (dissolved in chlorobenzene @ 50 mg/mL) was spin coated onto one side of the copper foil with graphene. The other side was etched with oxygen plasma to remove the graphene. The copper foil/graphene/PMMA stack was gently placed with the exposed copper side floating onto a solution of 0.25M ammonium persulfate (APS) to etch the copper. After 12 hours the graphene/PMMA stack was transferred to a fresh bath of 0.5M ammonium persulfate (APS) to ensure that the copper was completely etched. This graphene/PMMA stack was

transferred to DI water and washed gently by transferring it repeatedly into pure DI water baths. The graphene/PMMA stack was finally transferred onto the Cu nanorod surface gently to ensure no tearing of the graphene/PMMA stack and was dried in air; this allows the water to slowly evaporate without rupturing the graphene/PMMA stack. Next the Cu nanorod with graphene/PMMA was heated in an oven gradually to  $\sim 100$  °C for 15 minutes to allow the PMMA to partially flow; this in turn enables the graphene sheet to attach itself to the Cu nanorods surface. This step proved to be critical as rapid heating damaged the graphene/PMMA stack while heating above 100 °C fused the Cu nanorods and completely modified the original surface. The Cu nanorod sample with graphene/PMMA was then gently dipped into acetone at 50 °C for 15 minutes to strip away the PMMA layer followed by dipping in ethanol to rinse any residue. The final step was air drying of the Cu nanorods surface draped with graphene.

***Raman Spectroscopy:*** The Raman spectrum for the sample was measured using a Renishaw Raman Scope 2000 which was equipped with 514 nm green laser and a 50x microscope objective lens. CVD grown graphene, from the same batch used for the ‘graphene drape’, was transferred onto a silicon wafer with a 285 nm thick SiO<sub>2</sub> layer to allow easy location and measurement of the Raman signal.

***Contact Angle Measurements:*** Static contact angle measurements as well as advancing and receding contact angle measurements were performed on a 500-F4 Ramé Hart goniometer. Images captured on the goniometer were analyzed using Low-Bond Axisymmetric Drop Shape Analysis (LB-ADSA) plugin on ImageJ software. For the droplet impact study, images were captured using a high-speed PhantomV4 camera at 800 frames per second with an exposure time of 80  $\mu$ s. Extremely low contact angles during the pancake phase had to be measured manually since the LB-ADSA plugin did not work at those values. An average value of the left and right side contact angles was taken in those cases.

## 2.3 Conformal Coating of Graphene on Rough Surfaces

### 2.3.1 Introduction

The previous subchapters helped develop an understanding with respect to the wettability of graphene on flat and rough surfaces. Flat surfaces were found to be wetting transparent under certain conditions. To investigate the effect of roughness, graphene films were draped over copper nanorods. This resulted in reduced surface friction that is experienced by water droplets moving over the substrate. Since such coatings are non-conformal, the air gaps between the porous nanorods are sealed off by a flat graphene sheet resting on top of the copper nanorods. Thus the porosity of such a nanorod surface does not adversely affect the movement of water, since a Cassie to Wenzel state transition is prevented by the presence of an ultra-sheer graphene layer. The transparency of graphene in such a case was limited however. The maximum water contact angle in such a case is ultimately dictated by the graphene sheet ( $\sim 100^\circ$ ), considering the water molecules will be attracted to the basal plane of carbon, even if the underlying substrate is significantly more hydrophobic. These experiments helped gain an understanding with respect to how graphene coatings affect the wetting properties for a surface with nanoscale roughness features. It must be noted, that these coatings did not conformally follow the nanofeatures of the surface.

A study at the Graphene Research Center in KAIST<sup>18</sup>, in collaboration with our group, further developed this concept to produce a corrosion resistant water harvesting surface. The key innovation in this study was the “in-situ” growth of graphene which allows for a very conformal coating of the microscale and nanoscale roughness features. Copper oxide was electroplated in order to create a hierarchical roughness pattern. Copper provides the ideal substrate since it can be used as a catalyst for the CVD growth of graphene using methane and hydrogen, as discussed later in Materials and Methods. The electroplated copper oxide was reduced at a high temperature to form a roughened copper surface, that was found to be hydrophobic (WCA  $\sim 128^\circ$ ) The work focused on using graphene’s unique transparency effect in combination with this roughened underlying copper substrate to create a better surface for water harvesting. A conformal graphene coating helps protect the copper surface from corrosion during use and could potentially improve the performance and lifetime of water harvesting systems built using

this technology. The highly conformal nature of CVD grown graphene on the hierarchically rough microstructures and nanostructures allows the final surface to still exhibit several entrapped air pockets at these hierarchical scales. The sheer graphene coating protects the underlying copper substrate from corrosion and oxidation during usage. The improved chemical stability in addition to the extreme water repellency is a major advantage for any device with such wet operating conditions.

### 2.3.2 Conformal Graphene Coatings via “In-Situ” Deposition

A hydrophobic copper surface may be created by roughening it up and generating entrapped air pockets. Figure 7 shows a schematic that details steps involved in the fabrication process.

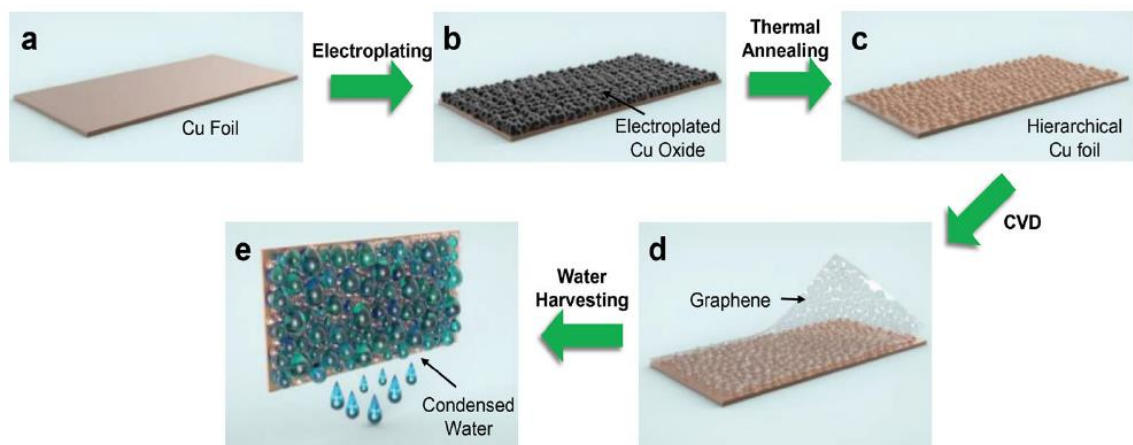


**Figure 7 – Monolayer graphene coating on hydrophobic electroplated copper substrate. (a) Flat Copper substrate. (b) Copper oxide grown on surface to create hierarchical roughness features. (c) Rough copper surface obtained after thermal annealing. (d) In-situ Chemical Vapor Deposition (CVD) used to grow monolayer graphene that provides a conformal coating for the hierarchical roughness features. (e) Water harvesting using the graphene protected, corrosion resistant hydrophobic copper surface. The graphene is wetting transparent and thus does not disturb the intrinsic hydrophobicity of the roughened underlying copper substrate**

Reprinted by permission: “Kim, G. T., Gim, S. J., Cho, S. M., Koratkar, N., & Oh, I. K. Wetting-Transparent Graphene Films for Hydrophobic Water-Harvesting Surfaces. *Adv. Mater.* 26, 5166-5172 (2014)”, Copyright © 2014 WILEY-VCH Verlag GmbH & Co. KGaA, Weinheim<sup>18</sup>

Copper oxide is electroplated in order to create desired surface roughness features. An aqueous solution of ~0.06 M sulfuric acid (H<sub>2</sub>SO<sub>4</sub>) and ~0.08 M copper sulfate (CuSO<sub>4</sub>) is used at ambient temperature for this electroplating process. Copper oxide particles are deposited on the surface and end up generating a pattern with hierarchical

roughness features. Following this, a thermal annealing step at  $\sim 850^{\circ}\text{C}$  is carried out. This step ensures that copper oxide particles are reduced to copper and that all the impurities are removed. Once the reduction is complete, graphene films are synthesized on this roughened copper surface using *in-situ* chemical vapor deposition. Methane and hydrogen are used as the hydrocarbon source for graphene growth at  $\sim 1000^{\circ}\text{C}$ , while hierarchically rough copper structures act as the catalyzing surface<sup>19</sup>. Once the surface is covered with a layer of graphene, it is used in experiments to demonstrate the improvement in performance and corrosion resistance for a water harvesting application.

Figure 8 a, b, c and d are images taken using a scanning electron microscope (SEM) in order to understand the morphology and structure of the copper surfaces involved in this study. The authors designated baseline copper as Cu, electroplated copper as h-Cu, electroplated and thermally annealed copper as h-rCu, and electroplated and thermally annealed copper with graphene as h-Gr/rCu. This nomenclature is used to identify the different copper surfaces. As seen in Figure 8b, the morphology for the electroplated copper oxide surface (h-Cu) is very different from the baseline copper foil (Figure 8a). The surface exhibits a lot more roughness features that are hierarchical in nature. After the electroplating process, thermal annealing (Figure 8c) and CVD growth of graphene (Figure 8d) also introduce changes to the surface morphology. These processes are carried out at  $850^{\circ}\text{C}$  and  $1000^{\circ}\text{C}$  respectively. At such high temperatures the copper particles tend to melt and vaporize. Consequently, the quantity of copper was reduced significantly after these heating steps. In spite of the loss of mass, as well as some agglomeration of the copper particles with each other due to melting, both the h-rCu and h-Gr/rCu surfaces (Figure 8c and 8d) are dramatically rougher than the baseline copper foil (Figure 8a). Raman spectroscopy characterization helped confirm the presence of graphene on these surfaces following the CVD growth process. As a control, graphene was also grown on the baseline copper foil. The Raman spectra (shown in Figure 8e) for these graphene layers after transfer on to Si/SiO<sub>2</sub> substrate shows very clear G and 2D peaks. Additionally, the defect related D-peak was found to be absent, indicating that the graphene was good quality, continuous, and had very few broken or dangling carbon bonds that might expose the underlying substrate.

### 2.3.3 Experimental Results and Discussion

The contact angle for water was measured using the sessile droplet method, where a small droplet is placed gently on the surface in front of a light source, and a camera takes an image of the silhouette from the other side. The baseline copper surface (Cu) exhibits a contact angle of  $\sim 86^\circ$  as shown in Figure 8a. Once the copper has been electroplated to create some roughness (h-Cu), the contact angle is found to be  $< 19^\circ$  (Figure 8b). This is expected since the electroplating process essentially deposits copper oxide particles that are super-hydrophilic in nature. According to the Wenzel model<sup>12</sup> for rough surfaces (wherein water penetrates the pores and structural features), a substrate that comprises of particles with a high affinity for water will also display super-hydrophilic behavior. To get back to a hydrophobic state, this surface is thermally annealed (h-rCu) and checked for wettability as shown in the inset for Figure 8c. This reduces the electrodeposited copper oxide by removing oxygen and makes the substrate highly hydrophobic ( $\sim 128^\circ$ ) as the water droplet rests on top of the surface topographies in accordance with the Cassie-Baxter model of wetting. The hydrophobic pockets of air stay within the pores of the rough topology since water is unable to effectively wet the hydrophobic copper walls in this architecture. Following thermal annealing, a Chemical Vapor Deposition (CVD) process similar to the one described earlier (2.2.6 Materials and Methods) is used to grow graphene directly on the reduced copper surface. Previously, in 2.2, it was shown that draping roughened copper nanorods with a monolayer of graphene would result in a lower contact angle, a value closer to what is expected for single layer graphene. This wetting opacity is observed when graphene covers up the pores and seals off the air pockets from exposure to water droplets. In sharp contrast, graphene on top of a rough surface in this present study seems to not affect the underlying hydrophobicity of electroplated copper. In fact even though the graphene is much more hydrophilic (WCA  $\sim 100^\circ$  as compared to  $128^\circ$  for electroplated copper) it still maintains wetting transparency.

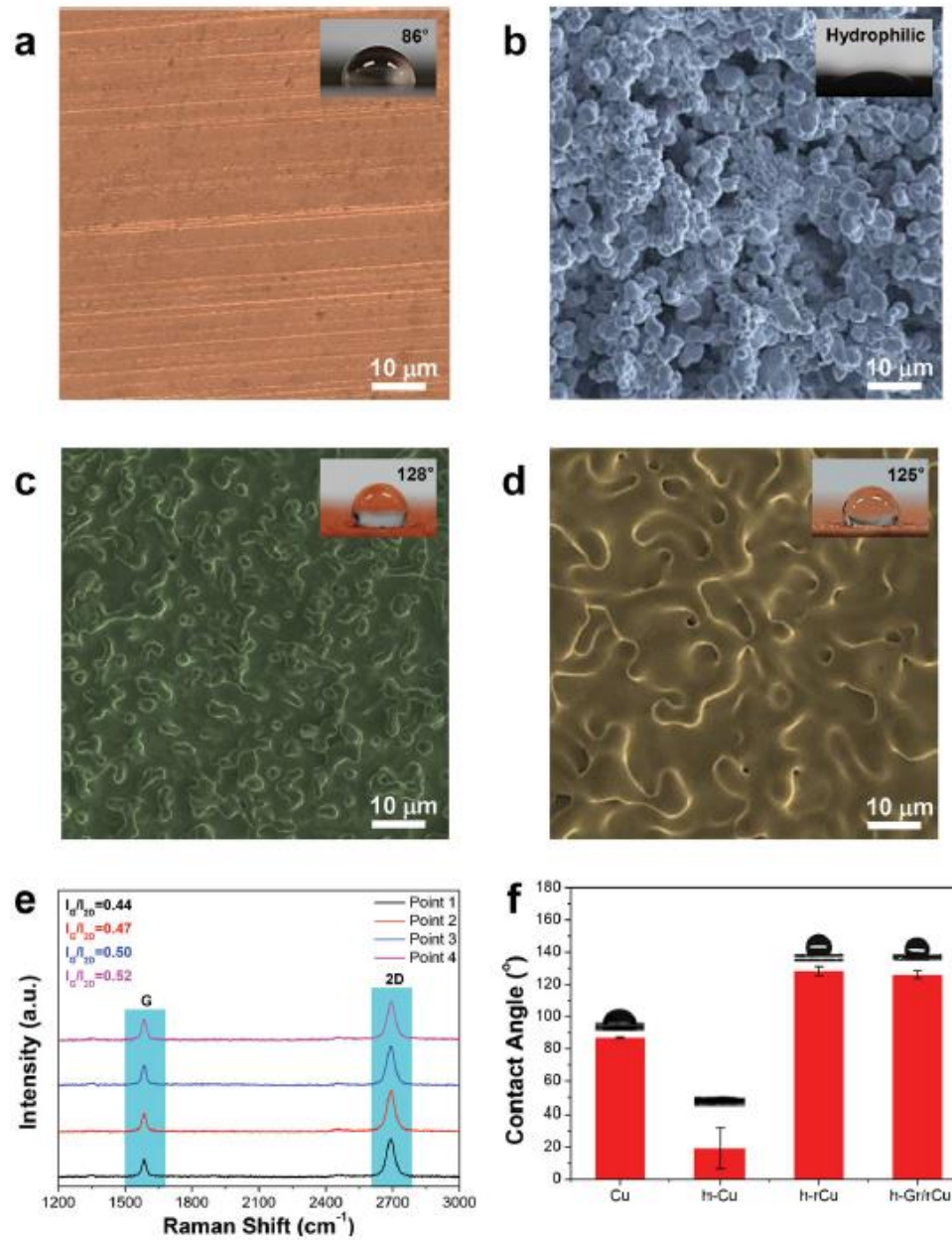


Figure 8 – The wetting transparency and water repellency achieved by conformal coating of graphene on a roughened copper surface Scanning Electron Microscopy (SEM) images for (a) Baseline copper surface (Cu). (b) Electroplated copper oxide surface (h-Cu). (c) Electroplated and thermally annealed copper surface (h-rCu). (d) Electroplated and thermally annealed copper surface after graphene growth using CVD (h-Gr/rCu). (e) Raman Spectra of graphene transferred to SiO<sub>2</sub>. (f) Water contact angle measurements on substrates (a)-(d).<sup>18</sup>

This intriguing aspect may be explained by the different deposition strategies followed in these two cases. In the prior case, graphene is first grown on copper foil and then transferred using wet chemistry methods that employ a polymer (PMMA) layer as a support. PMMA is later removed using hot acetone, and the graphene sheet just sits on top of the copper nanorods. The water droplet therefore sees a relatively flat surface composed of carbon atoms, leading to wetting opacity.

In contrast to transferred graphene, in-situ CVD growth involves flowing gases (hydrogen and methane) over the catalyzing roughened copper substrate at low pressure. The gas molecules are able to reach inside all the micro-scale or nano-scale pores as a result, and the dissociation of methane molecules on copper is very well spread. Owing to the low solid solubility of carbon in copper, the mechanism of growth process is dictated by surface adsorption<sup>20-21</sup>. Carbon atoms on the surface bond with each other and a highly conformal graphene monolayer begins to form. This process is also self-limiting with respect to the number of layers and usually stops after a single layer of graphene is covering the entire surface. Considering the dependency of the process on surface adsorption, it is natural to expect that graphene in this case will adhere closely to topological features present on the substrate. CVD growth of graphene thus effectively covers the entire area of exposed copper, while closely following the undulating nature of electroplated copper particles. Due to this, wetting transparency of graphene on copper is maintained at the local level. Furthermore, air pockets formed by the roughness features remain unaffected by the sheer thin monolayer of carbon. This is what allows the substrate to maintain its hydrophobicity ( $\sim 125^\circ$ ) as shown in Figure 8d. This result demonstrates that it is in fact possible to maintain the water repellent characteristics of a textured, porous surface even after they have been coated with a conformal layer of graphene. Such graphene coatings uniquely exhibit wetting transparency for extremely hydrophobic surfaces, with water contact angles greater than  $120^\circ$ .

Graphene drapes of this kind are expected to prevent oxidation and corrosion of the underlying copper surface under aggressive environments. In order to assess the effectiveness of graphene protective coatings, copper samples with and without graphene were heated in a furnace at  $200^\circ\text{C}$  for 4 hours. Figure 9 shows the data obtained from X-Ray Photoelectron Spectroscopy (XPS) of the various copper surfaces prior to and

following the oxidation step. It is clearly seen that bare copper (Cu) and electroplated/thermally annealed bare copper (h-rCu) undergo a dramatic change in color. The surfaces that do have graphene (Gr/Cu and h-Gr/Cu) however, show only a minor change in their color. Gr/Cu (Figure 9b) and h-Gr/rCu (Figure 9d) samples have an XPS spectra with two very sharp and clear Cu peaks. The peaks correspond to  $\text{Cu}2p_{3/2}$  and  $\text{Cu}2p_{1/2}$ <sup>22</sup>. It should be noted that bare copper surfaces such as Cu (Figure 9a) and h-rCu (Figure 9c) show additional strong peaks after oxidation. Notably, these peaks correspond to several oxidation states of Cu including CuO, Cu<sub>2</sub>O and Cu(OH)<sub>2</sub>. This experiment shows how graphene coatings can be a great barrier to prevent the oxidation of copper surfaces.

Following the oxidation in thermal furnace, experiments were conducted in electrolytic environments to analyze the anti-corrosive attributes of graphene barriers. A 0.1 M NaCl aqueous solution was prepared. Six different samples of h-rCu and h-Gr/rCu were immersed in this liquid for 5 hours at ambient room temperature. The water contact angle was measured at every one hour interval. Sodium chloride is the most common chemical found in sea water and was therefore used in this study as well. Photographs of water droplets resting on h-rCu and h-Gr/rCu are shown in Figure 10 a and b, extending over the five hour period of exposure to NaCl solution. Figure 10c shows the static water contact angle (averaged over six samples) measured over this time period. It is seen that within one hour of exposure, the h-rCu sample shows a rapid drop in contact angle all the way to  $\sim 86^\circ$ . In fact within five hours the WCA decreased to  $\sim 35^\circ$ , lower than the contact angle for even bare copper. On the other hand, h-Gr/rCu samples did not become more wettable with exposure time. The contact angle value stayed relatively stable around  $\sim 125^\circ$  and the underlying copper did not get affected over the 5 hour time period. These results shows the efficacy of graphene based barriers for anti-corrosive coatings.

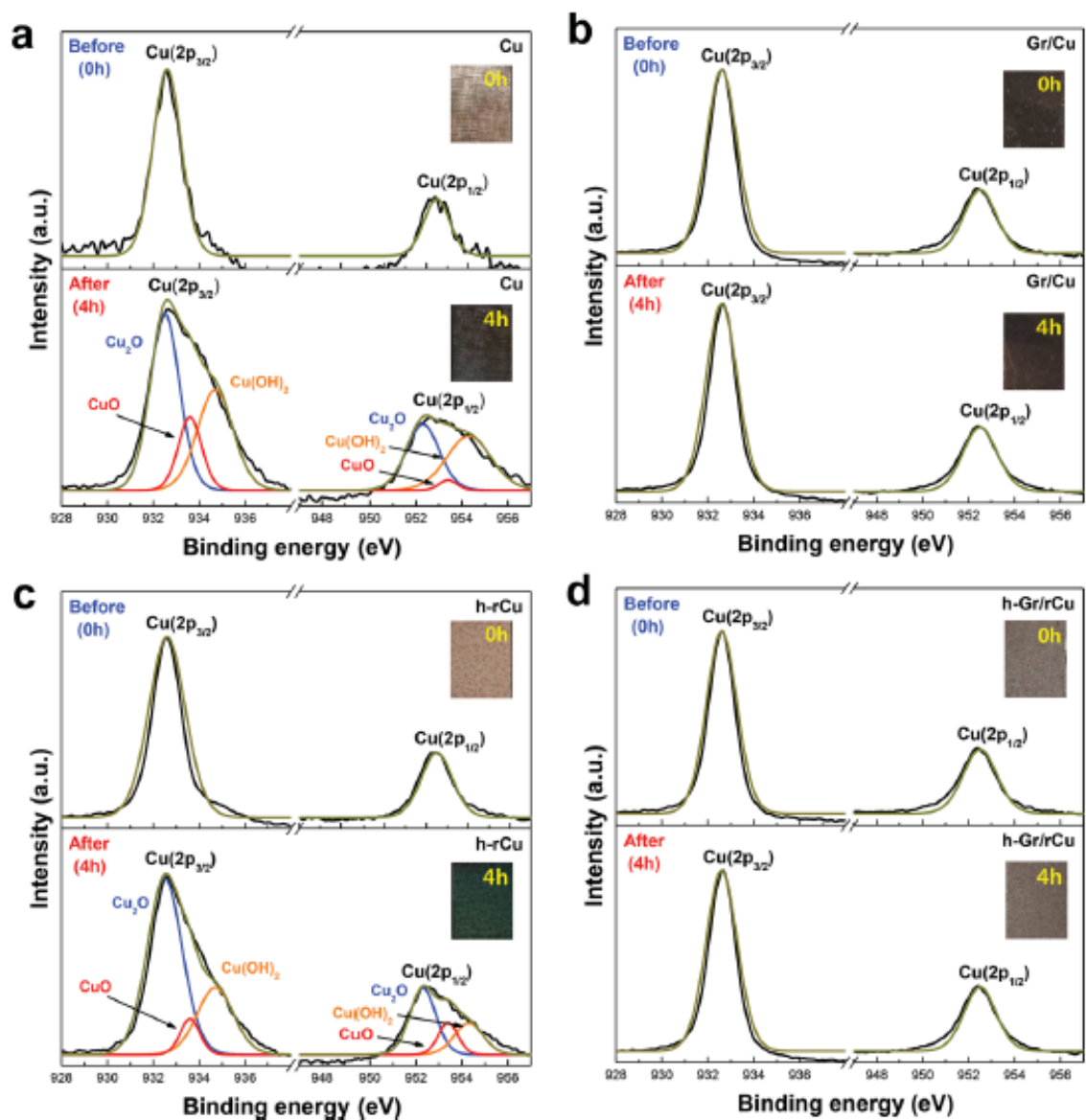


Figure 9 – Improved resistance to oxidation for graphene coated hierarchical copper surface. X-Ray Photoelectron Spectroscopy analysis for Cu2P<sub>3/2</sub> and Cu2p<sub>1/2</sub> spectrum of (a) Flat copper. (b) Graphene coated flat copper. (c) Electroplated and thermally annealed Cu without graphene. (d) Electroplated and thermally annealed Cu with graphene. Upper spectra and inset photographs are taken before the annealing at 200°C for 4 hours in air, while the data and images below are taken afterwards.<sup>18</sup>

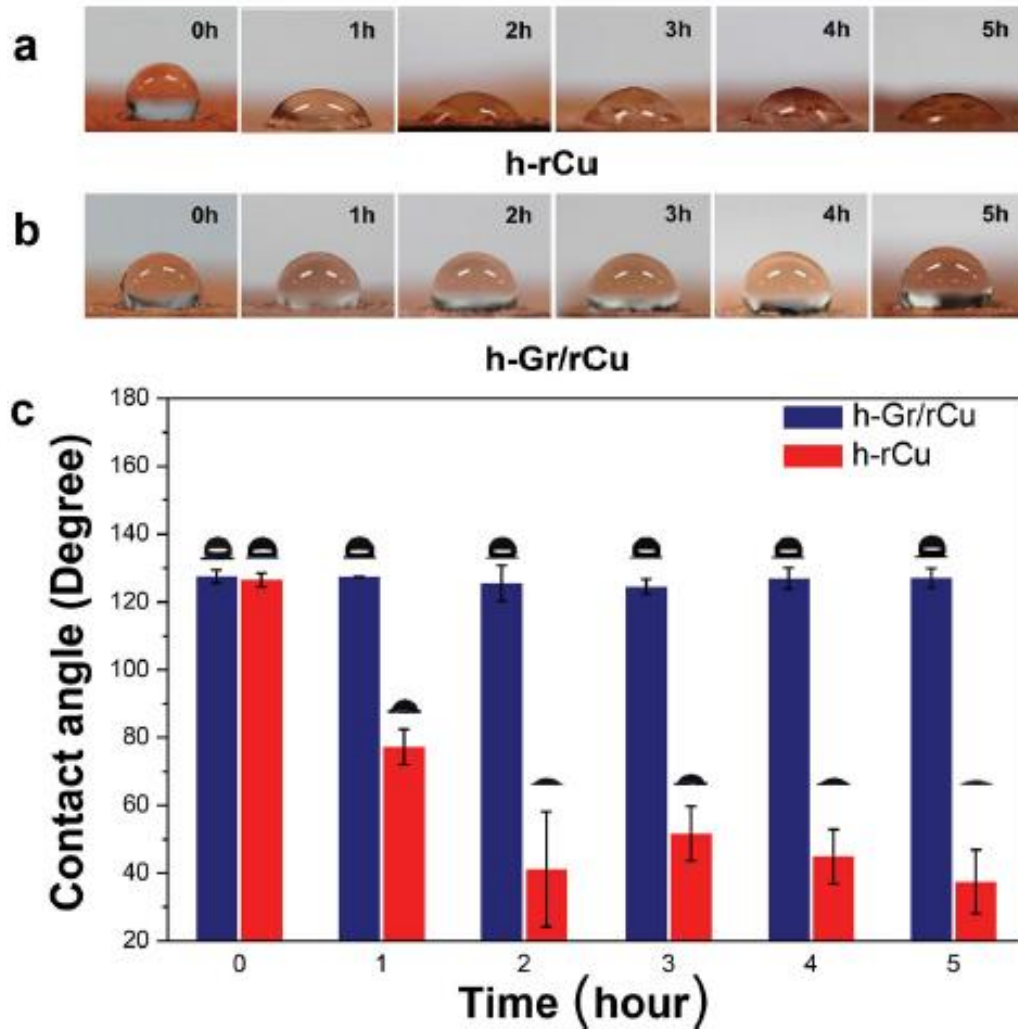
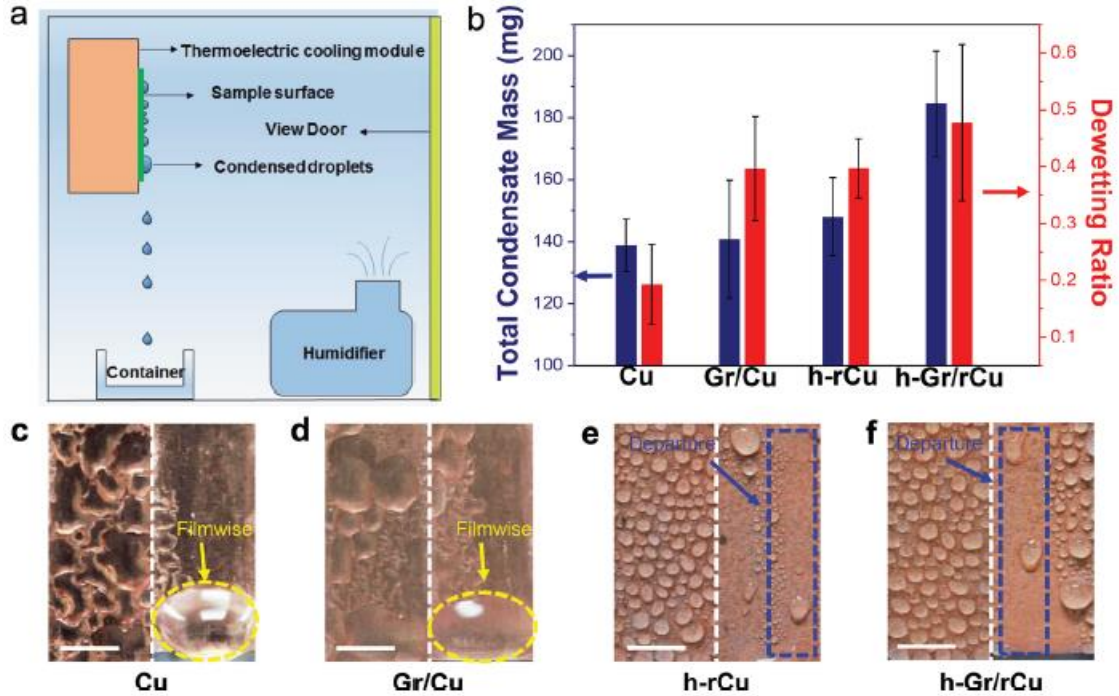


Figure 10 – Graphene monolayer helps improve chemical stability and ensures sustained hydrophobicity in corrosive environments. Photographs of a water droplet were taken on (a) h-rCu and (b) h-Gr/rCu after immersion in a ~0.1 M NaCl aqueous solution over a period of 1-5 hours. (c) Static water contact angle variation from 0 to 5 hours of electrolyte immersion.<sup>18</sup>

The unique hydrophobicity coupled with long term chemical stability proves useful in a multitude of applications including water harvesting through dehumidification. An experiment was conducted to test the utility of h-Gr/rCu surfaces for water harvesting by performing dehumidification using all the samples created (Cu, Gr/Cu, h-rCu, and h-Gr/rCu). The condensation experimental set-up designed for this study can be seen in Figure 11a. The temperature was reduced below ambient temperature by using a thermoelectric cooling module. Simultaneously, relative humidity of the chamber was maintained constant using a humidifier and temperature controller. Reproducibility of the results was confirmed by testing four samples each for Cu; Gr/Cu; h-rCu and h-Gr/rCu. The sample size was kept consistent at 1 cm × 3 cm. Experimental conditions within the environmental chamber were measured using a thermo-hygrometer mounted inside. Temperature was maintained at  $\sim 30.0^{\circ}\text{C} \pm 1$  while relative humidity was kept in the  $\sim 80\text{-}85\%$  range. Substrates were cooled down to a temperature of  $\sim 7.0^{\circ}\text{C} \pm 1$ , measured using a thermocouple in contact with the thermoelectric cooling device. The cooled substrates caused droplets to condense and roll off under the effect of gravity into containers kept below them. The total mass of condensed water and the mass collected in these containers was further used to calculate the dewetting ratio. Figure 11b details this information over a period of one hour. The graphene coated h-Gr/rCu surface clearly outperforms baseline Cu, Gr/Cu, and even hydrophobic h-rCu surfaces. To gain an understanding of this behavior, a high speed camera is used for imaging droplet condensation as it takes place on the various surfaces being investigated Figure 11c, d, e, and f). Cu and Gr/Cu are not very hydrophobic, as expected, and display a water contact angle  $\sim 86^{\circ}$ . This makes it impossible for the surface to stay within drop-wise condensation regime, as the nucleating droplets quickly coalesce, transitioning the system to a film-wise condensation mode as evidence in Figure 11c and d. A fairly low dewetting ratio of  $\sim 0.3$  (Figure 11b) indicates that most of the condensed water remains on these surfaces as a liquid film, since droplets do not roll or slide off.



**Figure 11 – Dehumidification for water harvesting (a) Droplet condensation experimental set-up. (b) Total condensate mass and dewetting ratio for the Cu, Gr/Cu, h-rCu and h-Gr/rCu surfaces. (c), (d) Filmwise condensation on bare copper (Cu) and copper with graphene coating (Gr/Cu). (e), (f) Drop wise condensation mode observed on electroplated/thermally annealed copper without (h-rCu) and with (h-Gr/rCu) graphene coating.<sup>18</sup>**

On the other hand, both h-rCu and h-Gr/rCu surfaces are much more hydrophobic and exhibit water contact angles above  $125^\circ$ . This leads to dropwise condensation behavior for these interfaces. In such dehumidification experiments, the rate of vapor-to-liquid phase change is governed by the rate of heat transfer. More water may be harvested if heat is transferred rapidly from water vapor to the surface. In this regard, a dropwise condensation regime is much better since there is always exposed surface area that allows for fast and efficient heat transfer to take place. Liquid films resulting from filmwise condensation have been shown to have higher interfacial thermal resistance<sup>23-24</sup>. This explains how the dropwise condensation surfaces, h-rCu and h-Gr/rCu, condense larger quantities of water when compared with filmwise condensation surfaces such as Cu and Gr/Cu. It is also worth noting that among the two dropwise condensation surfaces, h-Gr/rCu performs significantly better than h-rCu with respect to their water harvesting capabilities. This is due to the better chemical stability of graphene coated copper. Graphene’s anti-corrosive properties ensure stable wetting behavior over time,

as shown in Figure 9 and Figure 10. Conversely, the oxidation of bare roughened copper particles (h-rCu) results in increased interfacial thermal resistance, which adversely affects the heat transfer rate and eventually results in lower total condensate mass. The h-Gr/rCu surface has a wetting transparent graphene coating that acts as a thermally conductive passivation layer, suppressing oxidation of copper without affecting the inherent hydrophobicity of the substrate underneath.

## 2.4 Summary

The wetting transparency of graphene is shown to break down when sheets are non-conformally put down upon the tops of roughened nanostructures. The highest contact angle is limited in such cases by the graphene-water interaction. However, in certain cases the transparency effect is found to work even on strongly hydrophobic rough substrates. This requires in-situ growth of graphene through CVD methods. Although the CVD approach is limited to metallic surfaces such as copper and nickel, which limit the maximum achievable water contact angles, engineered nanostructures and microstructures could result in entrapped air pockets, leading to hydrophobic substrates. A conformal graphene coating does not disturb the inherent hydrophobicity of such roughened architectures, and is shown to maintain its wetting transparent nature. The key to this is “in-situ” deposition of the graphene layer using chemical vapor deposition methods, so as to ensure a coating that is well adhered and closely follows the contours of surface roughness features. Such graphene coatings show enhanced anti-corrosion properties and help maintain the wetting stability of underlying surfaces. The chemical stability and improved droplet mobility resulting from a passivating monolayer of carbon is extremely useful for a variety of applications, such as water harvesting that was demonstrated in this study.

## 2.5 References

1. Rafiee, J. *et al.* Wetting transparency of graphene. *Nat. Mater.* **11**, 217-222 (2012).
2. Shih, C. J. *et al.* Breakdown in the wetting transparency of graphene. *Phys. Rev. Lett.* **109**, 176101 (2012).
3. Singh, E. *et al.* Graphene Drape Minimizes the Pinning and Hysteresis of Water Drops on Nanotextured Rough Surfaces. *ACS Nano* **7**, 3512-3521 (2013).
4. Chen, X. *et al.* Nanograssed micropyramidal architectures for continuous drop-wise condensation. *Adv. Funct. Mater.* **21**, 4617-4623 (2011).
5. Blossey, R. Self-cleaning surfaces—virtual realities. *Nat. Mater.* **2**, 301-306 (2003).
6. Wang, Z., Lopez, C., Hirska, A., & Koratkar, N. Impact dynamics and rebound of water droplets on superhydrophobic carbon nanotube arrays. *Appl. Phys. Lett.* **91**, 023105 (2007).
7. Miwa, M., Nakajima, A., Fujishima, A., Hashimoto, K., & Watanabe, T. Effects of the surface roughness on sliding angles of water droplets on superhydrophobic surfaces. *Langmuir* **16**, 5754-5760 (2000).
8. Feng, L. *et al.* Super-hydrophobic surfaces: from natural to artificial. *Adv. Mater.* **14**, 1857-1860 (2002).
9. Yoshimitsu, Z., Nakajima, A., Watanabe, T., & Hashimoto, K. Effects of surface structure on the hydrophobicity and sliding behavior of water droplets. *Langmuir*, **18**, 5818-5822 (2002).
10. Lafuma, A., & Quéré, D. Superhydrophobic states. *Nat. Mater.* **2**, 457-460 (2003).
11. Cassie, A. B. D., & Baxter, S. Wettability of porous surfaces. *T. Faraday Soc.* **40**, 546-551 (1944).
12. Wenzel, R. N. Resistance of solid surfaces to wetting by water. *Ind. Eng. Chem.* **28**, 988-994 (1936).
13. Krishnan, R., Lu, T. M., & Koratkar, N. Functionally strain-graded nanoscoops for high power Li-ion battery anodes. *Nano Lett.* **11**, 377-384 (2010).
14. Li, C. *et al.* Nanostructured copper interfaces for enhanced boiling. *Small*, **4**, 1084-1088 (2008).
15. Schrader, M. E. Ultrahigh-vacuum techniques in the measurement of contact angles. II. Water on gold. *J. Phys. Chem-US.* **74**, 2313-2317 (1970).
16. Chen, S. *et al.* Oxidation resistance of graphene-coated Cu and Cu/Ni alloy. *ACS Nano*. **5**, 1321-1327 (2011).
17. Bunch, J. S. *et al.* Impermeable atomic membranes from graphene sheets. *Nano Lett.* **8**, 2458-2462 (2008).
18. Kim, G. T., Gim, S. J., Cho, S. M., Koratkar, N., & Oh, I. K. Wetting-Transparent Graphene Films for Hydrophobic Water-Harvesting Surfaces. *Adv. Mater.* **26**, 5166-5172 (2014).

19. Mattevi, C., Kim, H., & Chhowalla, M. A review of chemical vapour deposition of graphene on copper. *J. Mater. Chem.* **21**, 3324-3334 (2011).
20. Bhaviripudi, S., Jia, X., Dresselhaus, M. S., & Kong, J. Role of kinetic factors in chemical vapor deposition synthesis of uniform large area graphene using copper catalyst. *Nano Lett.* **10**, 4128-4133 (2010).
21. Li, X. *et al.* Large-area synthesis of high-quality and uniform graphene films on copper foils. *Science* **324**, 1312-1314 (2009).
22. Guo, Z., Fang, J., Wang, L., & Liu, W. Fabrication of superhydrophobic copper by wet chemical reaction. *Thin Solid Films* **515**, 7190-7194 (2007).
23. Xu, X., & Carey, V. P. Film evaporation from a micro-grooved surface-An approximate heat transfer model and its comparison with experimental data. *J. Thermophys. Heat Tr.* **4**, 512-520 (1990).
24. Graham, C., & Griffith, P. Drop size distributions and heat transfer in dropwise condensation. *Int. J. Heat Mass Tran.* **16**, 337-346 (2007).

### 3. Freestanding Superhydrophobic Graphene Foams

#### 3.1 Introduction

The wettability of a surface can be quantified by measuring the contact angle of a water droplet placed on the surface of the solid. The contact angle is the angle formed by the solid–liquid interface and the liquid–vapor interface, measured from the side of the liquid<sup>1</sup>. A surface is termed as hydrophobic when its contact angle is higher than 90°, otherwise it is hydrophilic. The larger the contact angle the more hydrophobic the surface. Generally, if the contact angle on a solid surface is greater than 150°, the surface is called super-hydrophobic<sup>1-6</sup>. Such super-hydrophobic surfaces are extremely water-repellant and have many applications ranging from self-cleaning and anti-fouling surfaces to low-drag coatings as well as surfaces for water harvesting and efficient dropwise condensation<sup>7-10</sup>.

In nature many surfaces such as the Lotus leaf are endowed with super-hydrophobicity that arises from its unique surface roughness features. Water droplets on the Lotus leaf tend to remain suspended on the top of these roughness features due to entrapped air pockets; this is called the Cassie state<sup>11</sup>. Such suspended Cassie drops display low adhesion to the substrate and can easily roll off the surface and thereby remove contaminants from the surface (self-cleaning). Taking inspiration from nature several studies have exploited surface roughness and surface chemistry (low energy coatings) to engineer superhydrophobic surfaces<sup>12-17</sup>. A variety of microscale (e.g. silicon micro-posts) as well as nanoscale (e.g. carbon nanotube) roughness features have been studied. However so far there has been very limited work on the use of graphene based structures to control surface wettability. Graphene is a single-atom-thick perfectly two-dimensional sheet of sp<sub>2</sub> hybridized carbon atoms<sup>18-19</sup>. The majority of the prior work on wetting of graphene films<sup>20-21</sup> has involved deposition of graphene from a colloidal solution onto substrates via spray or spin coating. The limitation of such methods is that there is poor control over the porosity and structure of the deposited graphene film. Non-uniformity in the porosity or roughness distribution of the surface

---

This chapter previously appeared as: Singh, E. et al. Superhydrophobic graphene foams. *Small*, **9**, 75-80 (2013).

can result in loss of hydrophobicity in practical situations, like droplet impact<sup>22</sup>. Droplet impact is important in lab-on-chip devices, ink jet printing, spray cooling of hot surfaces, solder drop dispensing in microelectronics as well as liquid atomization and cooling applications. On impact, pinning of the droplet can occur due to a transition from the Cassie state, where the droplet rests over the trapped air pockets, to the Wenzel state, where the droplet penetrates into the interstices of the surface and displaces the air<sup>23</sup>. Such a Cassie-to-Wenzel state transition implies that water drops are no longer able to rebound or slide off the surface and remain pinned to the substrate.

A novel macroscopic graphene structure comprised of an integrated foam-like network of graphene sheets with well-controlled microscale porosity and roughness is demonstrated<sup>24</sup>. The walls of the foam are comprised of few-layered graphene sheets coated with Teflon. The foam is produced using template directed chemical vapor deposition which enables a highly consistent and ordered pore structure. We show that such graphene foam architectures display stable super-hydrophobic behavior under both static and well as dynamic (impact) conditions. The advancing water contact angle of the graphene foam surface exceeds  $163^\circ$  while the receding contact angle is about  $143^\circ$ . Droplet impact experiments also reveal that water droplets can very effectively rebound off the graphene foam without pinning to the surface or damaging the foam structure. The graphene foam is also highly flexible and mechanically strong and could conveniently be attached to a variety of solid surfaces to control their wettability and impart super-hydrophobicity to the surface.

### **3.2 Graphene Foam Macrostructure**

The graphene foam (Figure 12) was synthesized via a template directed chemical vapor deposition (CVD) process described in the Experimental Section. Briefly, carbon atoms are deposited on a sacrificial Ni foam template using CH<sub>4</sub> decomposition at  $\sim 1000^\circ$  C under ambient pressure. The nickel scaffold is then removed using chemical etching. What remains is a continuous 3D network of graphene formed as a free-standing macroscopic structure with extremely thin interconnected sheets of graphene (Figure 12a, c). Since the graphene film forms over the entire Ni foam scaffold, the individual graphene sheets are interconnected or fused into each other. While there are

grain boundaries in the foam, there are no physical breaks or interfaces in the macroscopic 3D graphene network. This makes the graphene foam mechanically strong and easy to handle and manipulate. The graphene foam is also very porous, flexible and light-weight. The graphene foam used in the present study was fabricated using a CH<sub>4</sub> concentration of 0.7 vol% which shows an extremely low density of ~5 mg/cm<sup>3</sup>, corresponding to a very high porosity of ~99.7%<sup>25</sup>. The thickness of the graphene foam samples was ~0.5 mm.

Raman analysis of the foam (Figure 12b) indicates that the walls of the foam are comprised of monolayer to few-layer graphene sheets. The Raman spectra also show a strongly-suppressed defect-related D band, which confirms the overall high quality<sup>26</sup> of the graphene in the foam. To provide more hydrophobicity the graphene foam was coated with a ~200 nm thick layer of a fluoropolymer (Teflon AF) as described in the Experimental Section. Scanning electron microscopy (SEM) analysis of the Teflon coated foam (Figure 12d) shows that even after Teflon coating, the graphene foam retains its structure and porosity which was inherited from the original Ni foam template used in the CVD growth process. The average pore size for the baseline and Teflon coated graphene foam is ~200 μm.

### 3.3 Theoretical Contact Angle Prediction

Considering the foam as a rough surface with large pores it is unlikely to have a pure Cassie or Wenzel state. A mixed wetting state where the droplet penetrates to some extent into the pores leaving air pockets below it is more probable. The contact angle equation for such a state is given by Marmur<sup>27</sup>.

$$\cos \theta = f(R_f \cos \theta_0 + 1) - 1 \quad (1)$$

Here  $\theta$  is the static water contact angle,  $f$  is the fraction of solid-liquid interface per unit area,  $R_f$  is the roughness factor which is the ratio of true solid surface area to its flat projected area and  $\theta_0$  is the water contact angle for a flat surface of the same material (Teflon as ~104° and carbon as ~86°). Using  $f = 0.32$  and  $R_f = 2.5$  (based on SEM image analysis - Figure 12), the static water contact angle was found to be 129.45° for regular foam and 150.01° for the Teflon coated graphene foam. The Teflon coated foam is therefore expected to exhibit superhydrophobic behavior. Another important question

is whether this superhydrophobicity can be maintained under realistic operating conditions involving droplet impact.

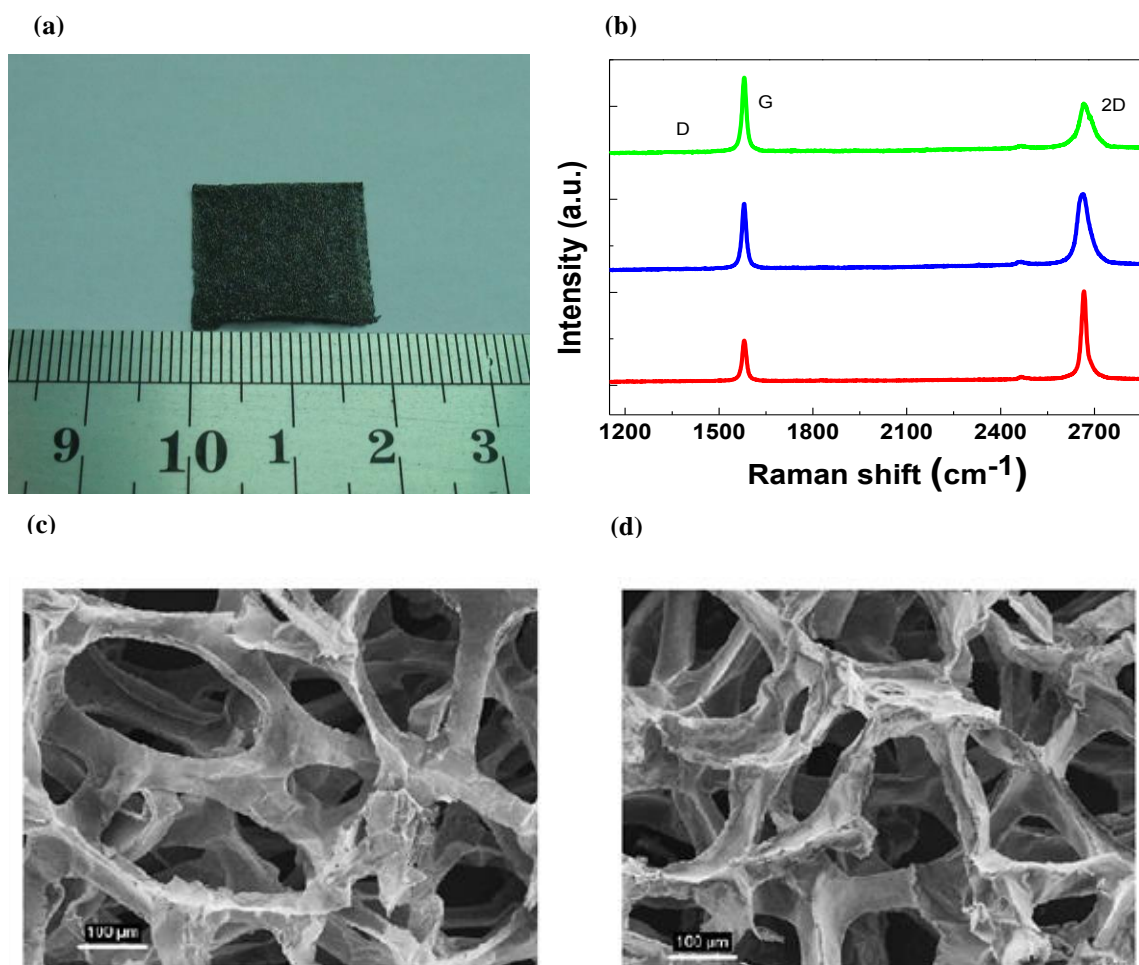


**Figure 12 – (a) Photograph of a macroscopic 3D graphene foam network. The foam is flexible and can be easily handled and manipulated. (b) Raman spectra taken from several locations on the graphene foam clearly showing the Raman G band and 2D band peaks. Based on the ratio of the integrated intensity of the G and 2D bands, we conclude that the walls of the foam are comprised of mono- to few-layered graphene sheets. Note the absence of a defect related D band in the Raman spectrum which indicates the high quality of graphene sheets prepared using our chemical vapor deposition process. (c) Scanning electron microscopy (SEM) image of the micro-porous graphene foam showing average pore size of ~200 μm. (d) Teflon coated graphene foam showing similar pore structure and dimensions to the original graphene foam. The Teflon coating thickness is estimated to be ~200 nm by Teflon coating on to a flat surface which was subsequently cleaved for cross-sectional SEM**

### 3.4 Water Contact Angle Measurements

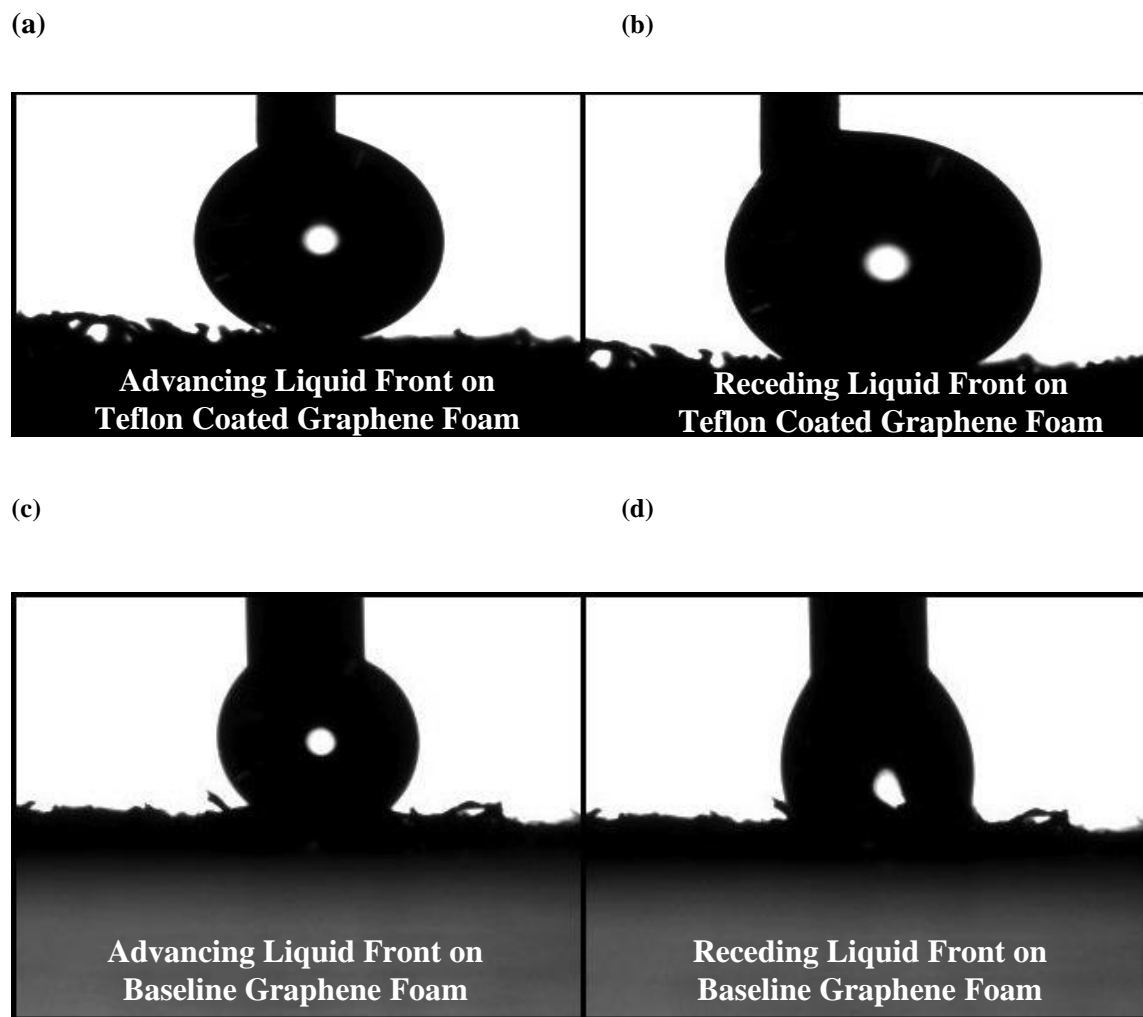


**Figure 13 – (a) Advancing liquid front for the Teflon coated graphene sample indicating an advancing water contact angle of ~163.01 degrees. (b) Receding liquid front on the same sample indicating a receding water contact angle of ~143.78 degrees. (c) Corresponding advancing contact angle on the baseline graphene foam (without Teflon coating) measured to be ~134.86 degrees. (d) Corresponding receding contact angle on the baseline graphene foam measured to be ~110.72 degrees.**

Advancing and receding contact angle measurements were performed using a 500-F4 Rame-Hart goniometer for images and low-bond axisymmetric drop shape analysis technique was used to determine the water contact angles. For this a  $\sim 1 \mu\text{l}$  volume drop was initially brought in contact with the sample surface and subsequently the volume of the drop was increased and then decreased to advance and retract the liquid front. This was repeated several times to check the reproducibility of the results. Figure 13 shows the advancing and receding conditions created by dispensing and retracting water at a rate of  $\sim 0.40 \mu\text{l/s}$ . The Teflon coated foam gives water contact angle values of  $\sim 163.01^\circ$  and  $\sim 143.78^\circ$  respectively for advancing (Figure 13a) and receding (Figure 13b) fronts. This is in agreement with the predicted static water contact angle ( $\sim 150^\circ$  from equation 1) which should lie between the advancing and receding angle values. In comparison to a regular foam (without Teflon coating), which gives advancing (Figure 13c) and receding (Figure 13d) water contact angles of  $\sim 134.86^\circ$  and  $\sim 110.72^\circ$ , the Teflon coated foam is much more hydrophobic. However both the baseline and Teflon coated graphene foams show significant contact angle hysteresis; this we presume is an artifact of the microscale roughness and the large porosity of the foam surface.

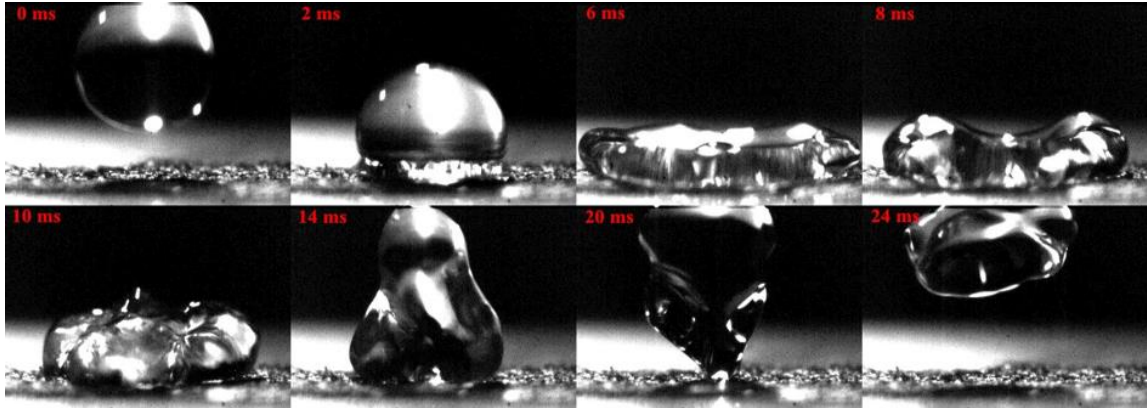
Typically high surface roughness and porosity can cause pinning of the liquid front particularly during the receding of the droplet which consequently increases the difference between the advancing and the receding water contact angles (i.e. the contact angle hysteresis). The Teflon coated graphene foam exhibited a lower contact angle hysteresis of  $\sim 19^\circ$  as compared to  $\sim 25^\circ$  for the baseline foam. Moreover both the advancing and receding contact angles of the Teflon coated graphene foam are nearly  $30^\circ$  higher than the baseline foam and lie in the superhydrophobic range. Therefore the Teflon coated graphene foam with its microscale porosity (entrapped air pockets) and low surface energy offers outstanding water repellency effect.

### 3.5 Droplet Impact Experiments

Droplet impact tests were performed to gauge the ability of the foam to repel impacting water droplets. Droplets as large as 1-1.5 ml were dropped on the regular and Teflon coated graphene foams from a fixed height using a microsyringe to impact the foam at a velocity ranging from 65 cm/sec to 76 cm/sec. The corresponding Weber

number ( $We = \frac{\rho V^2 R}{\gamma}$ , where  $\rho$  is the density of water,  $V$  is the impact velocity,  $R$  is the droplet's radius and  $\gamma$  is the surface tension of water) lies in the 8.3 to 12.7 range. The objective of these tests is to determine whether the kinetic energy of the impacting drop would cause the droplet to penetrate into the pores and transition to a sticky or pinned Wenzel state. A high-speed camera (PhantomV2) operated at ~500 frames per second with 30  $\mu$ s exposure time was used in this study. Time lapse images for the relevant advancing and receding stages of the droplets is shown in Figure 14 at an impact velocity of ~76 cm/sec. For the Teflon coated foam (Figure 14a), the droplet first deforms and flattens into a pancake shape, then retracts and finally rebounds off the surface. The droplet remains completely intact during the collision and does not splinter into smaller drops. The restitution coefficient of the droplets (i.e. ratio of droplet impacting velocity to ejecting velocity) ranges from ~0.3 (for 65 cm/sec impact velocity) to ~0.37 (for 76 cm/sec impact velocity). By contrast on the baseline graphene foam (Figure 14b) the droplet spreads but does not rebound off the surface. It appears to get strongly pinned to the foam surface and pulsates for a prolonged time period until the drop's vibrational energy is dissipated through viscosity.

(a)



(b)

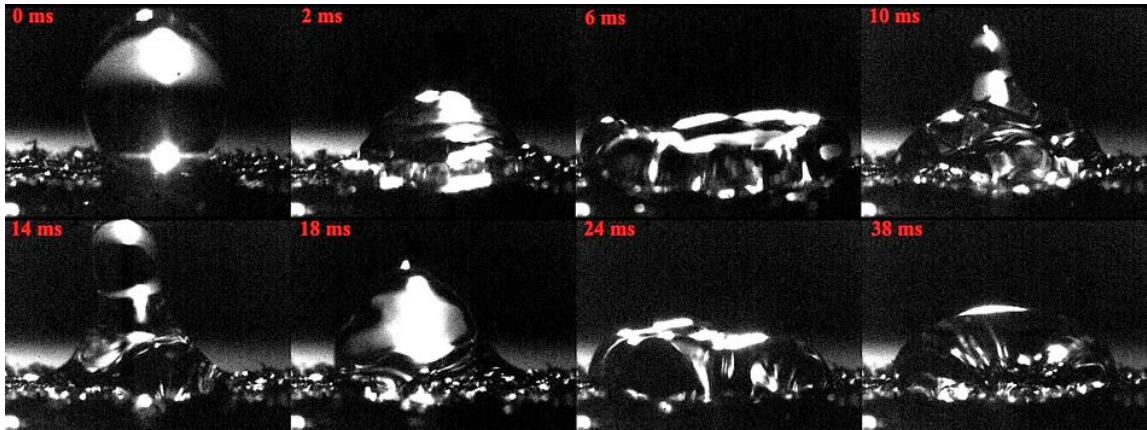
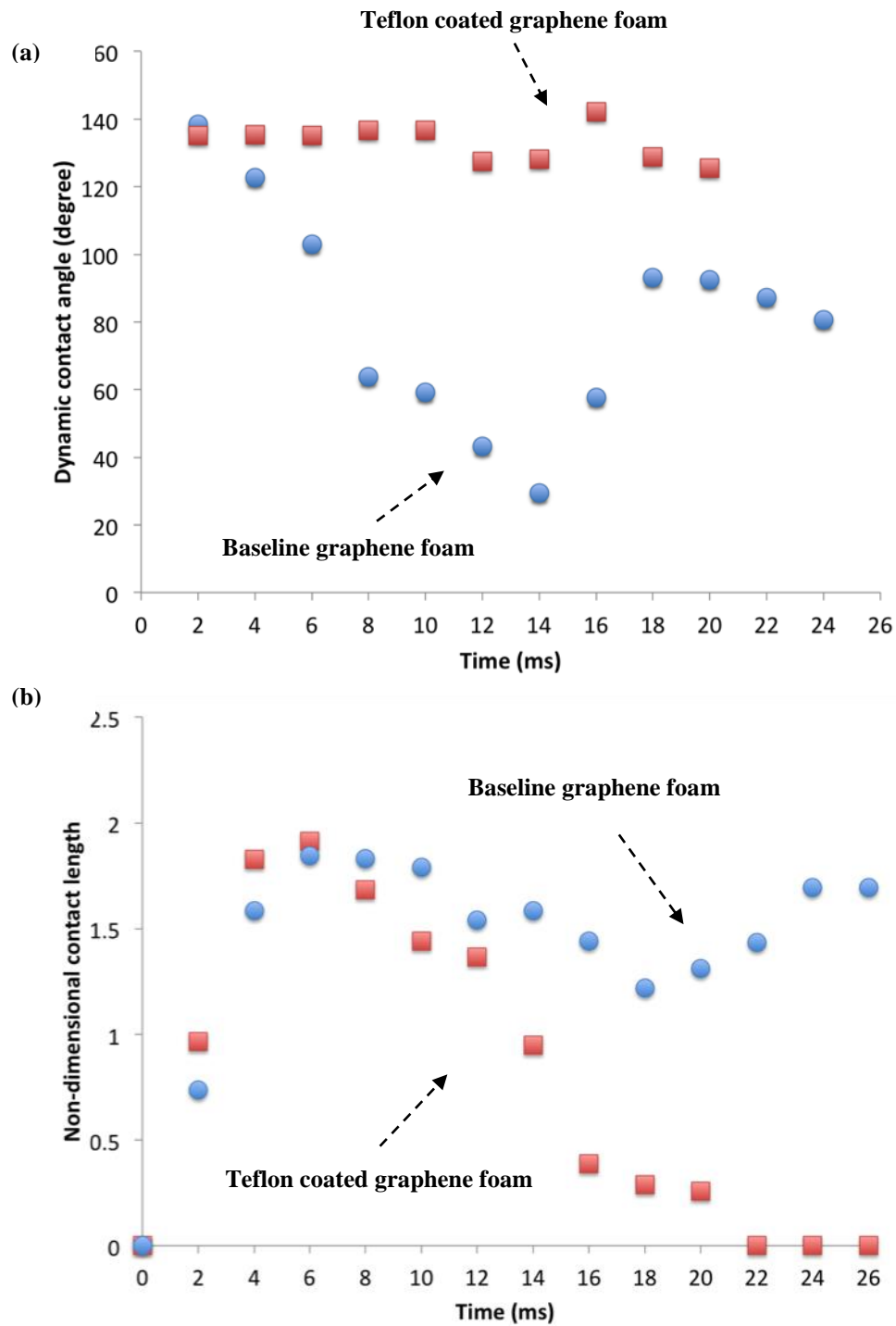


Figure 14 – (a) Snapshots of a water droplet impacting the surface of the Teflon coated graphene foam. The impact velocity just prior to the droplet striking the surface was  $\sim 76$  cm/sec. The sequence of snapshots shows the deformation time history of the droplet upon impact. The droplet spreads, then retracts and successfully rebounds off the surface. The coefficient of restitution (i.e. ratio of droplet impacting velocity to ejecting velocity) is  $\sim 0.37$  for the Teflon coated foam. (b) Corresponding snapshots of a water droplet impacting on the surface of the baseline graphene foam (without Teflon coating). The impact velocity in this case was  $\sim 75$  cm/s. For this case the droplet does not rebound off the surface. The droplet gets pinned to the substrate and pulsates on the surface as its kinetic energy is converted into internal modes of vibration and is eventually dissipated through viscosity.



**Figure 15 – (a) Time history of the droplet’s dynamic contact angle for the droplet impacting on the baseline graphene foam and the Teflon coated graphene foam samples. The impact velocity for both the samples is ~75 cm/s. (b) Normalized contact line length vs. time for droplets impinging on the baseline graphene foam and the Teflon coated foam with a velocity of ~75 cm/s.**

The droplet impact phenomenon was studied in further detail by plotting the dynamic contact angle against time as shown in Figure 15a. The result indicates that the dynamic water contact angle for the Teflon coated foam stays fairly constant during the advancing and receding phases after which the droplet successfully rebounds off the surface. However for the regular foam, the water contact angle is relatively high during the advancing phase but then drops rapidly when the droplet tries to recede. This reduction in the contact angle indicates that the droplet has penetrated into the pores within the graphene foam structure. Such penetration lowers the water contact angle due to greater contact of the droplet with the foam material. If the time axis is extended (not shown here), periodic oscillations in the water contact angle can be seen, which correspond to the vibrations of the droplet as it pulsates on the surface and dissipates its excess energy. Another parameter of interest is the non-dimensional contact length (NDCL) which is the contact length divided by the original drop diameter.

Figure 15b shows the NDCL variation with time for both the regular and Teflon coated foams. For the first  $\sim 4$  ms, the droplet deforms from a spherical to a pancake shape as seen in the images in Figure 14, with the normalized contact length increasing with time during this phase. There is no significant difference in the normalized contact length response of the baseline and Teflon coated foams during the advancing phase. However after  $\sim 4$  ms, the contact length for the droplet on the baseline graphene foam remains fairly constant and does not decrease significantly with time. In contrast, the contact length for the Teflon coated foam decreases monotonically to zero as the droplet contracts and then lifts-off the surface. This result demonstrates that the contact line for the baseline foam becomes pinned to the surface after the advancing (or the spreading) phase of the droplet is complete. Such a pinning phenomenon suggests that the momentum of the droplet during the initial impact enables it to penetrate into the interstices in the foam and transition into the Wenzel state. The resulting increase in contact area between the foam and the droplet significantly increases the adhesion of the droplet to the substrate and prevents the contact line from retracting. The droplet is therefore unable to recover sufficient energy to rebound off the surface and as a consequence gets pinned to the surface and simply vibrates (at  $\sim 50$  Hz frequency) on the foam surface till the energy of the droplet is dissipated. The measured frequency shows good correlation

with the droplet's lowest Rayleigh frequency ( $\sqrt{\frac{2\gamma}{\pi^2 R^3 \rho}}$ ) of ~57.91 Hz. On the other hand, the walls of the Teflon coated foam show much weaker adhesion to water which reduces energy dissipation during the spreading and retraction of the droplet and prevents Cassie-to-Wenzel state transition for the droplet. In order to quantitatively understand this process we computed the critical pressure ( $P_c$ ) required for transitioning the droplet from the Cassie to the Wenzel state [28]:

$$P_c = -\gamma \cos \theta \frac{L}{A} \quad (2)$$

Where  $\gamma$  is the surface tension of water (72 dynes/cm at 25°C), L is the perimeter of the micro-pore (~791.6  $\mu\text{m}$ ) and A is the cross sectional area of the micro-pore (~41088  $\mu\text{m}^2$ ) obtained from SEM images of the graphene foam (Figure 12) and  $\theta$  is the water contact angle of the foam walls (~105° for Teflon). Equation 2 yields a critical pressure of ~340.2 Pa. The impact dynamic pressure ( $P_d$ ) of the droplet can be expressed as [29]:

$$P_d = \frac{1}{2} \rho V^2 \quad (3)$$

Where  $\rho$  is the water density and V is the impact velocity, which in our case was ~76 cm/sec. This gives the dynamic pressure as ~294.3 Pa which is significantly below the predicted critical pressure of ~340.2 Pa. This justifies why the Teflon coated graphene foam does not fully transition into the sticky Wenzel state thereby enabling the water droplet to successfully rebound off the foam surface.

An experiment was also performed where the impact velocity was increased to ~84 cm/sec and the droplet did not rebound off the Teflon coated graphene foam. This is expected since a velocity of 84 cm/sec corresponds to an impact pressure of ~355.8 Pa (from Equation 3) which now exceeds the predicted critical pressure. We have also performed water droplet impact experiments on the Ni foam templates described in Section 2. The Ni foam was coated with ~200 nm thick Teflon coating following the exact same protocols used for Teflon deposition on to the graphene foam. The results for droplet impact at an impact velocity of ~75 cm/sec were also analyzed. In this case the impacting water droplet does not get pinned to the Teflon coated Ni foam surface but it is still unable to rebound off the surface. This inability to rebound of the surface is

indicative of significant dissipation of energy during the spreading and retraction of the droplet. The flexibility of the Teflon coated graphene foam over the far more rigid Teflon coated Ni foam could play a role in its superior ability to rebound water droplets. The cushioning effect provided by the elastic deformation of the graphene sheets and the release of this stored energy back to the droplet could assist with the droplet rebound process. The high flexibility and the resilience of the graphene foam also makes it feasible to coat surfaces with complex shapes and geometries as opposed to the far more rigid Ni foam.

### 3.6 Materials and Methods

**Graphene Foam Synthesis:** To fabricate the graphene foam, a scaffold of porous nickel foam is used as a template for the deposition of graphene. Chemical vapor deposition (CVD) is used to deposit carbon atoms on the nickel foam using  $\text{CH}_4$  decomposition at  $\sim 1000^\circ\text{C}$  under ambient pressure. The nickel scaffold is then removed using chemical etching by a hot HCl (or  $\text{FeCl}_3$ ) solution. To maintain the integrity of the foam during the etching of the Ni and to prevent it from collapsing, a thin layer of poly (methyl methacrylate) (PMMA) is also deposited on the surface of the graphene formed on the nickel foam. In the final step the PMMA layer is dissolved by hot acetone resulting in a free-standing three-dimensional graphene network structure. Additional details regarding this process are provided in Ref. 25.

**Teflon Coating:** Teflon AF 1601S (6% solid in solution) was procured from DuPont and diluted at a 1:24 ratio with the solvent Fluorinert FC-40 bought from 3M (12 ml Teflon AF with 288 ml FC-40). The graphene foam was coated with the resulting solution by drop casting and baked at  $\sim 165^\circ\text{C}$  for 24 hours. This is above the glass transition temperature for the Teflon AF (160 deg C) and gives a smoother, more adherent polymer coating. The baking was done in a tube furnace (Thermolyne 79300, Thermo Fisher Scientific Inc., USA).

### 3.7 Summary

Teflon coated graphene building blocks were used to create a superhydrophobic structure with an ordered pore structure of ~200 micrometers in dimensions. The advancing water contact angle on the foam surface exceeded 163 degrees. In spite of the large size pores, water repellency is maintained under droplet impact conditions. Since the graphene foam inherits the pore structure of the Ni foam template used in the CVD growth process, this method can be used to uniformly tune the pore size and structure of the graphene foam by selecting the appropriate Ni foam template. In contrast to the Teflon coated graphene foam, Teflon coated Ni foams did not provide stable superhydrophobic behavior especially under droplet impact conditions which indicates that the flexibility of the graphene foams could play an important role. The graphene foam can store elastic strain energy as it is deformed by the impacting drop and then deliver it back to the drop which could assist with the rebound process. Such flexible and mechanically robust graphene foams which display a stable superhydrophobic behavior could find a wide range of applications in self-cleaning, anti-fouling technologies and as low-friction coatings for micro-fluidics and lab-on-chip applications.

### 3.8 References

1. Lafuma, A., & Quéré, D. Superhydrophobic states. *Nat. Mater.* **2**, 457-460 (2003).
2. Fürstner, R., Barthlott, W., Neinhuis, C., & Walzel, P. Wetting and self-cleaning properties of artificial superhydrophobic surfaces. *Langmuir*, **21**, 956-961 (2005).
3. Blossey, R. Self-cleaning surfaces—virtual realities. *Nat. Mater.* **2**, 301-306 (2003).
4. Fürstner, R., Barthlott, W., Neinhuis, C., & Walzel, P. Wetting and self-cleaning properties of artificial superhydrophobic surfaces. *Langmuir*, **21**, 956-961 (2005).
5. Cheng, Y. T., & Rodak, D. E. Is the lotus leaf superhydrophobic? *Appl. Phys. Lett.* **86**, 144101 (2005).
6. Feng, X. J., & Jiang, L. Design and creation of superwetting/antiwetting surfaces. *Adv. Mater.* **18**, 3063-3078 (2006).
7. Xiao, W., Huang, Z., & He, Z. Tuning the wettability on  $\text{La}_{0.7}\text{Sr}_{0.3}\text{MnO}_3$  coatings from superhydrophilicity to superhydrophobicity by hierarchical microstructure. *Appl. Phys. Lett.* **89**, 083101-083101 (2006).
8. Lau, K. K., Bico, J., Teo, K. B., Chhowalla, M., Amaratunga, G. A., Milne, W. I., McKinley, G. H. & Gleason, K. K. Superhydrophobic carbon nanotube forests. *Nano Letters*, **3**, 1701-1705 (2003).
9. Koratkar, N., Wei, B. Q., & Ajayan, P. M. Carbon nanotube films for damping applications. *Adv. Mater.* **14**, 997-1000 (2002).
10. Chen, X. *et al.* Nanograssed micropylamidal architectures for continuous drop-wise condensation. *Adv. Funct. Mater.* **21**, 4617-4623 (2011).
11. Cassie, A. B. D., & Baxter, S. Wettability of porous surfaces. *T. Faraday Soc.* **40**, 546-551 (1944).
12. Fang, Y., Sun, G., Cong, Q., Chen, G. H., & Ren, L. Q. Effects of methanol on wettability of the non-smooth surface on butterfly wing. *J. Bionic Eng.* **5**, 127-133 (2008)
13. Byun, D. *et al.* Wetting characteristics of insect wing surfaces. *J. Bionic Eng.* **6**, 63-70 (2009).
14. Yarin, A. L. Drop impact dynamics: splashing, spreading, receding, bouncing. *Annu. Rev. Fluid Mech.* **38**, 159-192 (2006).
15. Koch, K., Bhushan, B., & Barthlott, W. Multifunctional surface structures of plants: an inspiration for biomimetics. *Prog. Mater. Sci.* **54**, 137-178 (2009).
16. Ma, M., & Hill, R. M. Superhydrophobic surfaces. *Curr. Opin. Colloid In.* **11**, 193-202 (2006).
17. Teshima, K., Sugimura, H., Inoue, Y., Takai, O., & Takano, A. Transparent ultra water-repellent poly (ethylene terephthalate) substrates fabricated by oxygen plasma treatment and subsequent hydrophobic coating. *Appl. Surf. Sci.* **244**, 619-622 (2005).
18. Tang, L. *et al.* Preparation, structure, and electrochemical properties of reduced graphene sheet films. *Adv. Funct. Mater.* **19**, 2782-2789 (2009).

19. Yavari, F. *et al.* Tunable bandgap in graphene by the controlled adsorption of water molecules. *Small* **6**, 2535-2538 (2010).
20. Rafiee, J., Rafiee, M. A., Yu, Z. Z., & Koratkar, N. Superhydrophobic to superhydrophilic wetting control in graphene films. *Adv. Mater.* **22**, 2151-2154 (2010).
21. Wang, G. *et al.* Flexible Pillared Graphene-Paper Electrodes for High-Performance Electrochemical Supercapacitors. *Small* **8**, 452-459 (2012).
22. Wang, Z., Lopez, C., Hirs, A., & Koratkar, N. Impact dynamics and rebound of water droplets on superhydrophobic carbon nanotube arrays. *Appl. Phys. Lett.* **91**, 023105 (2007).
23. Wang, Z., Koratkar, N., Ci, L., & Ajayan, P. M. Combined micro-/nanoscale surface roughness for enhanced hydrophobic stability in carbon nanotube arrays. *Appl. Phys. Lett.* **90**, 143117 (2007).
24. Singh, E. *et al.* Superhydrophobic graphene foams. *Small*, **9**, 75-80 (2013).
25. Chen, Z. *et al.* Three-dimensional flexible and conductive interconnected graphene networks grown by chemical vapour deposition. *Nat. Mater.* **10**, 424-428 (2011).
26. Yavari, F., & Koratkar, N. Graphene-based chemical sensors. *J. Phys. Chem. Lett.* **3**, 1746-1753 (2012).
27. Marmur, A. Wetting on hydrophobic rough surfaces: to be heterogeneous or not to be? *Langmuir* **19**, 8343-8348 (2003).
28. Zheng, Q. S., Yu, Y., & Zhao, Z. H. Effects of hydraulic pressure on the stability and transition of wetting modes of superhydrophobic surfaces. *Langmuir* **21**, 12207-12212 (2005).
29. Cao, L., Hu, H. H., & Gao, D. Design and fabrication of micro-textures for inducing a superhydrophobic behavior on hydrophilic materials. *Langmuir* **23**, 4310-4314 (2007).

## 4. Transition Metal Dichalcogenides

### 4.1 Introduction

TMDs have the stoichiometric formula,  $\text{MX}_2$ , with a trigonal prismatic structure comprised of atomic layers of chalcogens ( $\text{X} = \text{S}, \text{Se}, \text{Te}$ ) and group-VI transition metals ( $\text{M} = \text{Mo}, \text{W}$ )<sup>1-2</sup>. They are stable in bulk form but also as few-layered as well as monolayer sheets. It is well understood that one single monolayer of trigonal prismatic semiconducting TMDs (such as  $\text{MoS}_2$  and  $\text{WS}_2$ ) exhibit a direct band gap which it is not present in few-layered systems<sup>3</sup>. For this reason semiconductor TMDs exhibit remarkably enhanced interaction with visible light due to this indirect-to-direct bandgap conversion at the monolayer limit, rendering these systems versatile platforms for studying light-matter interactions and for nanoscale optical device applications<sup>4-5</sup>. Given that such TMD electronic and optoelectronic devices will be exposed to the environment during operation, it is important to understand how water interacts with and wets such surfaces, which is the goal of our study. The wetting studies are performed for TMD films supported on  $\text{Si}/\text{SiO}_2$  substrates since this is the most common gate dielectric for TMD electronic and optoelectronic devices.

The previous chapters focused on how water wets mono and few-layered graphene surfaces. Since such experiments are challenging to perform on suspended (i.e. free-standing) graphene, the experiments are performed on supported graphene sheets. For graphene it was found that the underlying (supporting) substrate can exert an influence on the wetting of the monolayer graphene sheet and this effect is controlled by various factors such as the composition of the substrate, presence of charge traps in the substrate, cleanliness (or aging) of the graphene sheet and defects in the graphene. In general these effects result in a partial transmission of the van der Waals interactions between the underlying substrate and the water droplet resulting in a partial wetting transparency effect for monolayer graphene. For thicker graphene films ( $> 1$  nm thick) such effects disappear and from a wetting standpoint, the graphene film is completely decoupled from the underlying substrate.

While we developed a reasonable understanding of how water wets supported mono and few layered graphene films on substrates, there was very limited understanding on the wettability of two-dimensional (2D) transition metal dichalcogenides (TMDs).

One study has reported wetting measurements on multilayer molybdenum disulfide ( $\text{MoS}_2$ ) films on  $\text{Si/SiO}_2$  substrates but this study did not study  $\text{MoS}_2$  monolayers and also did not study ‘aging’ effects, which are known to be very significant from our prior experience with graphene<sup>6-7</sup>. To address this, the wetting properties of mono-layer, bi-layer, tri-layer and multi-layer tungsten disulfide ( $\text{WS}_2$ ) films on  $\text{Si/SiO}_2$  substrates were systematically studied and the results compared to the predictions of simple continuum wetting models. We report a partial (albeit weak) wetting transparency effect for  $\text{WS}_2$  monolayers which contradicts the predictions of simple continuum models which foretell complete wetting opacity even for a monolayer TMD sheet. The wetting contact angle of monolayer  $\text{MoS}_2$  on  $\text{Si/SiO}_2$  substrate was also measured and was shown to be close to that of monolayer  $\text{WS}_2$ . We also studied ‘aging’ effects in monolayer  $\text{WS}_2$  films and show that when all airborne contaminants are desorbed from the sample surface, the monolayer film is in fact strongly hydrophilic and not hydrophobic. Over a period of ~1 week, these airborne contaminants are re-established on the monolayer  $\text{WS}_2$  film surface and the water contact angle reverts back to  $\sim 83^\circ$ . Finally, we study the effect of substitution of chalcogens (S) with oxygen groups on monolayer TMD ( $\text{WS}_2$  and  $\text{MoS}_2$ ) surfaces. The aged TMD surface is nearly hydrophobic while the oxygen substituted region is strongly hydrophilic which allows for ‘hydrophilic-hydrophobic’ patterns to be engineered onto such surfaces. This enables liquid micro-drops arrays to preferentially nucleate and grow on the hydrophilic patches during water condensation experiments. Such a chalcogen substitution approach provides a facile means to control the spatial wettability distribution of TMD films for applications in micro and nanofluidics.

## 4.2 Synthesis and Characterization

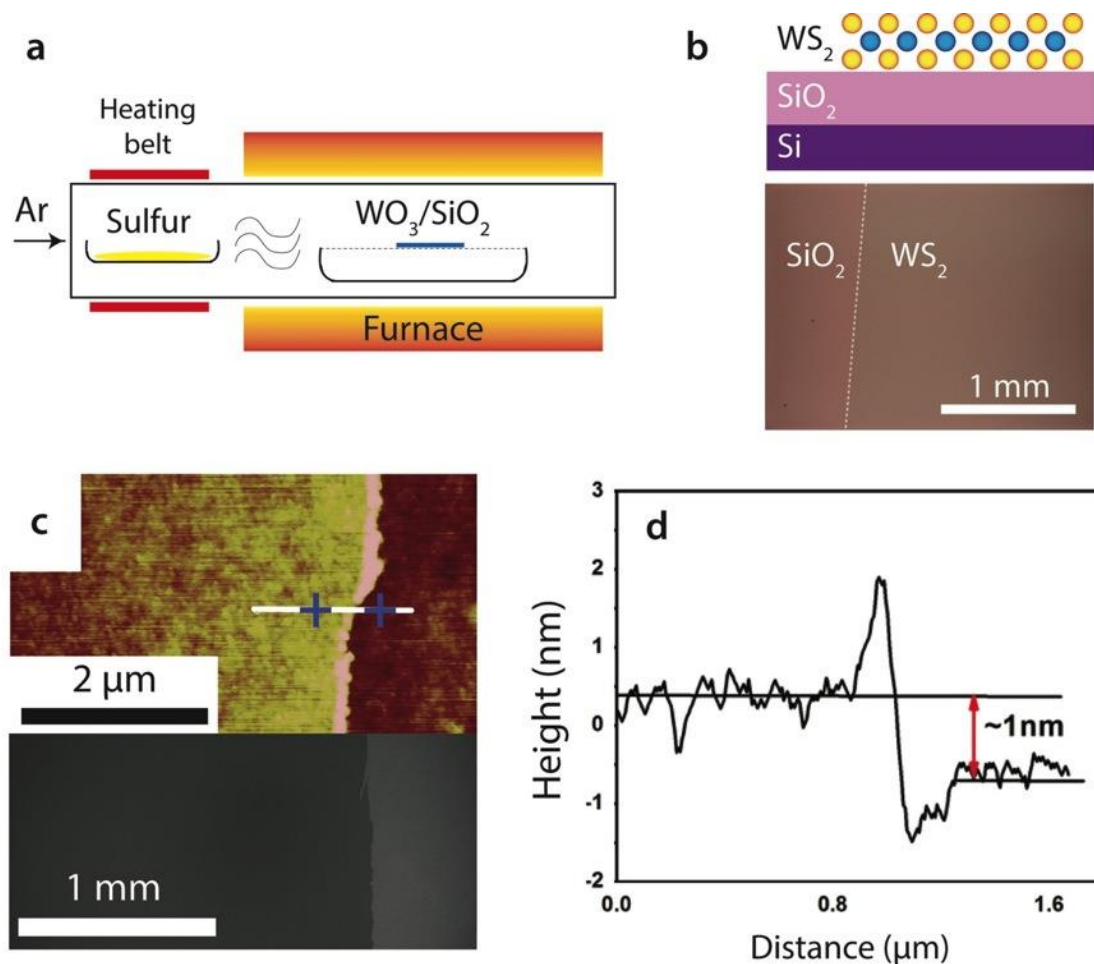


Figure 16 – (a) Schematic of the thermal reduction/sulfurization method used to deposit WS<sub>2</sub> sheets. (b) (Top) schematic of monolayer WS<sub>2</sub> film on Si/SiO<sub>2</sub> substrate, (bottom) Optical microscopy image of large area, continuous WS<sub>2</sub> film on SiO<sub>2</sub>/Si substrate, and this image is taken near the edge of the film showing the covered and exposed regions on the SiO<sub>2</sub> substrate. (c) (Top) Atomic force microscopy and (Bottom) scanning electron microscopy images of the edge region of the WS<sub>2</sub> film. (d) Atomic force microscopy line scan showing the height of the WS<sub>2</sub> monolayer film as ~1 nm.

Thin films of WS<sub>2</sub> were prepared by a thermal reduction/sulphurization scheme<sup>8</sup>. Briefly this process involves depositing a thin film of tungsten trioxide (WO<sub>3</sub>) on a Si/SiO<sub>2</sub> substrate by thermal evaporation at a base pressure of  $\sim 5 \times 10^{-7}$  torr. The films were then loaded into a quartz tube furnace and heated to  $\sim 800^\circ\text{C}$  under argon flow to maintain an inert environment. A sulphur target was also placed upstream of the hot zone of the furnace as shown in Figure 16a. The target was independently heated using a heating belt to evaporate the sulphur. When the furnace temperature reached  $\sim 800^\circ\text{C}$ , the metal oxide film was reduced completely and thinned down to an atomically thin layer. At this stage the heating belt temperature was raised to about  $150^\circ\text{C}$ , which releases sulphur into the furnace hot zone. After  $\sim 30$  minutes of reaction, the heating elements were switched off and the furnace was allowed to cool naturally. A similar process was also utilized to grow monolayer MoS<sub>2</sub> films from a MoO<sub>3</sub> precursor. The as-produced TMD films were wholly continuous, as demonstrated by optical microscopy (Figure 16b), atomic force microscopy and scanning electron microscopy (Figure 16c). AFM confirmed the average thickness (Figure 16c-d) of our as-synthesized monolayer WS<sub>2</sub> films to be  $\sim 1$  nm which is comparable to the theoretical thickness of 1.24 nm for single-layer WS<sub>2</sub>. In addition to monolayers, we also produced bi-layer, tri-layer and multi-layer ( $> 10$  layers) WS<sub>2</sub> films.

This was achieved by varying the WO<sub>3</sub> precursor film thickness. In general very thin oxide films ( $\sim 1$ -2 nm thick) produce monolayer WS<sub>2</sub> while bi-layer, tri-layer and multi-layer films could be created by simply increasing the thickness of the precursor oxide films.

Raman spectroscopy was used to characterize the few-to-single-layer WS<sub>2</sub> films using 532 nm excitation wavelength in a confocal microscopy configuration (Figure 17). Prior to the Raman study, atomic force microscopy line scans (as in Figure 16c-d) were used to independently confirm the number of WS<sub>2</sub> layers in these films. The positions and intensities (Figure 17) of the 2LA(M), E<sup>1</sup><sub>2g</sub> and A<sub>1g</sub> peaks (obtained by Lorentzian fitting) are consistent with those expected for WS<sub>2</sub>. While the intensities (Figure 17a) of the above modes did change from mono to bi to tri-layer films, the intensity ratio of these modes (e.g. E<sup>1</sup><sub>2g</sub> to A<sub>1g</sub>) did not show any definitive trend with respect to number of layers. On the other hand the frequency difference between the A<sub>1g</sub> and E<sup>1</sup><sub>2g</sub> and the

$A_{1g}$  and  $2LA(M)$  modes showed a clear increase from mono-layer to bi-layer to tri-layered films as shown in Figure 17b. This is because as the number of layers decreases the  $A_{1g}$  mode is freer to vibrate in the out-of-plane direction and therefore has decreased frequency as opposed to the in plane modes<sup>9</sup>. In this way, Raman spectroscopy characterization provides additional confirmation regarding the number of TMD layers in the film.

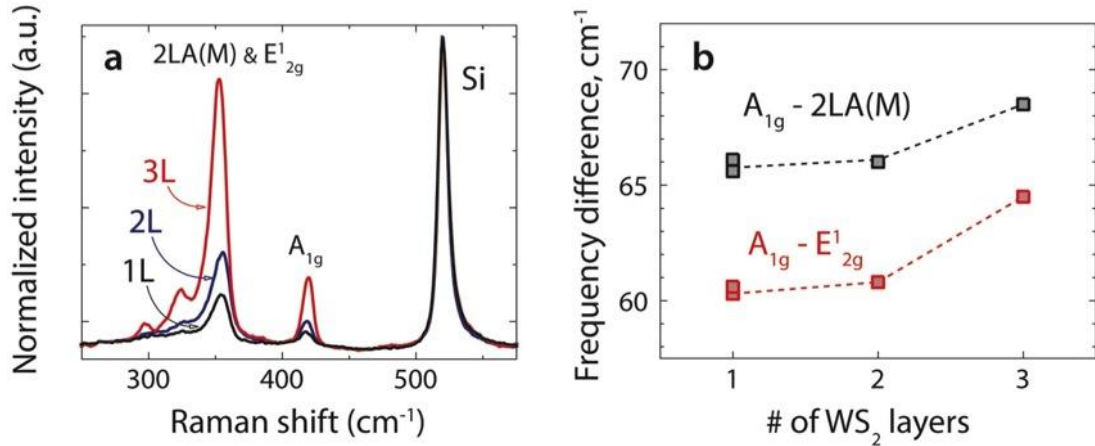


**Figure 17 – (a) Raman spectroscopy characterization (at 532 nm excitation) of monolayer, bi-layer and tri-layer WS<sub>2</sub> films on Si/SiO<sub>2</sub> wafer. (b) Difference in the frequency of various Raman active modes vs. the number of layers (mono, bi and tri) in the WS<sub>2</sub> film.**

### 4.3 Water Contact Angle Measurements

The advancing water contact angle of the various WS<sub>2</sub> films was measured using the dynamic sessile drop method via a Ramé-Hart M500 digital goniometer equipped with a dispensing needle (VICI Precision Sampling, CA, USA). First, a 1  $\mu$ l water droplet was generated using the automatic dispenser of the goniometer, based on four time-controlled volume steps of 0.25  $\mu$ l close to the sample surface. The sessile droplet was formed by fixing the needle and moving the substrate parallel to the needle orientation, using a gentle feed rate of a few micrometers per minute<sup>10</sup>. Once the droplet was in contact with the surface, additional water was pumped using a feed rate of 0.25  $\mu$ l every 3 seconds. The tests were recorded as video files and individual frames extracted for all measurements. All the tests were carried out in an air environment at room temperature (~25 °C). The axisymmetric drop-shape analysis profile (ADSA-P) method was used to

estimate the contact angle of the water droplet on the solid surface. We performed at least ten separate measurements on each sample for statistics. Figure 3a shows the static water contact angles for the mono-layer, bi-layer, tri-layer and multi-layer (bulk) WS<sub>2</sub> samples as well as the baseline Si/SiO<sub>2</sub> substrate. The SiO<sub>2</sub> substrate is strongly hydrophilic with water contact angle of ~30°. This is expected and is due to formation of hydrogen bonding networks at the water-SiO<sub>2</sub> interface which drastically increases the affinity of water to the solid surface. When a monolayer of WS<sub>2</sub> is deposited on the Si/SiO<sub>2</sub> substrate the water contact angle jumps to ~83°; we expect this is because hydrogen bonds between water and the SiO<sub>2</sub> surface can no longer develop due to the presence of the WS<sub>2</sub> film at the interface.

Interestingly the bi-layer and tri-layer films were more hydrophobic as compared to the monolayer film and showed wetting angles of ~85° and ~90° respectively. There was no measurable difference between the tri-layer and bulk samples (> 10 layers) as indicated in Figure 18a. In addition to WS<sub>2</sub>, we also tested a monolayer MoS<sub>2</sub> sheet on a Si/SiO<sub>2</sub> wafer, and the measured static water contact angle was ~82°, which was very close to the WS<sub>2</sub> result.

The thickness of one WS<sub>2</sub> layer is ~1.2 nm<sup>11</sup>. Complete opacity is expected from the WS<sub>2</sub> monolayer given this thickness- i.e. even a single sheet of WS<sub>2</sub> placed on silica increases the water contact angle from the value of silica to the value of bulk WS<sub>2</sub>. There is no wetting transition in such a continuum model which contradicts the experiments. Such discrepancy between the continuum wetting model and experiments could be attributed to many factors such as defects (e.g. sulfur mono and divacancies) that are commonly observed in transition metal dichalcogenide films grown by vapor phase nucleation and growth methods. Another possibility is the presence of charge traps or charge puddles that are ubiquitous in Si/SiO<sub>2</sub> substrates. The trapped charges may result in a relatively long range electrostatic interaction with water which could increase the affinity of water to the surface and hence reduce the wetting contact angle. After about three layers (3 to 3.5 nm thickness) of WS<sub>2</sub> this effect is screened out and the effect of the substrate is no longer felt on the wetting of the TMD film. Such long range electrostatic coupling is not modeled in the simple continuum wetting model described earlier

which only considers relatively short range van der Waals interactions. Additional in-depth study is warranted to study these effects in detail.

#### 4.4 Aging of Samples

Another key issue pertaining to water contact angle measurements is the recognition that all samples age over time. A recent study by Haitao Liu and his group demonstrates the effect of airborne contaminants on graphene and graphite surfaces<sup>7</sup>. It was shown that contrary to conventional wisdom, monolayer graphene and graphite surfaces in the absence of such contaminants are hydrophilic and not hydrophobic (with water contact angles as low as  $\sim 44^\circ$  instead of the expected value of  $\sim 90^\circ$ ). The contact angle actually increases upon exposure to the ambient atmosphere. Using X-Ray photoelectron spectroscopy and infrared spectroscopy the authors show how airborne hydrocarbons adsorb on to graphitic surfaces. To further illustrate this aging effect, thermal annealing and ultraviolet  $O_3$  treatments are used to remove the hydrocarbon contaminants, resulting in a concurrent decrease in the water contact angle. The samples are then allowed to develop a new passivating layer of hydrocarbons and the contact angle values increase as expected when plotted as a function of exposure time.

The TMD samples tested so far were all characterized for their wetting properties several weeks after they were first synthesized. Aging involves adsorption of airborne contaminants (mainly hydrocarbons) on the surface of the TMD sheets. To investigate such aging issues and their impact on the wettability of TMD sheets, we heated a  $WS_2$  monolayer on Si/SiO<sub>2</sub> in an inert Ar atmosphere to  $\sim 550^\circ C$  for  $\sim 1$  hour and then allowed the sample to cool back to room temperature in the Ar environment. Heating to  $\sim 550^\circ C$  has been shown to successfully desorb the majority of airborne contaminants from graphene and graphitic surfaces. After cooling to room temperature, this clean (or fresh) sample was immediately transferred in a gas tight container filled with Ar to the contact angle measuring set up and its wetting response was recorded on expose to ambient air (Figure 18b). The result indicates that the wetting contact angle increased rapidly from  $\sim 70^\circ$  to  $\sim 77^\circ$  in  $\sim 20$  minutes. Subsequently the wetting angle continued to rise gradually over a period of  $\sim 1$  week and finally stabilized at  $\sim 83^\circ$  which matches very well the result in figure 3a for an aged  $WS_2$  monolayer.

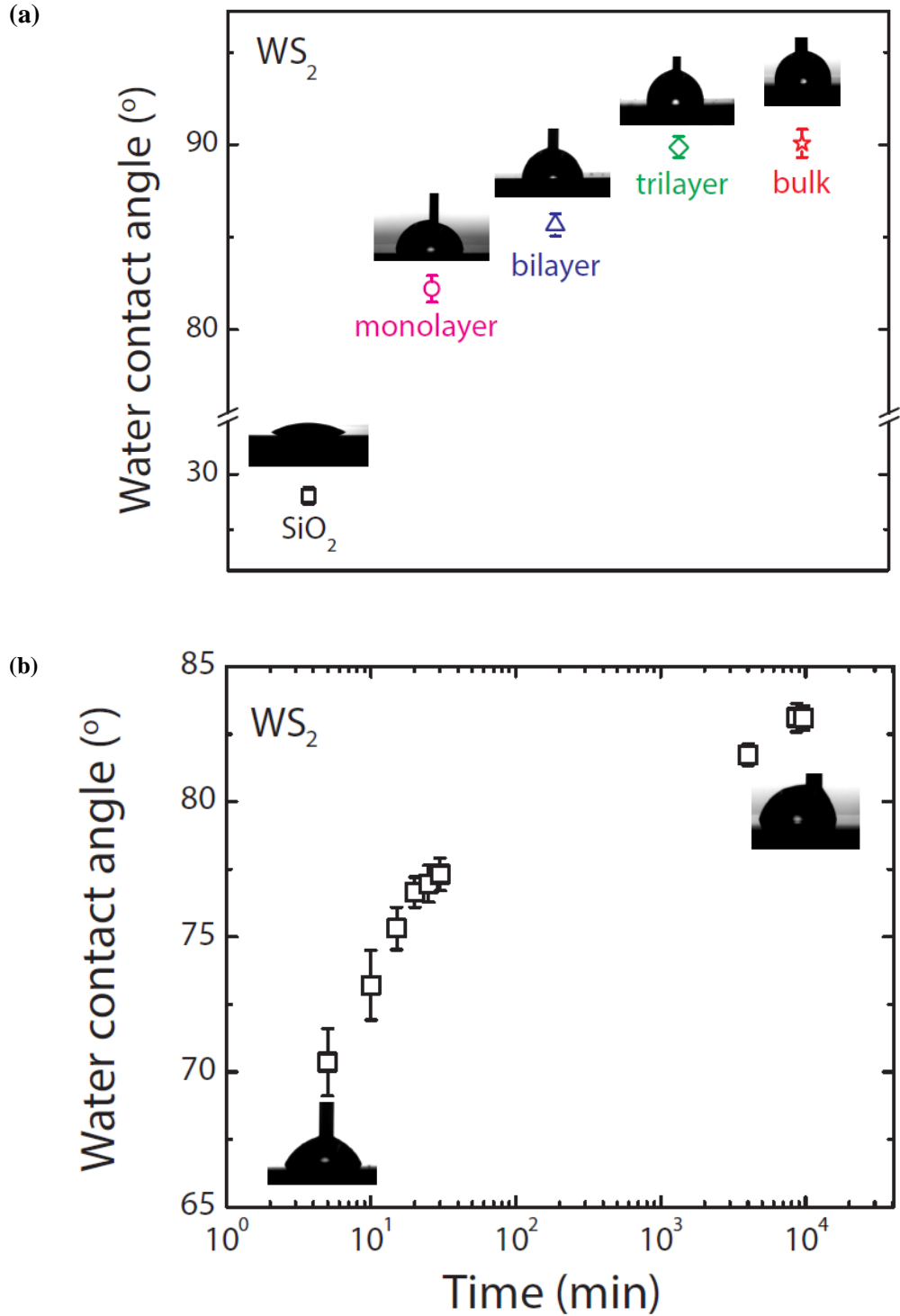


Figure 18 – (a) Static water contact angle measurements for WS<sub>2</sub> films with varying number of layers on Si/SiO<sub>2</sub> substrate. (b) Aging dynamics of a monolayer WS<sub>2</sub> film showing the formation of a hydrocarbon layer that increases the water contact angle over time.

While the effect of airborne hydrocarbon contaminants cannot be avoided in practical situations it is important to recognize that similar to graphene, perfectly clean TMD monolayers are intrinsically ‘hydrophilic’ and not hydrophobic. After  $\sim 1$  week, the aging process appears to reach equilibrium, with the water contact angle stabilizing and then remaining constant at further times. It should be noted that the TMD nanosheets used in practical applications are likely to represent such fully aged samples that exhibit close to hydrophobic behavior.

#### **4.5 Chalcogen Substitution for Hydrophobic/Hydrophilic Patterning**

Another noteworthy feature of TMDs is that even a single-layer of  $\text{WS}_2$  or  $\text{MoS}_2$  is a composite of a relatively more hydrophilic metal and a relatively less hydrophilic chalcogen atom. The chalcogen atom (as for example Sulphur), could potentially be expelled from the structure by exposure to Ar plasma bombardment. The replacements for the chalcogens are possibly oxygen atoms from the ambient which will likely occupy the sulphur vacancy sites. Oxygen is known to be hydrophilic due to its propensity to form hydrogen bonds with water molecules. As a result, such oxygen doped TMD sheets are expected to be more hydrophilic compared to the original TMD sheet. Argon plasma bombardment was used to create hydrophilic regions in a hydrophobic (aged)  $\text{WS}_2$  layer by depleting it of sulfur (Figure 19a). Briefly, as-synthesized films were exposed to argon ion irradiation (25W, 200 mtorr) using a commercial plasma cleaner (Nanoclean Model 1070, Fischione Instruments) for various times. X-ray photoelectron spectroscopy (Figure 19b) revealed a decrease in the sulfur-to-tungsten ratio with increased plasma treatment time from approximately two to one. Meanwhile, the tungsten-to-silicon ratio remained constant (Figure 19b). This suggests the preferential removal of sulfur atoms from the  $\text{WS}_2$ , due to our plasma treatment. The core-level tungsten 4f spectra exhibit significant asymmetric broadening towards higher binding energies with increased plasma treatment time, indicating increased average oxidation state of the tungsten atoms. This is likely due to adsorption of oxygen (which is more electronegative than sulfur) at sulfur vacancies upon exposure to air, thereby increasing the average oxidation state of the tungsten. Sulfur substitution at vacancy defect sites has been previously observed in high-resolution transmission electron microscopy experiments in exfoliated

MoS<sub>2</sub> monolayers<sup>12</sup>. We took advantage of such chalcogen substitution phenomena to engineer hydrophilic-hydrophobic patterns on the same monolayer samples. For this, a silicon wafer patterned with an array of 10-micron size holes was used to selectively mask certain regions of the WS<sub>2</sub> film during a 20 second argon plasma irradiation treatment cycle. Condensation tests were performed in ambient air at a temperature of ~19°C and a relative humidity of ~70%, corresponding to a dew point temperature of ~16°C. The testing apparatus was installed under high resolution microscope. The sample was horizontally put on a cold plate, which was controlled at ~4°C by a circulating chiller. After condensation experiment, the temperature of the cooling stage was increased to 30°C gradually. The evaporation result was recorded using the same resolution as the condensation experiment. The condensation result is shown in Figure 19c for the WS<sub>2</sub> film. The top panel in Figure 19c shows the condensation result on a monolayer WS<sub>2</sub> film without plasma treatment indicating liquid drops nucleating at random locations on the film surface. By contrast for the plasma treated WS<sub>2</sub> film (lower panel of Figure 19c) we observe nucleation and growth of water drops on the strongly hydrophilic regions with diameter of ~ 10 microns which correlates well to the size of the opening in the mask that was placed on the sample during the plasma treatment. Clearly these oxygen doped regions are strongly hydrophilic and attract water during the condensation experiment.

The net result of this is that we can pattern liquid microdrop arrays on surfaces in a facile manner with possible applications in microfluidics. This idea could in principle be extended to nanodrops by using a pattern with nanopores rather than the 10 micron size pores used in this experiment. These results were also reproducible for monolayer MoS<sub>2</sub> as shown in Figure 19d. The top panel shows random nucleation of drops on the hydrophobic (i.e. aged) MoS<sub>2</sub> surface. By contrast after exposure to ~20 seconds of Ar plasma through the aforementioned mask with periodic array of ~10 micron size openings, the distribution of water clusters is no longer random and follows a periodicity and size that matches near perfectly the pattern of the mask through which the plasma treatment was carried out. After condensation for about 1 to 2 minutes, the samples were gradually heated to ~30° C and the water drops were evaporated off the sample surface without damaging the TMD film.

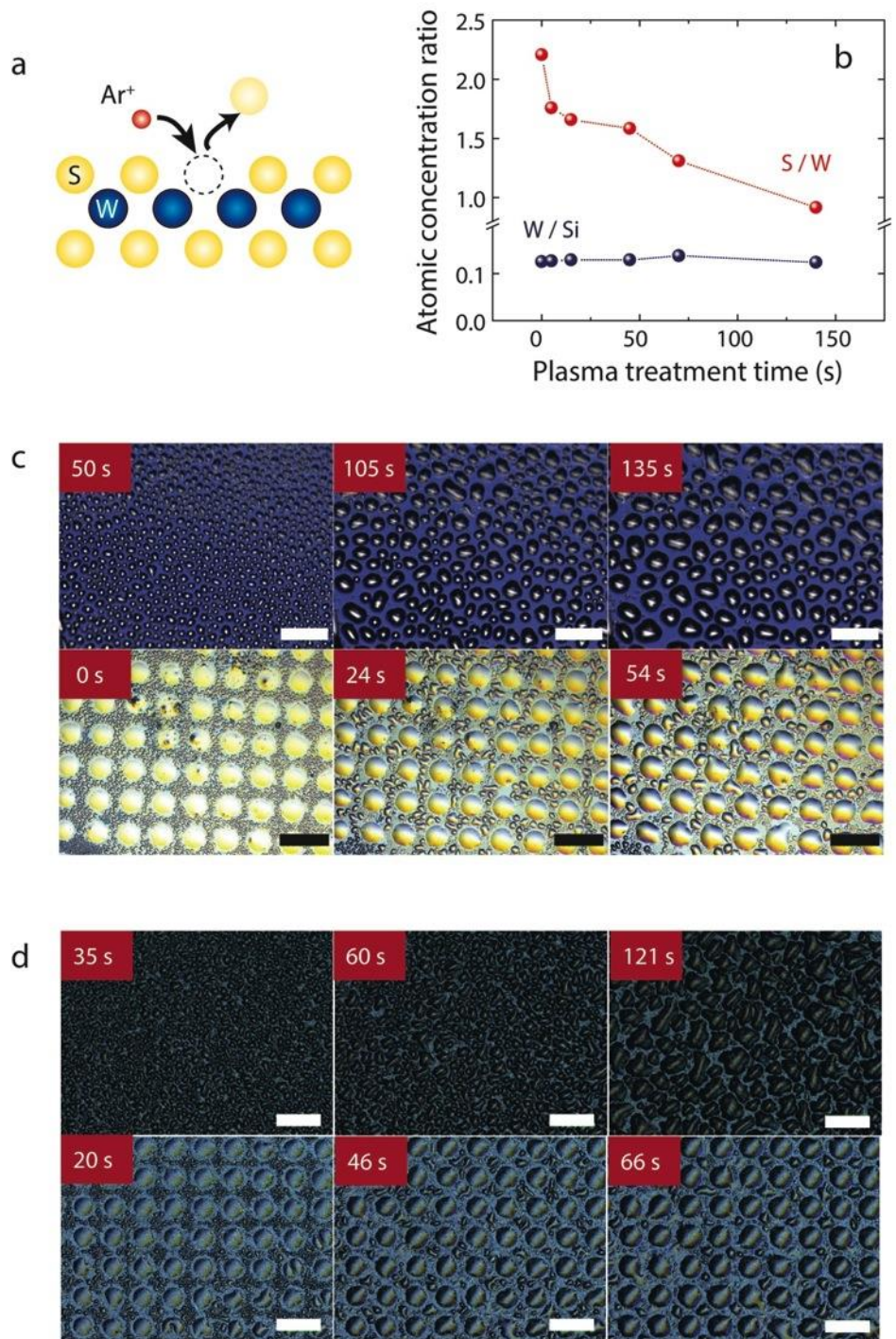


**Figure 19 – (a) Schematic of chalcogen substitution with oxygen using argon plasma treatment. (b) XPS analysis of Ar plasma treated  $WS_2$  showing removal of sulfur atoms with progressive plasma deposition time; the sulfur appear to be removed from the top surface of the film that is exposed to the plasma. (c) (Top) Condensation of water drops on untreated  $WS_2$ , (Bottom) Condensation on plasma-patterned  $WS_2$  surface. (d) Top and bottom show corresponding condensation results for a monolayer  $MoS_2$  film.**

## 4.6 Summary

In summary this work has provided fundamental information on the wettability of mono and few-layered films of transition metal dichalcogenides supported on silicon/silicon-dioxide wafers. The results indicate a noticeable (but weak) effect of the substrate on the wetting of the TMD film which contradicts the predictions of wetting opacity from simple continuum wetting models. Clearly there is a need for improved and more realistic wetting models to capture the physics of TMD-substrate interaction. We also show that TMDs undergo a powerful aging effect as airborne contaminants are established on the film surface. This aging was shown to mask the intrinsic hydrophilicity of monolayer TMD materials to a great extent. Finally we demonstrate the principle of chalcogen (sulfur) substitution with oxygen in TMDs to engineer well-controlled hydrophobic-hydrophilic patterns on the same monolayer TMD sheet. Such patterns can be used to engineer periodic arrays of microdrops on surfaces in a facile and effective manner.

## 4.7 References

1. Wilson, J. A., & Yoffe, A. D. The transition metal dichalcogenides discussion and interpretation of the observed optical, electrical and structural properties. *Adv. Phys.* **18**, 193-335 (1969).
2. Wilson, J. A., Di Salvo, F. J., & Mahajan, S. Charge-density waves and superlattices in the metallic layered transition metal dichalcogenides. *Adv. Phys.* **24**, 117-201 (1975).
3. Wang, Q. H., Kalantar-Zadeh, K., Kis, A., Coleman, J. N., & Strano, M. S. Electronics and optoelectronics of two-dimensional transition metal dichalcogenides. *Nat. Nanotechnol.* **7**, 699-712 (2012).
4. Friend, R.H., & Yoffe, A. D. Electronic properties of intercalation complexes of the transition metal dichalcogenides. *Adv. Phys.* **36**, 1-94 (1987).
5. Wilson, J. A., Di Salvo, F. J., & Mahajan, S. Charge-density waves in metallic, layered, transition-metal dichalcogenides. *Phys. Rev. Lett.* **32**, 882 (1974).
6. Gaur, A. P. *et al.* Surface Energy Engineering for Tunable Wettability through Controlled Synthesis of MoS<sub>2</sub>. *Nano Lett.* **14**, 4314-4321 (2014).
7. Li, Z. *et al.* Effect of airborne contaminants on the wettability of supported graphene and graphite. *Nat. Mater.* **12**, 925-931 (2013).
8. Gutiérrez, H. R. *et al.* Extraordinary room-temperature photoluminescence in triangular WS<sub>2</sub> monolayers. *Nano Lett.* **13**, 3447-3454 (2012).
9. Berkdemir, A. *et al.* Identification of individual and few layers of WS<sub>2</sub> using Raman Spectroscopy. *Sci. Rep.* **3**, (2013). doi: 10.1038/srep01755
10. Lander, L. M., Siewierski, L. M., Brittain, W. J., & Vogler, E. A. A systematic comparison of contact angle methods. *Langmuir*, **9**, 2237-2239 (1993).
11. Kuc, A., Zibouche, N., & Heine, T. Influence of quantum confinement on the electronic structure of the transition metal sulfide TS<sub>2</sub>. *Phys. Rev. B*, **83**, 245213 (2011).
12. Komsa, H. P. *et al.* Two-dimensional transition metal dichalcogenides under electron irradiation: defect production and doping. *Phys. Rev. Lett.* **109**, 035503 (2012).

## 5. Application Development using Wetting Science

### 5.1 Graphene Additives for Metal Cutting Fluids

#### 5.1.1 Introduction

Sustainable manufacturing practices are desirable not only from an environmental and ecological perspective, but also because of the economic benefit that a reduced hazardous waste stream offers. There is a clear need for the development of high-performance, environmentally benign cutting oils for metal-working<sup>1-2</sup>. Manufacturing industries currently use petroleum-based cutting oils. In addition to their dependence on fossilized hydrocarbon sources and large resulting carbon footprint, the usage of hazardous chemical additives such as sulfur and chlorine also create various problems<sup>3</sup>. Studies estimate that ~50% of these chemicals end up in the environment; making them a leading cause for health issues affecting more than a million workers every year<sup>4-5</sup>.

Work described in the first subsection focuses on synthesizing graphene with different functionalization groups in order to create stable dispersions in metal cutting oils. First, the effect of functional groups on dispersion of graphene platelets was studied for standard cutting fluids such as Castrol Clearedge™ 6519. An alternative is to use plant based cutting oils<sup>6</sup>. Plant derived oils have a high viscosity index, meaning their viscosity changes less with temperature variations. They also have low volatility and high flash points, which makes them less likely to ignite spontaneously<sup>7</sup>. They are also biodegradable and non-toxic, making them a good choice for environmentally-benign cutting fluids. Plant-based cutting oils are currently being used in some industries, but are limited in scope due to their poor thermal and oxidative stability. This restricts them from being used in demanding machining applications, wherein large cutting forces and high temperatures are experienced at the metal-tool interface<sup>7</sup>. Nanoscale additives, such as graphene in this study, improve cooling and lubrication performance for plant based cutting oils and make them suitable for high performance machining environments<sup>8</sup>.

---

Portions of this chapter previously appeared as:

Chu, B., Singh, E., Koratkar, N., & Samuel, J. Graphene-Enhanced Environmentally-Benign Cutting Fluids for High-Performance Micro-Machining Applications. *J. Nanosci. Nanotechnol.* **13**, 5500-5504 (2013).

Smith, P.J. *et al.* Graphene oxide colloidal suspensions mitigate carbon diffusion during diamond turning of steel. *J. Manuf. Proc.* **17**, 41-47 (2015).

The effect of graphene platelets on the cutting performance of semi-synthetic cutting fluids was recently explored by Samuel et al.<sup>9</sup>. The added graphene platelets reduce cutting forces and cutting temperatures as measured during machining processes. The primary reason for this is the nanoscale dimensionality of graphene that allows the platelet to insert itself within the tool-workpiece interface. Sliding and shearing of the graphene platelets and their inherently high thermal conductivity result in reduced cutting forces and better heat dissipation.

Although the effect of graphene platelets in semi-synthetic cutting fluids has been studied to an extent, methods described here may be used to vary graphene platelet size and dimensionality when dispersed in commercial synthetic cutting fluids such as Castrol Clearedge™ 6519<sup>10</sup>. Additionally, plant-based oils have a distinct wetting behavior as compared with polar aqueous solvents, mandating a different chemical functionalization strategy. Here it is shown that graphene sheets may be tailored to form stable dispersions in canola oil, a popular plant based cutting oil. The graphene laden canola oil is characterized based on its kinematic viscosity, thermal conductivity and coefficient of friction. Micro-machining tests were also performed to study the effect of these graphene platelets on cutting forces, cutting temperatures, and surface finish of the machined parts, and have not been mentioned here for the sake of brevity. Details regarding the machining tests and their methodology to study the effect of graphene platelets may be found in Reference 8.

### **5.1.2 Dispersing Graphene in Aqueous and Non-Aqueous Mediums**

To successfully use graphene platelets as additives in a cutting fluid, the dispersion needs to be stable over time. Any agglomeration or aggregation of individual platelets will reduce the benefits that are offered by graphene's extreme thinness. There are many studies in existing literature exploring pathways for the creation of stable, aqueous dispersions of single or few layered graphene<sup>11</sup>. These methods usually exploit the polarity of water molecules in conjunction with surfactants for better dispersion stability.

---

Mukherjee, R. *et al.* Defect-induced plating of lithium metal within porous graphene networks. *Nat. Comm.* **5** (2014). doi: 10.1038/ncomms4710

### 5.1.2.1 Semi Synthetic Cutting Oils - Castrol Clearedge™ 6519

The approach taken here to obtain different sized graphene- oxide platelets in semi-synthetic cutting fluids first involved the production of graphite oxide (GO) as a precursor. The GO was subsequently exfoliated using either a thermal shock or an ultrasonication technique to produce platelets with varied lateral size, thickness, and oxygen functionalization. The thermal shock process resulted in the exfoliation of GO in a powder form, which was then dispersed in the fluid medium of choice, whereas, the ultrasonication process resulted in direct exfoliation of the GO in the fluid medium.

Figure 20a shows the overall process flow for GOP production. The production of graphite oxide from raw graphite was accomplished using two oxidation techniques, 1) the Modified Hummer's (MH) method<sup>12</sup>, which produces heavily oxidized graphite, and 2) the Staudenmaier method<sup>13</sup> which produces lightly oxidized graphite. Figure 20b shows the results from the X-Ray diffraction used to characterize GO obtained from these two methods. The Modified Hummer's method completely oxidizes the graphite resulting in a diffraction peak shift from the graphitic  $\sim 26^\circ$  to graphite oxide at  $\sim 11^\circ$ , corresponding to an increase in *d-spacing* from  $\sim 0.34$  nm to  $\sim 0.81$  nm between the individual graphite layers. However, with the Staudenmaier method, graphite oxide is produced with a peak observed at  $\sim 13^\circ$ . This indicates a lower increase in the *d-spacing* of  $\sim 0.67$  nm, which in turn points to incomplete oxidation. The presence of a residual graphitic peak at  $26^\circ$  also confirms the milder oxidation that is achieved with the Staudenmaier method. This difference between the two types of GO plays a role in how these precursors may be further used for exfoliation to produce graphene oxide platelets<sup>13</sup>.

***Thermal Shock Exfoliation of Graphite Oxide – Reduced Graphene Powder:*** The thermal exfoliation technique works by consuming some of the graphite oxide to form carbon dioxide gas, which in-turn induces a tremendous interlayer pressure in the remaining stack-structure of the GO. This pressure causes the graphite oxide to explode into single or multiple-layer, partially-deoxygenated, thermally-reduced graphene oxide platelets (TR GOPs).

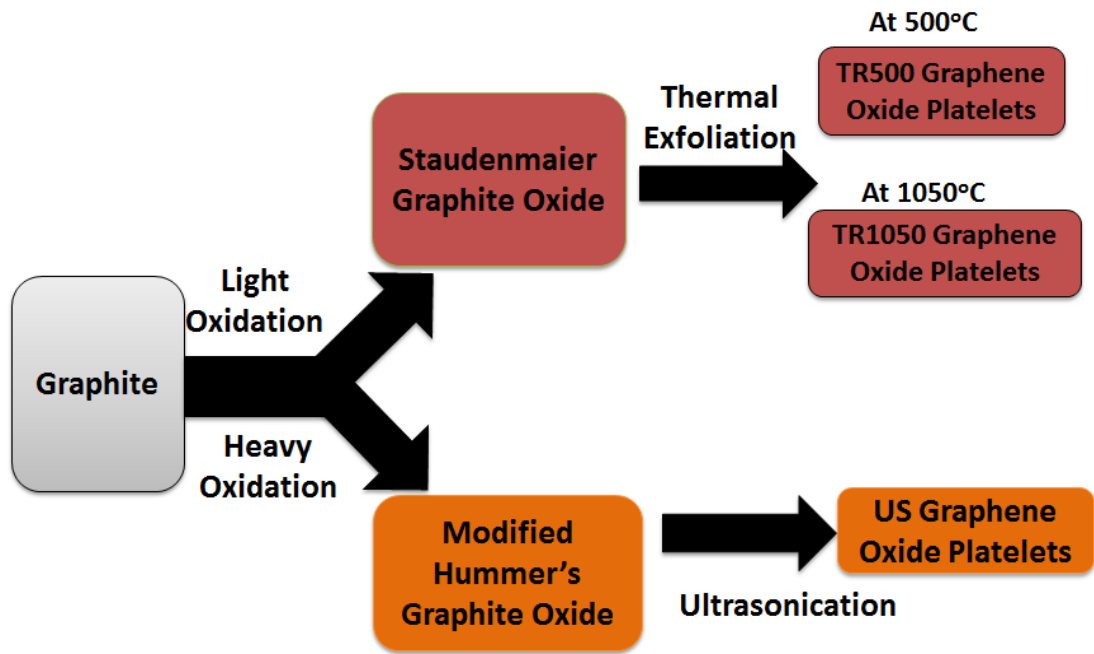
The GO produced from the Modified Hummer's method exfoliated well but gave extremely low yields when subjected to high temperatures in the thermal shock furnace.

This is attributed to the high oxygen content in the GO produced using this method. The presence of such high oxygen content causes most of the graphite to get consumed in the production of CO<sub>2</sub> gas during the thermal shock, which in-turn results in a poor yield of TR GOPs. In addition to the poor yield, the furnace also showed deposits of a soot-like material that caused the TR GOPs to adhere to the walls of the fabrication vessel, thereby increasing the difficulty of extracting the TR GOPs. The GO produced using the Staudenmaier method was observed to be better suited for thermal exfoliation. This is attributed to the limited amounts of oxygen moieties in the GO produced using this method, which results in a lower consumption of graphite during the production of CO<sub>2</sub>. Thermal shock was carried out on the Staudenmaier GO at two temperatures, 500°C and 1050°C. The resulting thermally-reduced graphene oxide platelets will be referred to as TR500 and TR1050, respectively.

***Ultrasonication-based Exfoliation of Graphite Oxide – Aqueous Processing:***

In this technique, graphite oxide is exfoliated in-solution using ultrasonication energy. The graphene oxide platelets produced using this method will be referred to as US GOPs. Deionized (DI) water was chosen as the suspension medium since it is used as a diluent for semi-synthetic cutting fluids. The GO obtained using the Modified Hummer's method was seen to be more suitable for this technique as opposed to the one obtained using the Staudenmaier method. This is attributed to the fact that the MH method over-oxidizes the GO with strong acidic groups. Models for graphite oxide produced using the MH method have shown that there exists acidic oxidative debris on the surface of the GO<sup>13</sup>. This oxidative debris acts as a surfactant in aqueous suspensions and renders the GO hydrophilic, allowing it to be easily dispersed in water. Such surfactant groups are absent in the case of the GO obtained from the Staudenmaier method, which impedes their suspension in deionized water.

(a)



(b)

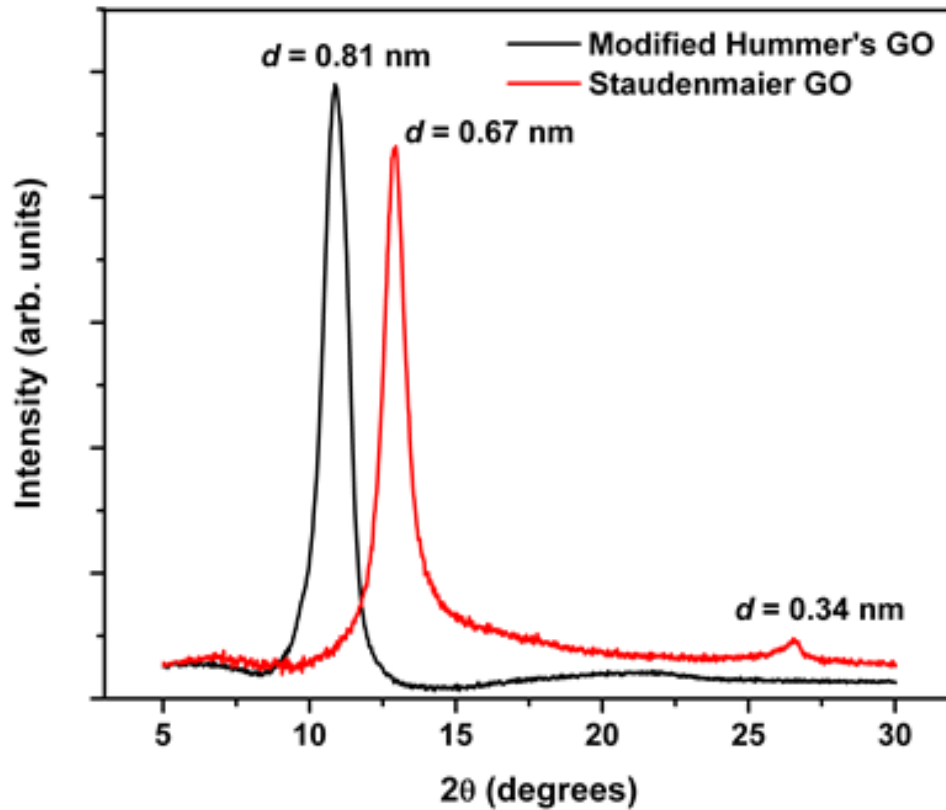
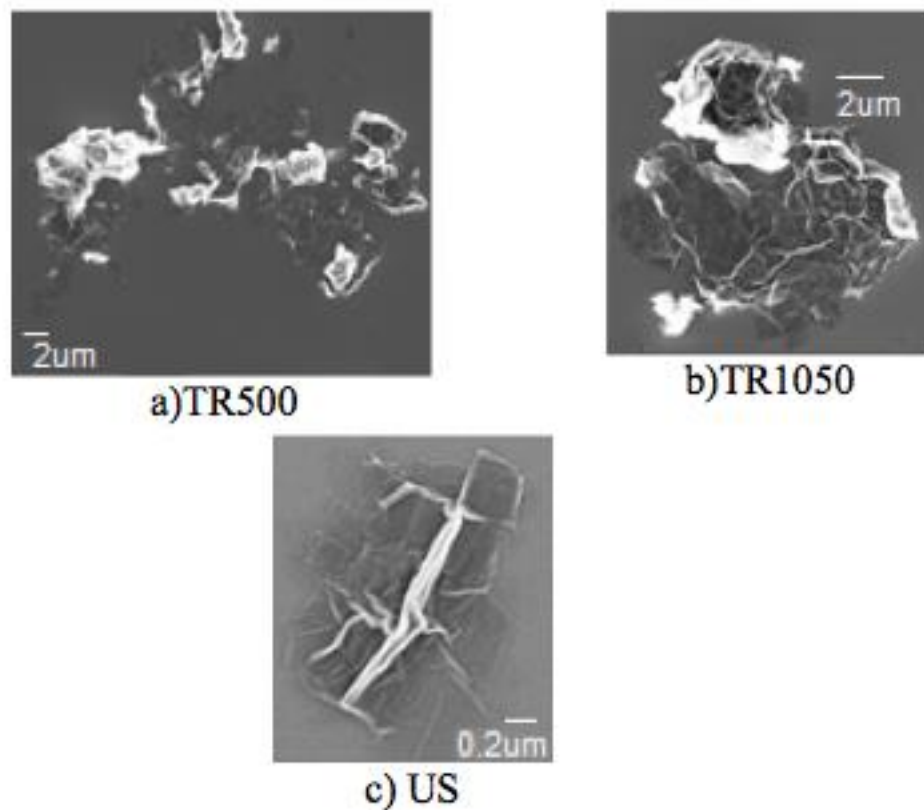


Figure 20 – Graphite to Graphene production. (a) Process flow schematic for the creation of graphene platelets with different aspect ratios and thicknesses in water-based synthetic cutting oils. (b) Modified Hummer's method over oxidizes the graphite as compared to Staudenmaier method, which exhibits lesser expanded when interlayer spacing is analyzed using X-Ray Diffraction.<sup>10</sup>

Figure 21a-c shows sample scanning electron microscope (SEM) images of the TR500, TR1050, and US graphene oxide platelets used in this study. Even though the lateral size measurements could be estimated using the SEM, this measurement technique has a major limitation. The surfactants present in semi-synthetic cutting fluids affect the colloidal stability of the GOP suspensions, which in-turn influences the agglomeration of GOPs in the solution. Therefore, the ex-situ size analysis of the platelets may not be an accurate representation of the effective GOP lateral dimensions that are seen by the tool and the work-piece. With this in mind, alternate techniques that allowed for in-solution measurement of the lateral dimension of the GOPs were explored.



**Figure 21 – SEM image analysis of graphene platelets. (a) Reduced graphene oxide exfoliated at 500 °C. (b) Reduced graphene oxide exfoliated at 1050°C. (c) Ultrasonicated graphene oxide sheets. Agglomeration of TR-GO flakes ex-situ mandates use of alternate techniques to analyze in-situ dimensionality of these flakes.<sup>10</sup>**

### ***Dynamic Light Scattering for Estimating In-solution Lateral Size***

This technique is used to determine the size distribution of the particles in a solution. It relies on the principle, that when colloidal particles being measured are of the same order of magnitude as the wavelength of the monochromatic laser source being shone on the solution, the particles will scatter the light. This scattering causes constructive and destructive interference, which is recorded by a receiver. Using such a signal, over time, one can calculate a size distribution of the particles by relating the fluctuation in signal intensity to Brownian motion. DLS is typically used for estimating of the hydrodynamic diameter of spherical particles in solution form. When used on a GOP suspension, this method will not provide the absolute value of the lateral dimensions of the GOP sheets. However, it is able to provide a numerical hydrodynamic diameter value, which better represents the lateral size seen by the tool and the workpiece.

A 1:7 mixture by volume of Castrol Clearedge™ 6519 semi-synthetic cutting fluid in DI water was used in these experiments as the baseline cutting fluid. Figure 22a-c show the DLS analysis of the three different types of graphene oxide suspensions made using this baseline cutting fluid. As seen in the figures, a bi-modal size distribution is apparent where oil droplets with ~50nm hydrodynamic diameter appear in the emulsion along with the hydrodynamic diameters of the GOP clusters. As seen from the DLS data, the hydrodynamic diameter of the ultrasonicated graphene oxide platelets (US GOPs) is 120 nm. The thermally-reduced graphene oxide (TR GOPs) hydrodynamic diameters were seen to be 562 nm and 2781 nm at the reduction temperatures of 500°C and 1050°C, respectively.

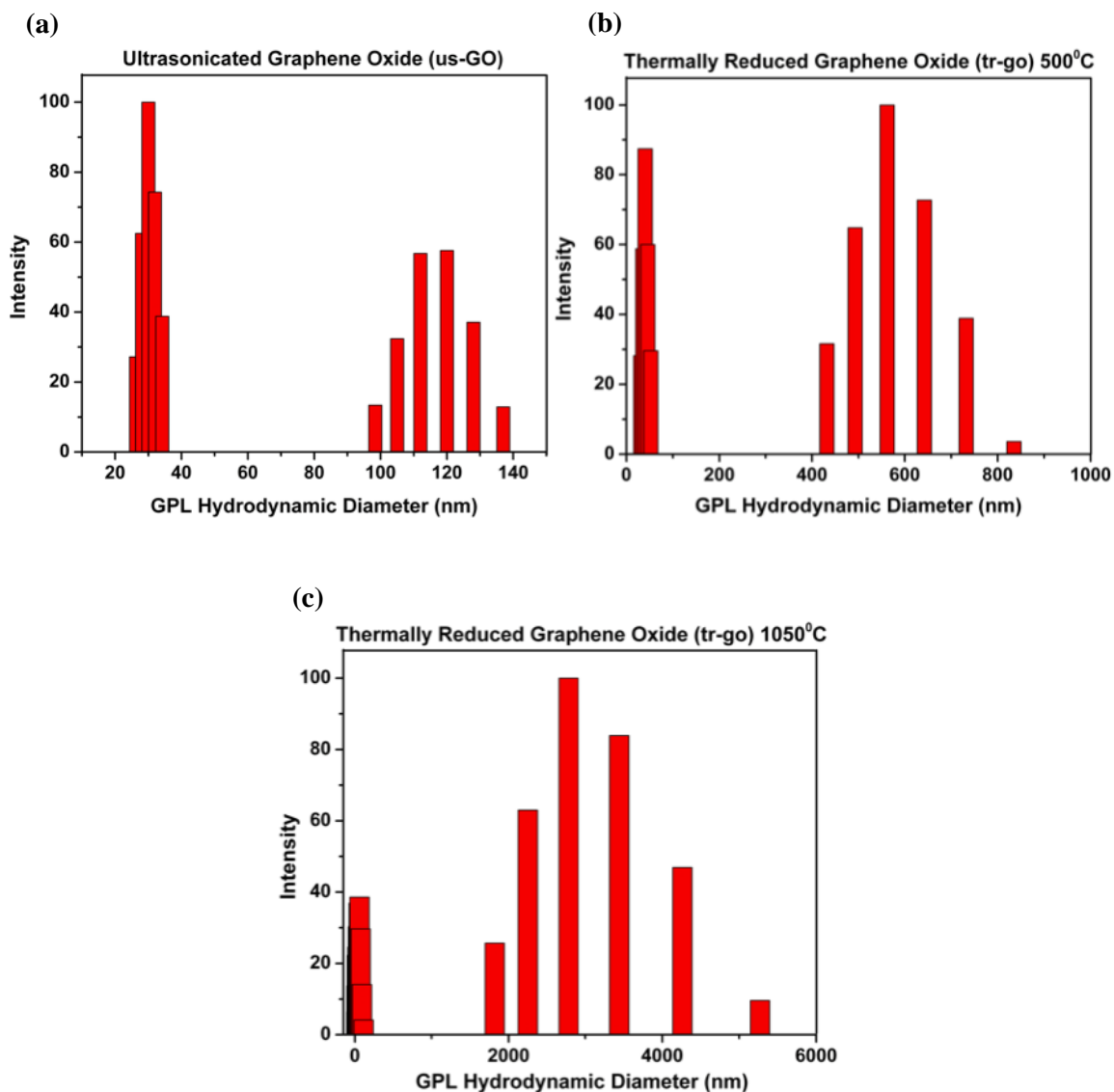


**Figure 22 – Dynamic Light Scattering (DLS) data for various functionalized graphene platelets. (a) Ultrasonicated graphene oxide produced via Modified Hummer's method shows the smallest hydrodynamic diameter with a mean of ~120 nm owing to electrostatic repulsion of sheets. (b) TR-GO 500°C shows larger flakes in dispersion as a result of lesser oxygen functional groups and more hydrophobic nature. (c) TR-GO 1050°C agglomerates further as higher temperature thermal exfoliation reduces oxygen moieties to a great extent and the sheets become highly hydrophobic.<sup>10</sup>**

It should be noted that while the DLS data (Figure 22) provides the estimated hydrodynamic diameter for a spherical particle, a direct correlation exists between the characteristic length obtained through this measurement and the actual lateral size of the graphene platelet in suspension. Considering a higher intensity of thermal shock would result in rapid deoxygenation and thus better exfoliation of individual graphene sheets, one would expect that the higher the extent of exfoliation, the smaller the lateral size of the graphene platelets in-solution. However, the DLS data contradicts this assumption. It was found that TR1050, which should be smaller and thinner based on exfoliation temperature, actually formed larger flakes than TR500 in-solution. The higher temperature of thermal shock thus produced larger sized ( $\sim 3 \mu\text{m}$ ) GOPs in-solution, whereas the lower temperature of thermal shock produced smaller-sized sheets ( $\sim 0.5 \mu\text{m}$ ) in-solution.

Although this behavior is counterintuitive at first, it makes more sense when the role played by the oxygen functional groups is examined carefully. The polar oxygen functional groups present on graphite oxide are removed violently during the thermal shock process, as carbon from the graphite reacts with the oxygen to form carbon oxides that generate extremely high interlayer pressures. This results in the rapid exfoliation of graphite oxide into reduced graphene oxide flakes. Higher temperatures do produce flakes with higher surface area, but these GOPs have much lesser oxygen content<sup>13</sup>. Residual oxygen functional groups play a crucial role in reducing agglomeration through electrostatic repulsion between individual platelets when dispersed in an aqueous environment. For the TR GOPs, there is a greater loss of oxygen moieties when the platelets are exfoliated at  $1050^\circ\text{C}$  than when the exfoliation is conducted at  $500^\circ\text{C}$ . The lower surface energy of highly-reduced graphene oxide platelets (that are formed by exfoliation at  $1050^\circ\text{C}$ ) is responsible for their hydrophobicity and resultant agglomeration. This is evident from the observable hydrodynamic diameters that are much larger for TR1050 as compared to TR500. A Gaussian distribution exists for the measured hydrodynamic diameter, with TR500 exhibiting a high probability for values  $\sim 562 \text{ nm}$ , while the TR1050 shows much larger agglomerates with a mean diameter of  $\sim 2781 \text{ nm}$ . This difference is significant and indicates that TR500 is better dispersed in aqueous solvents. The presence of oxygen groups also explains why US GOP suspensions exhibit

the smallest hydrodynamic diameter of 120 nm, as the polar groups interact with water molecules enabling better dispersibility.

### 5.1.2.2 Plant Derived Canola Oil

In contrast to aqueous solvents where the H<sub>2</sub>O molecule is highly polar, the long chain fatty acids in canola oil are non-polar in nature. In such a situation, covalent functionalization of the graphene flakes with carboxyl groups may help, considering the long acid molecules (alpha-linoleic acid) have carboxyl groups at their ends. Similar methods have been used to disperse carbon nanotubes (CNT's) and microwave exfoliated graphene nano-platelets previously<sup>14-15</sup>.

Carboxylated graphene (purchased from ACS Materials) was dispersed in canola oil via horn/tip sonication performed with a Sonics Vibra Cell VCX750. Horn sonication was conducted for a period of 4 hours at 40% of the maximum amplitude possible for this machine. The concentration of carboxyl graphene in canola oil was then varied between 0.05%; 0.10% and 0.15% by weight. For these concentrations, stable and homogenous dispersions were obtained. Higher mass loadings of graphene were avoided as the dispersion becomes oversaturated due to which incomplete exfoliation and agglomeration of graphene flakes was observed.

Scanning electron microscopy (SEM) (Figure 23a) and X-Ray Photoelectron Spectroscopy (XPS) (Figure 23b) are used to characterize the carboxyl graphene flakes. The 2-dimensional layered flakes are found to be several microns wide in their lateral dimensions. Such flakes can easily slide in between the tool-workpiece interface and shear in order to provide a reduction in cutting forces. The XPS spectra clearly show prominent peaks for hydroxyl (286.4 – 286.7 eV) and carboxyl functional groups (288.0-289.4 eV).

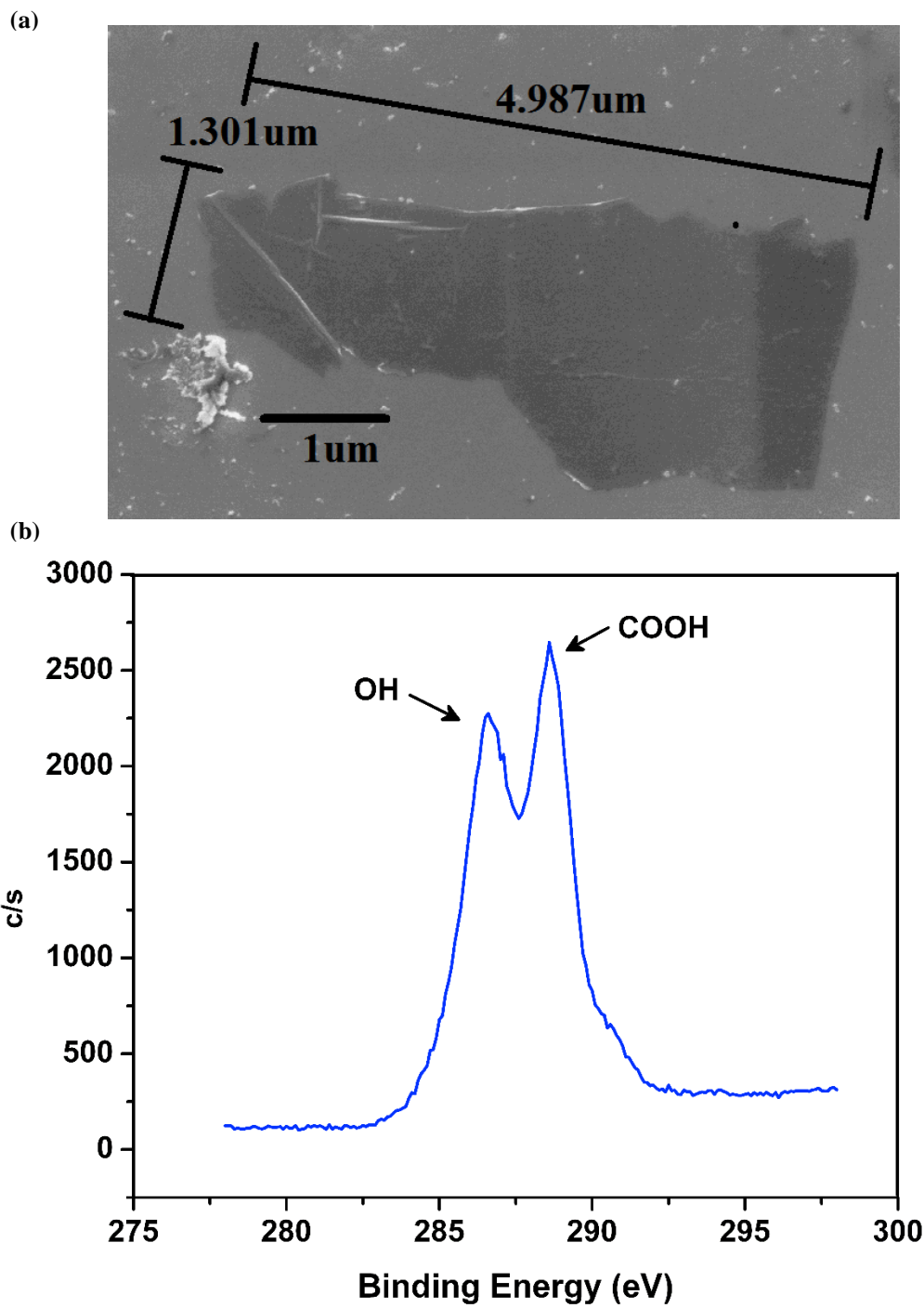
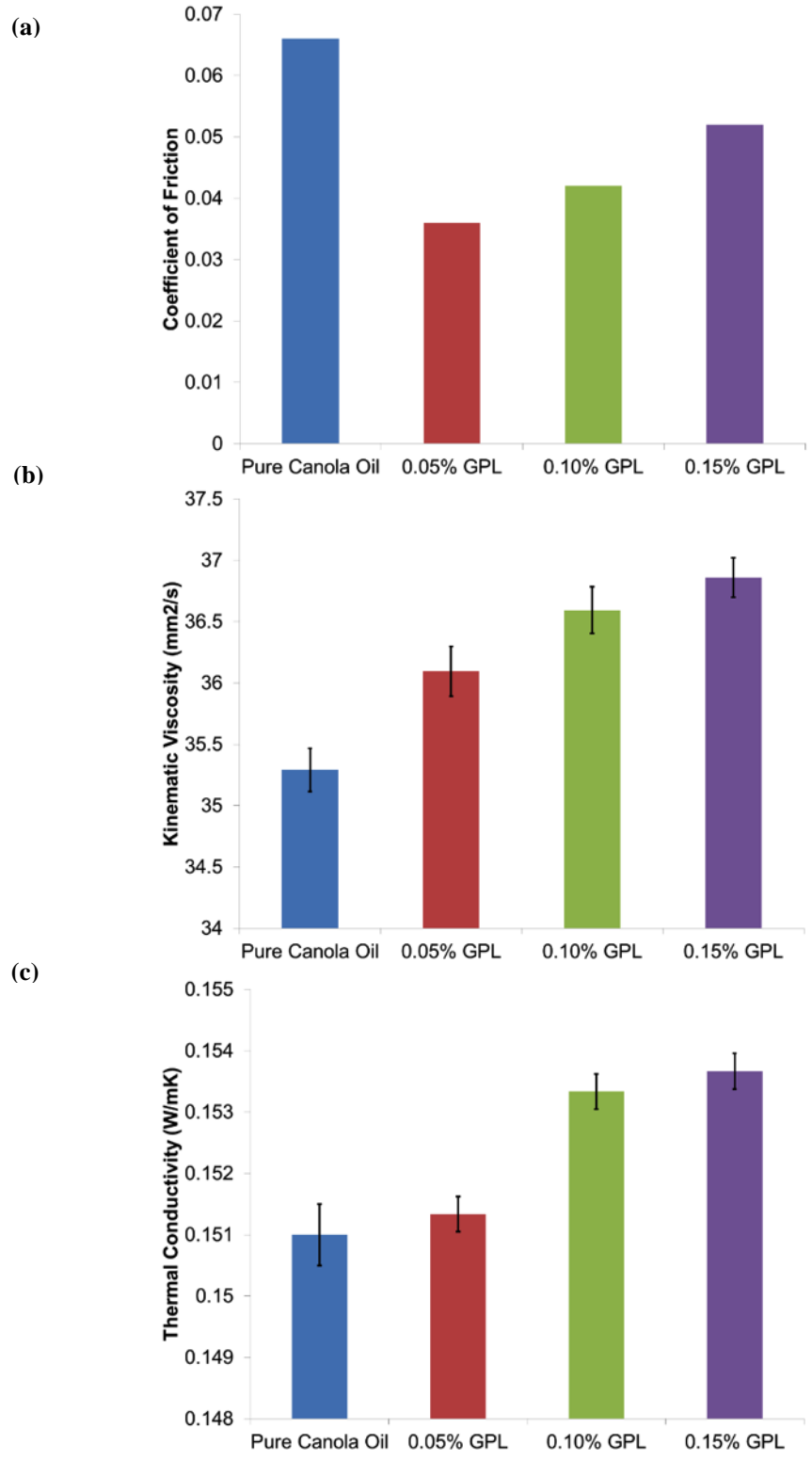


Figure 23 – Carboxyl Graphene Platelets (GPL) analyzed. (a) Scanning Electron Microscope (SEM) imaging. (b) X-Ray Photoelectron Spectroscopy indicates prominent peaks at ~286 eV for hydroxyl and ~289 eV for carboxyl functional groups attached to the basal plane of graphene.<sup>10</sup>

***Dispersion Characterization:*** In order to judge the dispersion quality and its suitability for micromachining applications, multiple characterization techniques were used. The effect of added graphene platelets on the coefficient of friction, thermal conductivity as well as kinematic viscosity was measured and quantified.

To determine the coefficient of friction, a compressive load of 50 lbf was applied through two glass-filled PTFE pins on to an aluminum plate, which is attached to a universal testing machine. This was done in accordance with testing procedures developed by Maru and Tanaka<sup>16</sup>. The pins move horizontally over the surface under this applied load for a certain number of passes. Each one of the cutting oil formulations is tested by applying a thin layer (~500  $\mu\text{L}$ ) on to the aluminum surface. Once the apparatus is assembled, the aluminum plate reciprocates back and forth using linear actuators. The load cell measures dynamic friction forces experienced by the PTFE pins under these conditions.

Figure 24a clearly shows how the addition of graphene platelets causes the coefficient of friction to be reduced dramatically as compared with baseline canola oil. Using canola oil rather than a dry surface causes the coefficient of friction to drop by ~57.14%. The friction coefficient is seen to further reduce considerably by 45.45% for 0.05% of graphene loading. Higher concentrations seem to have lower levels of improvement with reductions of 36.36% and 21.21% for 0.10% and 0.15% of graphene loading respectively. It is interesting to note that while frictional coefficients with graphene laden canola oils are lesser than what is observed for pure canola oil, an increase in graphene content does increase friction at the interface. This may be explained by excess buildup of graphene layers at the tool-workpiece interface.



**Figure 24 – Varying concentrations of carboxyl graphene dispersed in canola oil positively impact critical parameters for metal cutting fluids. (a) Coefficient of Friction. (b) Kinematic Viscosity. (c) Thermal Conductivity.<sup>8</sup>**

Figure 24b and c show the kinematic viscosity and thermal conductivity of the created formulations. Kinematic viscosity, measured with a Canon-Fenske routine viscometer; was found to increase as expected with additional solids content. The kinematic viscosity of the liquid formulation increases by 2.27%, 3.69% and 4.44% for 0.05%, 0.10% and 0.15% respectively. This slight increase did not adversely affect the application of oil in any way. Thermal conductivity was measured with a KD-2 Pro thermal conductivity probe. The conductivity of canola oil with graphene did increase though not very significantly. The increases measured were 0.66%, 1.90% and 2% for 0.05%, 0.10% and 0.15% loadings of graphene platelets. This rise is not as high as seen in the previous study with semi-synthetic metal working fluid and thermally reduced graphene. This indicates that canola oil acts as a stronger barrier to heat transmission. In addition, carboxyl and hydroxyl groups on the graphene sheet that allow it to disperse well may also be reducing its thermal conductivity.

Micro-machining tests that were performed using these canola oil based cutting fluid formulations using a Mikrottools DT-110 CNC machine tool. Cutting temperature and cutting force data was collected on this instrument. The data has not been included here for the sake of brevity but may be found in Reference 8. The cutting temperatures measured make it abundantly clear that adding graphene nano-platelets to canola oil helps with heat dissipation in a significant manner. As the concentration of graphene is increased, the maximum temperature drops even further. Although the thermal conductivity did not improve as much, it seems that the graphene platelets still have an effect on maximum temperature rise during the cut. The dry cut causes highest temperature rise in the cutting zone, as expected. Adding pure canola oil to the surface drops this maximum temperature rise by ~13%. The 0.05% mass loading led to a further decrease of ~24%, while 0.10% and 0.15% resulted in large drops of ~31% and 58% respectively.

The relatively large drops in temperature are inconsistent with the low improvements observed in thermal conductivity. An alternate mechanism of carboxyl graphene reduction to reduced graphene is believed to be the reason for this discrepancy. It is well known, that graphene oxide and other graphenes with oxygen functional groups get reduced when they are exposed to high temperatures. This is in fact a major production method for single and few layered graphene flakes. It is reasonable to assume that the

high temperatures at the tool-workpiece interface might cause the decomposition of oxygenated graphene flakes (in this case carboxyl and hydroxyl groups), which act as a sacrificial heat sink, thus reducing overall cutting temperatures. Better tool lifetimes and surface finish may thus be obtained with the use of graphene in plant-derived cutting oils.

With respect to resultant cutting forces, the data was averaged over the entire length of cut for each condition. The use of canola oil (without graphene) results in ~2.3% reduction in the average cutting force as compared to dry conditions. Adding graphene platelets results in further decreases of ~6.9%, 11.3%, and 8.9% for 0.05%, 0.10%, and 0.15% dispersions over pure canola oil. It must be noted that beyond a certain limit, graphene platelets degrade the performance and result in increased cutting forces. This can be explained by oversaturation of canola oil, and subsequent agglomeration and coalescence of graphene flakes. Larger agglomerates would build up near the tool-workpiece interface, resulting in increased cutting forces.

### **5.1.3 Summary**

Graphene platelets were oxygenated to various levels, facilitating the creation of stable dispersions in different mediums. Highly oxidized graphene made using the Modified Hummer's method disperses extremely well in aqueous suspensions. Staudenmaier method is used to synthesize graphene sheets with lesser oxygen functional groups that cause more agglomeration resulting in larger flake sizes as observed by dynamic light scattering experiments. For non-polar, canola oil based cutting fluids, carboxylated graphene sheets were found to possess the ideal level of oxygenation. Carboxyl and hydroxyl functional groups present at the edges of pristine graphene sheets help improve their affinity to non-polar, fatty acid chains. Using well-dispersed formulations, the cooling and lubrication efficiency is seen to improve resulting in reduced cutting forces and lower cutting temperatures. The added graphene platelets also result in significantly lower coefficient of friction at the interface. This is due to shearing of the few-layered platelets that insert themselves between the tool and workpiece. The cutting forces are thus reduced resulting in better overall performance and lower tool wear over time. However it must be noted that the modest increases observed in thermal conductiv-

ity do not fully account for the observed drop in maximum temperature rise in the cutting zone. In fact, the reduction of oxygenated functional groups on these graphene sheets may play a major role in heat dissipation for such systems. A tipping point is observed with respect to performance, wherein adding more graphene results in increased cutting forces. This implies that there is a saturation point for the cutting oil, beyond which additional graphene flakes are unable to disperse properly, and end up agglomerating and building up at the tool edge. This causes higher cutting forces and adversely affects the overall lubrication efficiency.

#### 5.1.4 References

1. Stanford, M., & Lister, P. M. The future role of metalworking fluids in metal cutting operations. *Ind. Lubr. Tribol.* **54**, 11-19 (2002).
2. Skerlos, S. J., Hayes, K. F., Clarens, A. F., & Zhao, F. Current advances in sustainable metalworking fluids research. *Int. J. Sust. Manuf.* **1**, 180-202 (2008).
3. Forbes, E. S. Antiwear and extreme pressure additives for lubricants. *Tribology* **3**, 145-152 (1970).
4. Mang, T., & Dresel, W. Lubricants in the environment. In *Lubricants and Lubrication*. Edn. 2 (eds. Mang, T., & Dresel, W.) 7.119-7.182 (John Wiley & Sons, Mannheim, Germany, 2007).
5. Adler, D. P., Hii, W. S., Michalek, D. J., & Sutherland, J. W. Examining the role of cutting fluids in machining and efforts to address associated environmental/health concerns. *Mach. Sci. Technol.* **10**, 23-58 (2006).
6. Shashidhara, Y. M., & Jayaram, S. R. Vegetable oils as a potential cutting fluid—an evolution. *Tribol. Int.* **43**, 1073-1081 (2010).
7. Erhan, S. Z., & Asadauskas, S. Lubricant basestocks from vegetable oils. *Ind. Crop. Prod.* **11**, 277-282 (2000).
8. Chu, B., Singh, E., Koratkar, N., & Samuel, J. Graphene-Enhanced Environmentally-Benign Cutting Fluids for High-Performance Micro-Machining Applications. *J. Nanosci. Nanotechnol.* **13**, 5500-5504 (2013).
9. Samuel, J., Rafiee, J., Dhiman, P., Yu, Z. Z., & Koratkar, N. Graphene colloidal suspensions as high performance semi-synthetic metal-working fluids. *J. Phys. Chem. C* **115**, 3410-3415 (2011).
10. Smith, P.J. *et al.* Graphene oxide colloidal suspensions mitigate carbon diffusion during diamond turning of steel. *J. Manuf. Proc.* **17**, 41-47 (2015)
11. Li, D., Müller, M. B., Gilje, S., Kaner, R. B., & Wallace, G. G. Processable aqueous dispersions of graphene nanosheets. *Nat. Nanotechnol.* **3**, 101-105 (2008).
12. Hummers Jr, W. S., & Offeman, R. E. Preparation of graphitic oxide. *J. Am. Chem. Soc.* **80**, 1339-1339 (1958).
13. Dreyer, D. R., Park, S., Bielawski, C. W., & Ruoff, R. S. The chemistry of graphene oxide. *Chem. Soc. Rev.* **39**, 228-240 (2010).
14. Balasubramanian, K., & Burghard, M. Chemically functionalized carbon nanotubes. *Small* **1**, 180-192 (2005).
15. Chen, Y., Yao, X., Zhou, X., Pan, Z., & Gu, Q. Poly (lactic acid)/graphene nanocomposites prepared via solution blending using chloroform as a mutual solvent. *J. Nanosci. Nanotechnol.* **11**, 7813-7819 (2011).
16. Maru, M. M., & Tanaka, D. K. Consideration of stribeck diagram parameters in the investigation on wear and friction behavior in lubricated sliding. *J. Braz. Soc. Mech. Sci.* **29**, 55-62 (2007).

## 5.2 Nanomaterial Electrode Synthesis for Energy Storage Devices

### 5.2.1 Introduction

Electrochemical energy storage systems are ubiquitous in today's environment. As the world's population surpasses 7 billion, energy storage is becoming critical not only for consumer electronic goods, but also for larger applications such as electric vehicles and storage for intermittent renewable energy sources that need to be integrated with the grid. These applications are much more demanding than in terms of performance as well as production volume and cost requirements.

As we seek to transition to a low-carbon economy and reduce our consumption of fossilized hydrocarbon fuel sources, it is imperative that we produce, store and use more renewable energy. The International Panel for Climate Change (IPCC) recently reiterated the urgency with which humans need to cut down greenhouse gas emissions (~40-70% by 2050 and down to zero by 2100)<sup>1</sup>. With current technology, production of renewable energy is not too expensive. In fact solar cell prices have come down exponentially in the past three decades, and wind energy production has shown tremendous success with global deployments growing rapidly<sup>2-5</sup>. However the intermittence of these sources does create problems for transmission and consumption at the customer end. This consumption includes electric vehicles as well as electricity used to power office buildings and homes. Stationary power plants are the biggest emitters of greenhouse gases and replacing them with decentralized renewable sources supported by energy storage systems is a long term solution to our societal needs. More so, replacing an existing fleet of over a billion gasoline powered automobiles with electric or hybrid electric vehicles will require significant advancements in battery technology. The energy density and power density achievable by a modern internal combustion (IC) engine is unmatched by any existing battery chemistry. Tackling this century's challenge of cutting emissions down to zero, requires the development of a groundbreaking energy storage technology, one that can offer high energy and power density at low costs and eventually replace the internal combustion engine.

### 5.2.2 Lithium Ion Batteries

Lithium-ion is currently the battery chemistry of choice for consumer electronics, electric vehicles and even grid storage solutions. The first ever lithium ion cell, developed at Exxon in 1976, featured a transition metal dichalcogenide ( $\text{TiS}_2$ ) electrode paired with a bare lithium metal anode<sup>6</sup>. However the use of pure lithium metal with non-aqueous electrolytes resulted in the formation of sharp growths called dendrites. Dendrites are caused by subsurface imperfections and impurities that lead to charge concentration and the subsequent electroplating of lithium. The tip-like extension tends to grow out from the surface and becomes longer with each charge/discharge cycle. As the dendrites accumulate additional lithium, the projections can eventually extend and pierce through the separator causing an electrical short between the two electrodes.

This led the community towards layered-structured lithium metal compounds such as transitional metal oxides, spinels and phospho-olivines that could be used as the lithium source<sup>7-8</sup>. In 1980, Goodenough and his research team pioneered the use of lithium cobalt oxide ( $\text{LiCoO}_2$ ) as a cathode material<sup>9</sup> with a theoretical capacity of  $\sim 273$  mAh/g and theoretical energy density of  $1.11 \text{ kWh kg}^{-1}$ . However, the dissolution of cobalt above 4.2 V, restricts the maximum possible voltage window and thus the practically achievable capacity to  $\sim 140$  mAh  $\text{g}^{-1}$ . Recent advancements such as the partial substitution of cobalt with nickel to suppress lattice expansion, and aluminum doping for improved conductivity have led to better performance over extended cycling<sup>10</sup>.  $\text{LiCoO}_2$  cathodes are the most widely deployed in today's commercial lithium-ion batteries.

A wide variety of anode materials are capable of reversible electrochemical reactions with lithium, including the formation of alloys or intercalates. Sony Corporation in 1991 for the first time commercialized a lithium ion battery with graphitic anodes and  $\text{LiCoO}_2$  cathodes<sup>11</sup>. This chemistry remains dominant in the commercial space, albeit with a few changes to the metal-oxide composition. Graphitic carbon allows for an intercalation reaction, wherein lithium ions insert themselves in the interlayer spacing between individual graphene sheets, resulting in the formation of  $\text{LiC}_6$ . Although, there have been significant developments in anode chemistry since then, with various studies exploring high capacity anodes such as silicon and tin among other materials, the low

cost and electrochemical stability of graphite over extended cycling make it the industrial incumbent<sup>12-13</sup>.

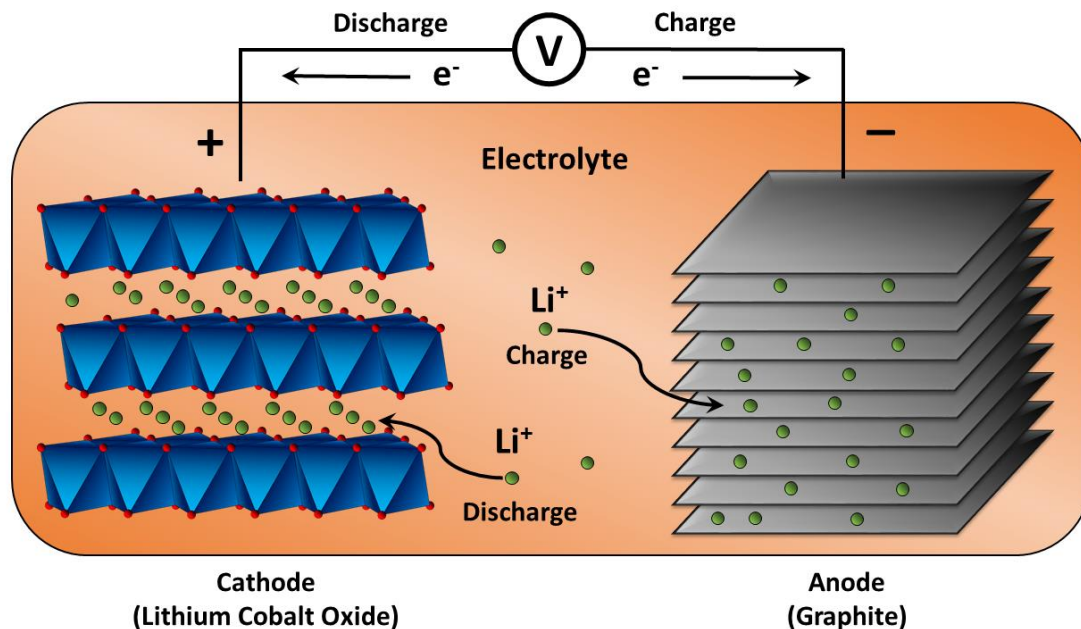


**Figure 25 – Schematic representation of a commercially available  $LiCoO_2$  - Graphite Li-Ion Cell.**

More recently, the research community has been focusing on the development of nanomaterials for electrochemical energy storage. Lithium iron phosphate nanoparticles allow for high rate capabilities, silicon nanorods allow for better cycling ability while 2-dimensional graphene sheets allow for enhanced capacities beyond what is predicted theoretically for graphite<sup>14-16</sup>. A comprehensive review of nanomaterials for lithium-ion batteries is beyond the scope of this work, but it must be noted that nanostructured electrodes are inherently not scalable. This is a major issue, considering any improvement in the cathode or anode chemistry needs to be weighed against its cost effectiveness and manufacturing scalability. The overall cost is not only a function of the material constituents, but also the ease of manufacturing and process scalability. Currently, the battery industry uses large industrial coating processes, such as doctor blading, to paste slurries comprising of electrode materials, polymeric binders and conductive additives on to metal current collector foils. These foils are then cut and

calendared before being assembled into cylindrical or prismatic cell configurations. This process is extremely high throughput and uses economies of scale to bring costs down. It is clear, that in order to create next generation energy storage devices, nanomaterial processing techniques need to be developed to the point that they allow for industrial scale production. The challenges lie not only with keeping costs low, but also with scaling up the material dimensions to micro and macro levels while maintaining nanoscale properties.

### **5.2.3 Freestanding Graphene Electrodes**

Graphene, being the 2-dimensional counterpart for graphite, with its high surface area and superb electronic conductivity has naturally been the subject of intense research for energy storage applications. A host of recent studies have explored graphene-based electrodes for capacitors, super-capacitors and batteries<sup>17-19</sup>. Most approaches follow the industry standard technique and mix exfoliated graphene sheets in organic solvent based slurries with polymeric binders and paste them on to metal current collector foils. This results in individual sheets coalescing and agglomerating, reducing the overall conductivity and surface area, essentially nullifying the various benefits nano-scale dimensionality promised. Understanding this, there has also been some work on creating pure, unadulterated graphene electrodes<sup>20-21</sup>.

In 2012, Mukherjee et al. demonstrated the use of photo-thermally reduced graphene sheets as lithium-ion battery anodes<sup>22</sup>. Freestanding graphene oxide papers were exposed to a laser or photo-thermal flash lamp that provides a brief pulse of high intensity photonic energy. The rapid heating up of insulating graphene oxide results in the formation of carbon dioxide and monoxide, generating extremely high interlayer pressures that cause mini-explosions as the gases force their way out. This explosive deoxygenation leads to freestanding reduced graphene macrostructures. The exfoliation process produces porous graphene networks with several microscale cracks, pores and intersheet voids, (Figure 27c and d) resulting in enhanced electrolyte wettability and faster lithium ion diffusion. The lack of polymeric binders ensures that graphene sheets are accessible to lithium ions in the electrolyte and have a low interfacial charge transfer resistance. To begin, graphite is oxidized to give graphite oxide (GO). GO is then

exfoliated in DI water through ultrasonication, yielding graphene oxide sheets in dispersion. The colloidal suspension of graphene oxide flakes is then filtered through an alumina membrane (Whatman Anodisc ~47 mm diameter) to produce freestanding graphene oxide papers upon drying. Following this, the GO paper is subjected to a laser or photo-thermal flash and the high energy exposure results in carbon reacting with oxygen and escaping to cause deoxygenation. The rapid outgassing of carbon oxides leads to the creation of microscopic pores and cracks that enhance electrolyte wettability and improve lithium ion diffusion within the graphene network. Individual graphene sheets remain welded together to form a robust and flexible structure that can be used as an electrode without the need for metallic current collectors, given their high electronic conductivity

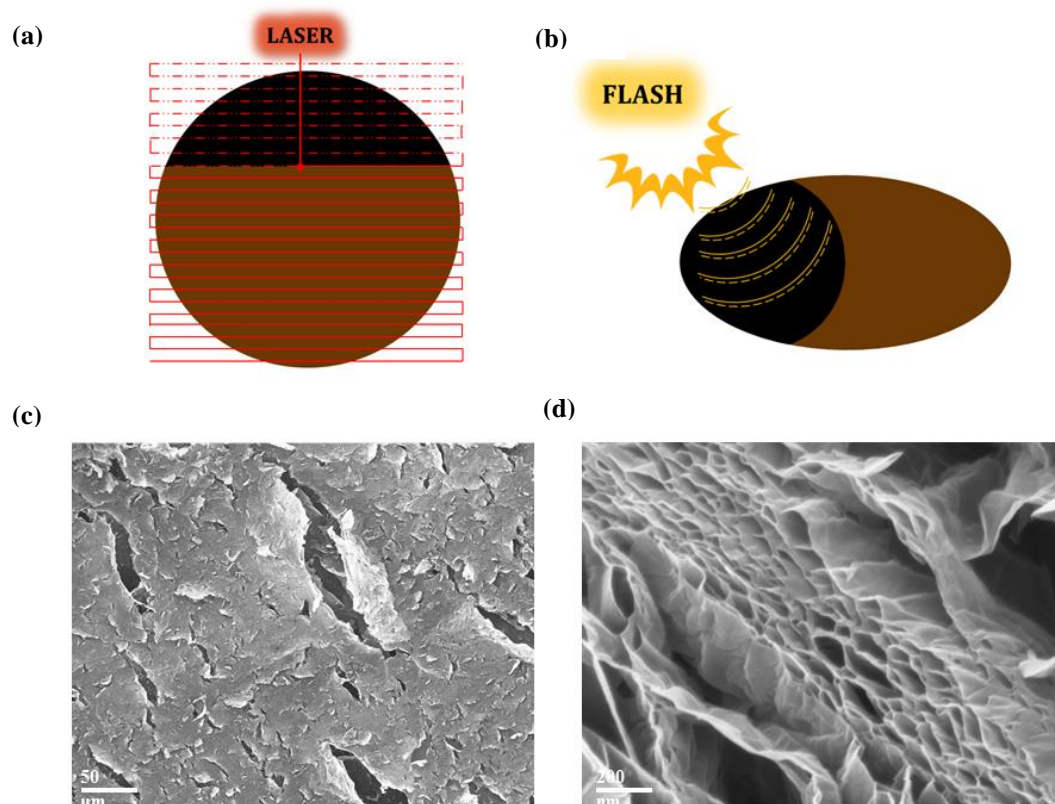


**Figure 26 – Photo-thermal reduction of graphene oxide sheets induces a rapid deoxygenation reaction resulting in the formation of freestanding graphene electrodes. (a) Laser based raster scanning. (b) Xenon flash induced deoxygenation. (c) Freestanding electrode is found to be robust and flexible. (d) Top view showing cracks and pores created as a result of photo-thermally induced deoxygenation.**

Adapted and reprinted with permission from “Mukherjee, R., Thomas, A. V., Krishnamurthy, A., & Koratkar, N. Photothermally reduced graphene as high-power anodes for lithium-ion batteries. *ACS Nano* 6, 7867-7878 (2012).” Copyright 2014 American Chemical Society.<sup>22</sup>

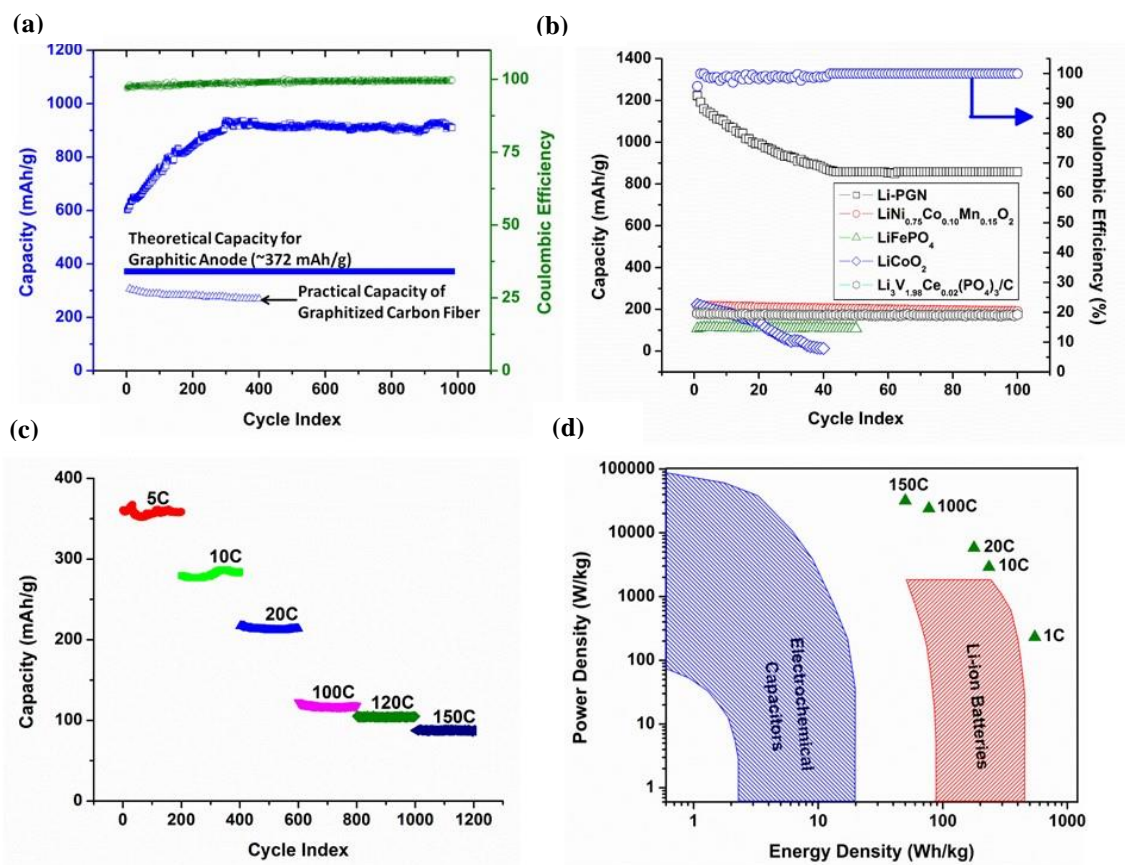


**Figure 27 – A summary of performance characteristics for graphene based electrodes (a) Graphene anodic half-cells exhibit high capacities upto  $\sim 915$  mAh/g over 1000 cycles. (b) Cathodic half cells are compared with commercially available cathodes and achieve  $\sim 815$  mAh/g. (c) Graphene electrodes demonstrate extremely high rate capability with appreciable capacities observed at rates up to 150 C. (d) A Ragone Chart comparing this battery technology with state-of-the-art energy storage devices including batteries and electrochemical capacitors.<sup>22,23</sup>**

These porous graphene networks (PGN's) were evaluated as anodes for lithium ion batteries, and exhibited capacities of  $\sim 915$  mAh/g as compared to a theoretical maximum of  $\sim 372$  mAh/g for graphite<sup>22</sup>. Practically achievable capacities of graphite are even lower. Further work on this concept revealed the reason for these high achievable capacities. Cracks and defects created during the high intensity deoxygenation were shown to be responsible for benign lithium electroplating within the nanoscopic cavities (Figure 26)<sup>23</sup>. Using pure lithium metal in batteries has proven hazardous with the growth of dendrites and resulting fire hazards. However, the small scoops of lithium metal stored within these nanoscale pores are never a large enough volume that would result in dendritic growth<sup>24</sup>. Thus restricting the amount of lithium to nano-sized chunks encapsulated by a porous graphene network enables a safe, electroplating phenomena for

high achievable capacities. This concept was used to create lithiated graphene composite electrodes, which were tested as counter electrodes that act as the lithium source in cells. When tested in cathodic half-cell configurations (Figure 27a), these electrodes demonstrated capacities of  $\sim 850$  mAh/g,  $\sim 4$  times the value attained by commercial cathodes. Moreover, the penetration of electrolyte within the macrostructure allows for extremely high rate capability. Appreciable capacities are achieved even at rates as high as 150 C (Figure 27c), where a rate of nC implies charge or discharge in  $1/n^{\text{th}}$  of an hour. The power densities thus achieved are an order of magnitude higher than commercial lithium ion technology and would enable various new applications that are not even possible with current systems. A Ragone Chart has been included for a broad perspective on where the graphene based electrodes lie in terms of energy density and power density as compared to commercial electrochemical batteries and capacitors. They can be seen pushing the envelope on both ends towards performance metrics that could compete with an internal combustion engine. An extensive overview of the battery performance is beyond the scope of this work, and may be found in References 22 and 23.

Such high energy densities and power densities would be critical for next generation applications. Electric vehicles would benefit from faster charging infrastructure, better acceleration and regenerative braking, as well as hybrid start-stop ignition systems that can significantly reduce emissions for gasoline powered automobiles. Faster charging consumer electronics are very desirable from the perspective of mobility and a tetherless world. High power applications, beyond what is currently the norm, would also benefit from such devices. Robotics has lately seen an upheaval with modern control systems and dynamics facilitating humanoids, drones and increasingly complex space faring robots with specialized applications. A reliable, high performance battery storage system can open up several possibilities in these areas and empower novel implementations.

#### **5.2.4 Roll-to-Roll Production and Assembly of 2D Nanomaterials**

To achieve scalable production of such graphene based electrodes, a top-down synthesis and assembly of graphene macrostructures is a superior approach. Bottom up techniques such as Chemical Vapor Deposition (CVD) can prove to be cost prohibi-

tive<sup>25-26</sup>. The system comprises of a tube furnace with hydrogen, methane and argon gas flow tubes attached. Throughput is limited by batch production cycles with high temperature and low pressure requirements. The process is also constrained with respect to achievable mass loadings of the deposited nanomaterial. There is some evidence that roll-to-roll CVD may be realizable, however the core limitation of CVD processes stems from the atom-by-atom assembly method, which requires a large amount of energy to produce small quantities of highly ordered material<sup>27</sup>. Such methods are suitable for electronic applications where high crystallinity and single layer architectures are desirable. For high mass loadings, solution based approaches are significantly cheaper and can prove to be technologically feasible, even at an industrial scale production levels.

Freestanding graphene and graphene oxide papers have been synthesized through the vacuum filtration of stable dispersions<sup>28-30</sup>. Notwithstanding the thorough investigation that such freestanding papers have been subjected to for various applications, ranging from battery and capacitor electrodes as well as membranes for selective gas permeation or water filtration, the techniques used to produce them are inherently not scalable<sup>31-32</sup>. The basic methodology for creating these membranes stays the same and is usually a batch process. Spin coating or evaporation may yield thin films required for membrane applications. To achieve slightly thicker films for electrode applications, vacuum filtration of exfoliated graphene oxide in water has been performed extensively.

A Modified Hummer's method was used to oxidize the graphite<sup>33</sup>. Flake graphite is first treated with heavily oxidizing reactants that intercalate between the individual sheets and introduce oxygen functional groups. These are appended to the edges of graphitic monolayers as well as on the basal plane and include hydroxyl (-OH), carboxyl (-COOH), 1,3 ethers and several other oxygen moieties that increase the interlayer spacing from ~0.34 nm to ~1.1 nm as shown by X-Ray Diffraction analysis in Figure 28. The value of  $2\theta$  goes from  $27^\circ$  to  $11^\circ$  indicating the increase in  $d$ -spacing. The enhanced wettability and larger interlayer spacing facilitates water molecule penetration. Mechanical exfoliation techniques such as ultra-sonication in aqueous environments facilitate the delamination and separation of graphite oxide flakes into single layer graphene oxide sheets. The dispersion is then filtered to assemble graphene oxide layers together, binding them strongly together to create flexible, freestanding paper like structures 4-5

cm in diameter. Vacuum filtration of graphene oxide or reduced graphene oxide in an aqueous suspension through a porous Anodisc membrane allows the sheets to settle down and bond to each other, forming a thin sheet. These membranes are formed by electroplating aluminum oxide as micro-porous, vertically oriented channels. This allows the water to escape when subjected to a vacuum.

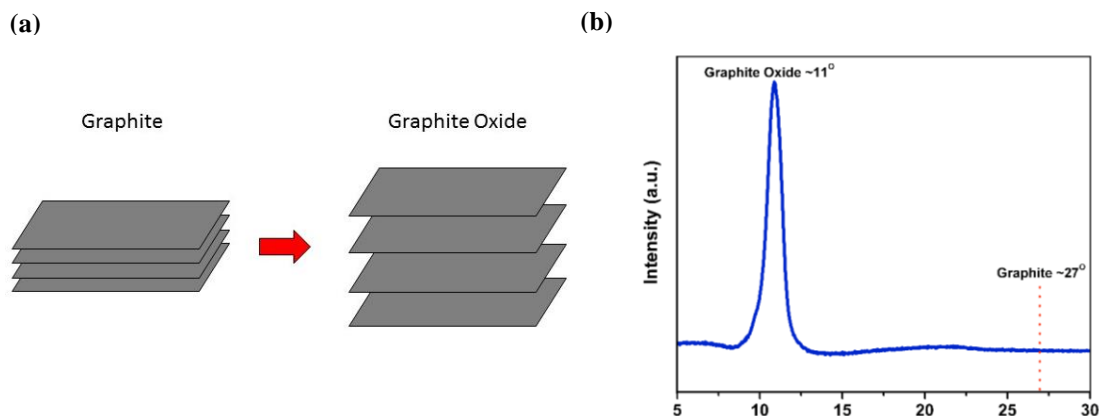


**Figure 28 – (a) Schematic representing graphite oxidation to graphite oxide and its result on interlayer spacing. (b) X-Ray diffraction of Graphite Oxide produced using Modified Hummer’s method shows a prominent peak at ~11 deg (as opposed to ~27° for pristine graphite) indicating a larger interlayer spacing of ~1.1 nm (as opposed to 0.34 nm for pristine graphite).**

Unfortunately, the largest such membrane available commercially, Whatman Anodisc, is ~47 mm in diameter. The Al<sub>2</sub>O<sub>3</sub> membrane is bordered along its periphery by a plastic ring that provides strength and support while enabling the handling of its brittle circular interior. Scaling lateral dimensions or even geometry with such membranes becomes a challenge for any filtration based methods. The process is also not suitable for creating thick sheets with higher mass loading, a critical requirement for industrial electrode applications. Since vacuum filtration relies on the deposition of graphene oxide sheets on top of each other, the buildup of layers over time slows down the flow of water considerably. The water molecules must pass through the interlayer spacing of each deposited layer in order to be completely removed. This creates a tortuous path for the fluid and significantly slows down the water flow. Even ~10-20 microns thick graphene oxide papers can take ~72-96 hours for complete water removal and drying before they are ready for use. It must be noted that the time increase is extremely non-linear and rapid after a certain point. This is understandable considering the impediment to water flow increases over the duration of the process. This infeasibility of this method at any

meaningful scale necessitated the development of a faster method that could allow for the synthesis of large aspect ratio graphene macrostructures with high mass loadings in shorter time periods.

The reason graphene oxide dispersions are stable and resist aggregation is the inherent electrostatic repulsion that individual sheets have with each other. Any particle or sheet dispersed in a medium attracts charged species that interact chemically with the surface. A layer of ionic charges thus builds up and is consequently balanced by a second layer of loosely attached ions, giving rise to the “interfacial double layer”. The electric potential measured at the edge of this solvation shell relative to a point in the bulk fluid is termed the Zeta Potential. Even though this measured value is lesser than the real surface charge beneath the double layer, it is a good measure for the electrostatic repulsion experienced between similarly charged particles or sheets. A high value of zeta potential indicates a more stable suspension. The highly negative surface charge on graphene oxide is evidenced by its zeta potential value of approximately -40 mV at a neutral pH of  $\sim 7$ <sup>34</sup>. This characteristic was used to develop an electrophoretic deposition process that allows for rapid synthesis of high mass loading graphene oxide paper. A graphene oxide colloidal dispersion is subjected to an electric field that initiates the movement of negatively charged species (monolayer graphene oxide) towards the anode. The process is initiated by the electrolytic splitting of water and the deposition is conducted at 10V. The graphene oxide sheets moving towards the current collector are collected on a porous membrane composed of cellulose ester or polypropylene. After drying, the deposited sheet may be separated by dissolving the cellulose ester in acetone. The sheet may just be peeled off of polypropylene. Figure 29a shows a bench-top prototype developed for roll-to-roll production of large scale graphene oxide sheets. This setup was used to demonstrate the synthesis of large sheets as a proof-of-concept. Figure 29b shows the variation of current and resistance with time as the deposition thickness increases. Initially the current measured is  $\sim 13$  mA but it quickly drops off to 2-3 mA as the layers build up, increasing overall interfacial resistance.

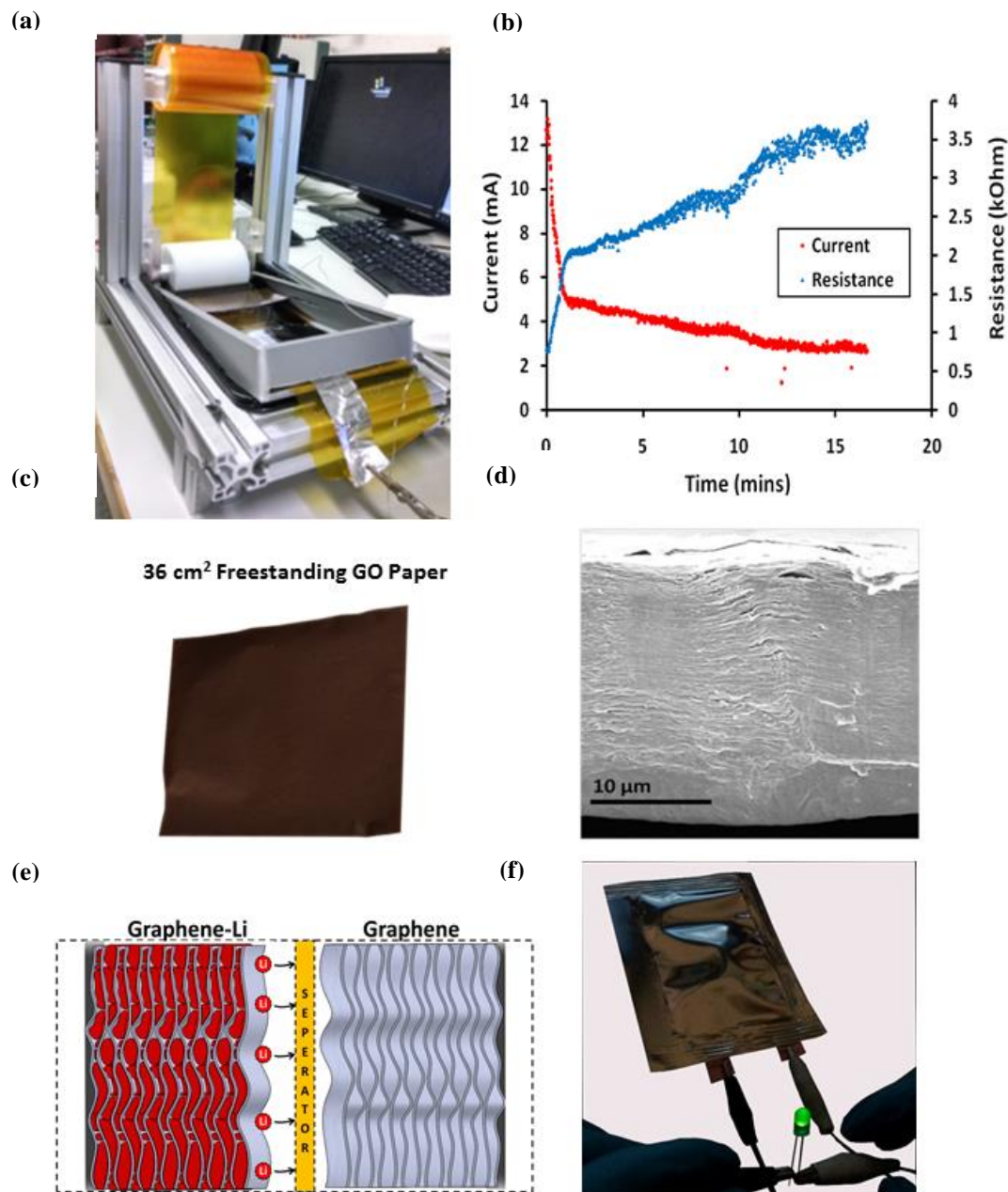


**Figure 29 – (a) Profiles for change in current and resistance as a function of time during the electro deposition of graphene oxide. (b) Roll-to-Roll electrodeposition setup built for graphene oxide electrodeposition. (c) Image of a large area freestanding graphene oxide sheet. (d) Cross-sectional SEM image of synthesized graphene oxide paper. (e) Schematic representation of All-Carbon lithium ion cell using graphene anodes and graphene-lithium composite cathodes. (f) Image of 20 mAh pouch cell built using graphene based electrodes powering an LED. Electroplating offers a drastic reduction in production time, leading to faster processing for industrial scale electrodes, with high achievable mass loadings. Flexibility with lateral dimensions enables device scale prototypes.<sup>23</sup>**

The deposition process takes ~17 minutes for a ~20  $\mu\text{m}$  thick graphene oxide layered structure, and a total of ~6 hours including drying in ambient conditions. When compared to ~96 hours for a similar mass loading with vacuum filtration, this process offers an order of magnitude advantage with reduced process times and effectively lower cost of production.

It must also be noted that electrodeposition process was used to create sheets with thicknesses ranging from ~10-100  $\mu\text{m}$ , thereby establishing the versatility of this process for various applications. Mass loadings of ~5  $\text{mg}/\text{cm}^2$  for reduced graphene electrodes were easily achieved as per industrial standards. In comparison vacuum filtration only allows up to ~1  $\text{mg}/\text{cm}^2$ , suitable for research but not sufficient for device level applications. Figure 29c and d show a photographic image and SEM image of graphene oxide papers prepared using this method. The graphene oxide paper is 36  $\text{cm}^2$  in area, limited only by the dimensions of the bath used for electrodeposition. Figure 29 e and f depict a schematic and photographic image respectively, for the All-Carbon lithium-ion battery enabled by such graphene based electrodes. The specific capacity, high rate capability, electro-chemical stability and extended cycle life for graphene electrodes produced by the photo-thermal reduction of freestanding graphene oxide have been discussed extensively, along with predicted mechanisms for such performance attributes in References 22 and 23.

### 5.2.5 Summary

A novel electrodeposition based approach is investigated and developed for scaling up the assembly of nanosheets into macrostructures. This process itself is highly scalable with respect to lateral dimensions that may be achieved. It also enables the synthesis of electrodes with high mass loadings of ~5  $\text{mg}/\text{cm}^2$  and higher as required, thus fulfilling industrial requirements for lithium ion batteries. The process was demonstrated in a proof-of-concept roll-to-roll production line that facilitates a continuous, high throughput manufacturing technology. The resulting graphene oxide precursor is subjected to photo-thermal energy for an intense deoxygenation reaction, resulting in myriad pores and cracks within the layered structure. The presence of defects initiates benign lithium electroplating within the porous graphene network, resulting in high

achievable capacities and thus breakthrough energy density ( $\sim 650$  Wh/kg). The enhanced wettability due to this graphene networks porous nature also reduces interfacial resistance at the electrolyte-electrode interface, providing better lithium ion transfer kinetics and thus high power densities ( $\sim 30$  kW/kg).

## 5.2.6 References

1. Field, C. B., Barros, V. R., Mach, K., & Mastrandrea, M. Climate change 2014: impacts, adaptation, and vulnerability. *Working Group II Contribution to the IPCC 5th Assessment Report-Technical Summary*, 1-76 (2014).
2. Green, M. A. Photovoltaics: technology overview. *Energ. Policy* **28**, 989-998 (2000).
3. Zahedi, A. Solar photovoltaic (PV) energy; latest developments in the building integrated and hybrid PV systems. *Renew. Energ.* **31**, 711-718 (2006).
4. Blanco, M. I. The economics of wind energy. *Renew. Sust. Energ. Rev.* **13**, 1372-1382 (2009).
5. Hoogwijk, M., de Vries, B., & Turkenburg, W. Assessment of the global and regional geographical, technical and economic potential of onshore wind energy. *Energ. Econ.* **26**, 889-919 (2004).
6. Brandt, K. Historical development of secondary lithium batteries. *Solid State Ionics* **69**, 173-183 (1994).
7. Tarascon, J. M., & Armand, M. Issues and challenges facing rechargeable lithium batteries. *Nature* **414**, 359-367 (2001).
8. Armand, M., & Tarascon, J. M. Building better batteries. *Nature* **451**, 652-657 (2008).
9. Mizushima, K., Jones, P. C., Wiseman, P. J., & Goodenough, J. B.  $\text{Li}_x\text{CoO}_{2(0 < x \leq 1)}$ : A new cathode material for batteries of high energy density. *Solid State Ionics* **3**, 171-174 (1981).
10. Chen, C. H. *et al.* Aluminum-doped lithium nickel cobalt oxide electrodes for high-power lithium-ion batteries. *J. Power Sources* **128**, 278-285 (2004).
11. Nishi, Y. Lithium ion secondary batteries; past 10 years and the future. *J. Power Sources* **100**, 101-106 (2001).
12. Obrovac, M. N., & Christensen, L. Structural changes in silicon anodes during lithium insertion/extraction. *Electrochem. Solid St.* **7(5)**, A93-A96 (2004).
13. Idota, Y., Kubota, T., Matsufuji, A., Maekawa, Y., & Miyasaka, T. Tin-based amorphous oxide: a high-capacity lithium-ion-storage material. *Science* **276**, 1395-1397 (1997).
14. Jugović, D., & Uskoković, D. A review of recent developments in the synthesis procedures of lithium iron phosphate powders. *J. Power Sources* **190**, 538-544 (2009).
15. Chan, C. K. *et al.* High-performance lithium battery anodes using silicon nanowires. *Nat. Nanotechnol.* **3**, 31-35 (2007).
16. Yoo, E. *et al.* Large reversible Li storage of graphene nanosheet families for use in rechargeable lithium ion batteries. *Nano Lett.* **8**, 2277-2282 (2008).
17. Wang, G., Shen, X., Yao, J., & Park, J. Graphene nanosheets for enhanced lithium storage in lithium ion batteries. *Carbon* **47**, 2049-2053 (2009).
18. Wang, H. *et al.*  $\text{Mn}_3\text{O}_4$ -graphene hybrid as a high-capacity anode material for lithium ion batteries. *J. Am. Chem. Soc.* **132**, 13978-13980 (2010).
19. Liu, C., Yu, Z., Neff, D., Zhamu, A., & Jang, B. Z. Graphene-based supercapacitor with an ultrahigh energy density. *Nano Lett.* **10**, 4863-4868 (2010).

20. El-Kady, M. F., Strong, V., Dubin, S., & Kaner, R. B. Laser scribing of high-performance and flexible graphene-based electrochemical capacitors. *Science*, **335**, 1326-1330 (2012).
21. He, Y. *et al.* Freestanding three-dimensional graphene/MnO<sub>2</sub> composite networks as ultralight and flexible supercapacitor electrodes. *ACS Nano* **7**, 174-182 (2012).
22. Mukherjee, R., Thomas, A. V., Krishnamurthy, A., & Koratkar, N. Photothermally reduced graphene as high-power anodes for lithium-ion batteries. *ACS Nano* **6**, 7867-7878 (2012).
23. Mukherjee, R. *et al.* Defect-induced plating of lithium metal within porous graphene networks. *Nat. Comm.* **5** (2014). doi: 10.1038/ncomms4710
24. Harry, K. J., Hallinan, D. T., Parkinson, D. Y., MacDowell, A. A., & Balsara, N. P. Detection of subsurface structures underneath dendrites formed on cycled lithium metal electrodes. *Nat. Mater.* **13**, 69-73 (2014).
25. Li, X. *et al.* Large-area synthesis of high-quality and uniform graphene films on copper foils. *Science* **324**, 1312-1314 (2009).
26. Kim, K. S. *et al.* Large-scale pattern growth of graphene films for stretchable transparent electrodes. *Nature* **457**, 706-710 (2009).
27. Bae, S. *et al.* Roll-to-roll production of 30-inch graphene films for transparent electrodes. *Nat. Nanotechnol.* **5**, 574-578 (2010).
28. Dikin, D. A. *et al.* Preparation and characterization of graphene oxide paper. *Nature* **448**, 457-460 (2007).
29. Wang, J. Z., Zhong, C., Chou, S. L., & Liu, H. K. Flexible free-standing graphene-silicon composite film for lithium-ion batteries. *Electrochem. Commun.* **12**, 1467-1470 (2010).
30. Liu, F., Song, S., Xue, D., & Zhang, H. Folded structured graphene paper for high performance electrode materials. *Adv. Mater.* **24**, 1089-1094 (2012).
31. Koenig, S. P., Wang, L., Pellegrino, J., & Bunch, J. S. Selective molecular sieving through porous graphene. *Nat. Nanotechnol.* **7**, 728-732 (2012).
32. Li, H. *et al.* Ultrathin, molecular-sieving graphene oxide membranes for selective hydrogen separation. *Science* **342**, 95-98 (2013).
33. Dreyer, D. R., Park, S., Bielawski, C. W., & Ruoff, R. S. The chemistry of graphene oxide. *Chem. Soc. Rev.* **39**, 228-240 (2010).
34. Li, D., Müller, M. B., Gilje, S., Kaner, R. B., & Wallace, G. G. Processable aqueous dispersions of graphene nanosheets. *Nat. Nanotechnol.* **3**, 101-105 (2008).

## 6. Conclusion

This dissertation focuses on the inherent wetting characteristics of 2-dimensional nanomaterials such as graphene and transition metal dichalcogenides including tungsten disulfide and molybdenum disulfide. The molecular interaction of these nanoscale materials with water is useful to understand from a fundamental perspective for the scientific community. It is also crucial background information for engineers and scientists attempting to utilize these nanomaterials for their unique properties in various applications. The work is broadly segmented in 4 major chapters other than the introduction and conclusion.

Chapter 2 first discusses the wetting behavior of graphene when supported on flat planar substrates. Wetting transparency is observed in some cases, especially when there are long range chemical interactions between the substrate and water droplet. This allows the water molecules to “see-through” the sheer graphene monolayer, which is only  $\sim 0.34$  nm thick. This unique attribute spurred the investigation of thin graphene coatings on roughened substrates. A non-conformal graphene coating on copper nanorods showed that when the carbon layer rested on tops of these roughness features, it ended up blocking the pores and air-pockets. Such graphene coatings would demonstrate wetting opacity for highly hydrophobic surfaces, with the highest water contact angle limited by the carbon-water interaction. The surface friction was reduced significantly, and lower contact line pinning and hysteresis observed for moving water droplets on such coated surfaces. Thereafter, the conformal coating of graphene on hierarchically rough copper structures, synthesized using in-situ deposition methods such as chemical vapor deposition, is also discussed. It is observed that such adherent coatings allow graphene to demonstrate wetting transparency at a local level, thereby maintaining an overall hydrophobic state with entrapped air still exposed to the resting water droplets.

Chapter 3 departs from the supported graphene regime and explores a 3-dimensional macrostructure created using chemical vapor deposition on nickel foams. The nickel is subsequently etched away and the freestanding graphene foam obtained contains several pores and microscopic air pockets. Such foams were found to be superhydrophobic when treated with low surface energy polymers such as Teflon. The

inherent strength and elasticity of graphene based foams allows impacting water droplets to rebound off the surface, demonstrating a useful capability for various applications.

Chapter 4 expands on this work with a look at another class of 2D layered materials called transition metal dichalcogenides. Tungsten disulfide and molybdenum disulfide monolayers are studied and found to exhibit some level of wetting transparency, indicating a more complex behavior than previously predicted by simple continuum models. Furthermore, the effect of aging is studied for such monolayer samples. Earlier studies on graphene regarding hydrocarbon contamination were used as a baseline to develop a better understanding of how these monolayers would behave without any surface contamination as opposed to what is usually observed in practice. Such information may assist in the development of better models for TMD surface wettability.

Chapter 5 uses these wetting concepts to develop two distinct and diverse technologies. The wettability of nanosheets plays a critical role in the production of stable dispersions that allow manipulation and assembly of these nanosheets according to requirements for specific technological implementations. The first subchapter discusses graphene-based additives that can be used with semi-synthetic and vegetable oils in order to develop a better alternatives for metal cutting oils. This is useful for micro-machining applications where high cutting forces and temperatures may be mitigated by few-layered, sacrificial graphene sheets with chemical functionalization to help them disperse better in canola oil. This results in reduced friction and better heat dissipation heat when the graphene sheets shear and undergo thermal decomposition at the tool-workpiece interface. Finally, the development of graphene based electrodes for lithium-ion batteries are discussed. Freestanding graphene electrodes are currently produced via techniques such as vacuum filtration, which prove to be inherently not scalable for industrial use. A top-down approach to the synthesis of exfoliated graphene oxide and subsequent assembly of the nanosheets into layered structures is demonstrated. A unique roll-to-roll electrodeposition technique is invented for high-throughput production. This technique allows for rapid synthesis of thick graphene oxide sheets that are reduced photo-thermally to create high performance lithium ion electrodes. Such freestanding battery electrodes eliminate heavy metals such as cobalt and nickel, leading to improved energy and power densities while simultaneously lowering the overall cost.